

Frederik Mayer

On Multi-Material 3D Laser Microprinting

2020
Dissertation

ON MULTI-MATERIAL 3D LASER MICROPRINTING

Zur Erlangung des akademischen Grades eines
DOKTORS DER NATURWISSENSCHAFTEN
von der KIT-Fakultät für Physik des
Karlsruher Instituts für Technologie (KIT)

genehmigte

DISSERTATION

von

M.Sc. Marc Frederik Mayer
geboren in Stuttgart

Tag der mündlichen Prüfung: 06.11.2020

Referent: Prof. Dr. Martin Wegener

Korreferent: Prof. Dr. Rasmus R. Schröder

CONTENTS

CONTENTS	v
PUBLICATIONS	1
1 INTRODUCTION	3
2 FUNDAMENTALS	7
2.1 3D Laser Microprinting	7
2.1.1 Introduction	7
2.1.2 Principle	8
2.1.3 Threshold Model	10
2.1.4 Resolution Limits	12
2.1.5 Experimental Setup	15
2.2 Photoresist Chemistry	16
2.3 Microfluidics	19
2.3.1 Definition of Viscosity	19
2.3.2 Turbulent vs. Laminar Flow	20
2.3.3 The Hagen-Poiseuille Equation	21
I MULTI-PHOTORESIST 3D LASER MICROPRINTING	25
3 FLUORESCENT 3D SECURITY FEATURES	27
3.1 Introduction	28
3.2 3D Security Feature Design	30
3.3 Sample Fabrication	32
3.3.1 Fluorescent Photoresist Containing Quantum Dots . .	32
3.3.2 Printing Routine	35

CONTENTS

3.4	Fluorescence Microscopy on Fabricated Structures	38
3.4.1	One Emission Color.	39
3.4.2	Two Emission Colors	41
3.4.3	Fluorescence Stability.	43
3.5	Conclusion	47
4	INTEGRATED MULTI-MATERIAL 3D LASER MICROPRINTING	49
4.1	Introduction	50
4.2	Experimental Realization	52
4.2.1	Overview of the Microfluidic Injection System	52
4.2.2	Basic Design Guidelines	54
4.2.3	The Microfluidic Sample Holder	56
4.2.4	The Selection Valve	60
4.2.5	Flow Considerations	62
4.3	Fluorescent Security Features as Benchmark Structures	66
4.3.1	Microstructure Layout	67
4.3.2	Fabrication Routine	68
4.3.3	Fluorescence Microscopy on Fabricated Structures. . .	72
4.4	Conclusion	75
II	COMBINING 3D PRINTING AND SELF-ASSEMBLY	77
5	3D LASER MICROPRINTING OF NANOPOROUS POLYMERS	79
5.1	Porous Materials	81
5.2	Photoresist Development	81
5.2.1	Introduction	82
5.2.2	Polymerization-Induced Phase Separation (PIPS) . . .	83
5.2.3	A Photoresist Based on PIPS.	85
5.2.4	Oxygen Depletion During Printing	88
5.3	Methods for Detailed Material Characterization.	94
5.3.1	Scanning Electron Microscopy.	94
5.3.2	Optical Characterization via Ballistic Transmission. . .	100

5.4	Material Characterization	103
5.4.1	Characterization of Single-Exposed Structures	104
5.4.2	Characterization of Double-Exposed Structures.	106
5.4.3	Optical Characterization	109
5.5	A Miniaturized Ulbricht Sphere	111
5.6	Conclusion	114
6	CONCLUSIONS AND OUTLOOK	117
A	APPENDIX	123
A.1	Photoresist Formulations	123
A.1.1	Photoresists for 3D Fluorescent Security Features (chap- ters 3 and 4)	123
A.1.2	Phase-Separating Photoresist (chapter 5)	124
A.2	Further Experimental Details.	125
A.2.1	Security Feature Samples	125
A.2.2	Laser Scanning Fluorescence Microscopy	126
A.2.3	3D Printing of Porous Samples	127
A.2.4	Supercritical Drying	129
A.2.5	Adhesion Improvement by Silanization	129
A.3	Resolution Loss under Oxygen-Depleted Conditions.	130
BIBLIOGRAPHY		133
ACKNOWLEDGMENTS		147

PUBLICATIONS

PARTS OF THIS THESIS HAVE ALREADY BEEN PUBLISHED . . .

. . . in scientific journals:

- F. Mayer, S. Richter, T. Jabbour, and M. Wegener, “3D Fluorescence-Based Security Features by 3D Laser Lithography”, *Adv. Mat. Technol.* **2**, 1700212 (2017).
- F. Mayer, S. Richter, J. Westhauser, E. Blasco, C. Barner-Kowollik, and M. Wegener, “Multimaterial 3D laser microprinting using an integrated microfluidic system”, *Sci. Adv.* **5**, eaau9160 (2019).
- F. Mayer, D. Ryklin, I. Wacker, R. Curticean, M. Čalkovský, A. Niemeyer, Z. Dong, P. A. Levkin, D. Gerthsen, R. R. Schröder, and M. Wegener, “3D Two-Photon Microprinting of Nanoporous Architectures”, *Adv. Mat.* **32**, 2002044 (2020).

. . . in patent applications:

- S. Richter, T. Jabbour, P. Hübner, M.F. Mayer, M. Wegener, “Security device and associated production method and reading device”, WO2018206534A1 / DE102017110130A1 (2018).
- P. Levkin, M. Wegener, D. Zheqin, F. Mayer, “Printing of inherently porous three-dimensional polymer objects”, DE20000011.5 (filed on 13.01.2020).

. . . at scientific conferences (only own presentations):

- F. Mayer, S. Richter, J. Westhauser, E. Blasco, C. Barner-Kowollik, and M. Wegener, “Microfluidic System for Multi-Material 3D Laser Micro-Printing” (contributed talk), SPIE Photonics West, San Francisco, USA, February 2019.
- F. Mayer, D. Ryklin, M. Čalkovský, Z. Dong, I. Wacker, P. Levkin, D. Gerthsen, R.R. Schröder, and M. Wegener, “Multiphoton 3D Laser Printing of Nanoporous Architectures” (contributed talk), SPIE Photonics West, San Francisco, USA, February 2020.

ADDITIONAL RELATED WORK HAS ALREADY BEEN PUBLISHED . . .

. . . in scientific journals:

- J. B. Mueller, J. Fischer, F. Mayer, M. Kadic, and M. Wegener, "Polymerization Kinetics in Three-Dimensional Direct Laser Writing", *Adv. Mat.* **26**, 6566 (2014).
- F. Mayer, R. Schittny, A. Egel, A. Niemeyer, J. Preinfalk, U. Lemmer, and M. Wegener, "Cloaking Contacts on Large-Area Organic Light-Emitting Diodes", *Adv. Opt. Mat.* **5**, 740 (2016).
- R. Schittny, A. Niemeyer, F. Mayer, A. Naber, M. Kadic, and M. Wegener, "Invisibility cloaking in light-scattering media", *Laser Photonics Rev.* **10**, 382 (2016).
- A. Niemeyer, F. Mayer, A. Naber, M. Koirala, A. Yamilov, and M. Wegener, "Uncloaking diffusive-light invisibility cloaks by speckle analysis", *Opt. Lett.* **42**, 1998 (2017).
- J. Qu, A. Gerber, F. Mayer, M. Kadic, and M. Wegener, "Experiments on Metamaterials with Negative Effective Static Compressibility", *Phys. Rev. X* **7**, 041060 (2017).
- S. Mannherz, A. Niemeyer, F. Mayer, C. Kern, and M. Wegener, "On the limits of laminates in diffusive optics", *Opt. Express* **26**, 34274 (2018).
- V. Hahn, F. Mayer, M. Thiel, M. Wegener, "3-D Laser Nanoprinting", *OPN* **30**, 28 (2019).
- L. Yang, A. Münchinger, M. Kadic, V. Hahn, F. Mayer, E. Blasco, C. Barner-Kowollik, and M. Wegener, "On the Schwarzschild Effect in 3D Two-Photon Laser Lithography", *Adv. Opt. Mat.* **7**, 1901040 (2019).
- Z. Dong, H. Cui, F. Wang, Z. Xiang, F. Mayer, B. Nestler, M. Wegener, and P. Levkin, "3D printing of inherently nanoporous polymers via polymerization-induced phase separation", *submitted*.
- M. Čalkovský, E. Müller, M. Meffert, N. Firman, F. Mayer, M. Wegener, and D. Gerthsen, "Comparison of segmentation algorithms for FIB-SEM tomography of porous polymers: Importance of image contrast for machine learning segmentation", *submitted*.

I INTRODUCTION

A multitude of different 3D printing techniques has evolved in the last decades and both technological as well as application development have gained considerable momentum. The charm in 3D printing lies in that it offers a previously unprecedented control over the three-dimensional shape of manufactured objects. Furthermore, the fabrication of individual parts is vastly facilitated, as new designs can immediately be printed from a digital 3D model. In many different areas, this method vastly speeds up often required iteration cycles and hence also the convergence towards a final part design. Hence, 3D printing is often also termed "rapid prototyping".

These characteristics of 3D printing often lead to striking applications: prominently, the aerospace industry has recently adopted selective laser sintering for the manufacturing of 3D metal parts. Herein, often, few 3D printed parts can replace complex assemblies of many conventionally machined parts. In doing so, complexity is reduced and weight can be saved. As an example, the startup Additive Rocket Corporation managed to halve the weight of a rocket engine while increasing its power by manufacturing it by 3D printing.¹ Likewise, the company Airbus was able to reduce the weight of a mechanical element that holds the pilot's sleeping cabin in an airplane by almost a factor of 2, while increasing its maximum loading capacity.² Such examples impressively demonstrate how a precise control over the *three-dimensional shape of objects* can help to improve parts, or even lever entirely new applications that could not have been realized before.

However, one would like to additionally be able to achieve precise control over the local material properties of printed objects. Ideally, one could

¹ Billiger, leichter, stärker – Raketen-Antriebe aus dem 3D-Drucker.
<https://heise.de/-4403793>, retrieved on August 4, 2020.

² Das Flugzeug aus dem 3D-Drucker.
<https://www.golem.de/1610/123924.html>, retrieved on August 4, 2020.

realize a large number of *very different material properties* within single three-dimensional structures in a short amount of time. Obviously, this would boost the ability to realize 3D structures with a high degree of functionality even further. Consequently, the 3D printing community is pushing into this direction for almost every common 3D printing technology. Specifically, this includes the development of integrated multi-material printers, as well as the development of new materials with highly different physical or chemical properties. As an illustrative example, multi-material extrusion-based 3D printers have been developed. Hereby, mechanically soft as well as stiff materials can be printed into one single structure, and pneumatic walking robots and Miura folding sheets have thereby been realized [1].

In this thesis, an optical 3D printing technique that is called 3D laser microprinting is employed. In particular, this method is capable of manufacturing three-dimensional *microstructures* with printing resolutions in the sub-micrometer regime. More precisely, it relies on a spatially selective polymerization of a liquid photoresist that is triggered by an optically nonlinear absorption process. Hereby, it enables the realization of three-dimensional microstructures that have not been manufacturable previously. In the present thesis, the challenges of development of 1) integrated multi-material printers and processes and 2) novel printable materials are treated in the context of 3D laser microprinting.

Using 3D laser microprinting, microstructures composed of multiple materials have previously been realized by performing multiple 3D printing steps sequentially, while processing the sample in between manually. Examples include cages for biological cells, in which cells attach selectively [2]. Another example is given by achromatic microlenses printed from materials with different dispersions [3, 4]. However, as these approaches have relied heavily on error-prone manual processing, they were limited to relatively few different materials within one printout. Consequently, integrated approaches that eliminate any manual intermediate processing steps would be desirable. This challenge is tackled in the first part of the present thesis.

With respect to the second challenge, considerable effort is put into the development of new materials [5, 6]. Current research is, for example, carried out on 3D printable stimuli-responsive polymers such as liquid crystal elastomers [7] and hydrogels [8–10], metals [11, 12], and even erasable polymeric photoresists [13, 14]. However, up to today, one can state that the vast majority of available photoresists for 3D laser microprinting yield similar properties, in that curing of them yields solid transparent polymers, that have a glass-like appearance. The second part of this thesis is dedicated

towards the realization of a photoresist that strongly differs from this trend: polymerization of this photoresist yields a polymer that is inherently *porous* with typical pore sizes below 100 nm. As a result, hierarchical nanoporous 3D microstructures can be printed from this photoresist, that could have hardly been realized otherwise. Hence, this approach constitutes a combination of the two contrary concepts of 3D printing and self-assembly. Herein, both of the concepts contribute to the full three-dimensional structure, but on different size scales. Moreover, printing of *non-porous material* is possible from the *same photoresist* by adjusting the 3D printing strategy accordingly. Hence, a variety of material properties is attainable. In this sense, this approach can also be regarded as multi-material printing from a single photoresist. Furthermore, it could also be combined with very different photoresists in a multi-material printer.

OUTLINE OF THIS THESIS

Chapter 2 treats the most important concepts that are crucial for a detailed understanding of this work. Specifically, I will start by discussing the fundamentals of 3D laser microprinting. I will furthermore briefly elaborate on fluid mechanics of laminar flows that occur in microfluidic systems, which will be required for the realization of a multi-material 3D laser microprinter (as presented in chapter 4).

The subsequent chapters are split in two parts: Part (I) discusses the printing of multi-material microstructures by printing multiple different photoresists sequentially.

In particular, I start by discussing a possible application of multi-material 3D laser microprinting in chapter 3, which is the printing of three-dimensional fluorescent security features. These security features are printed from three different photoresists with different fluorescence properties in several consecutive 3D printing steps with manual processing steps in between. They can be imaged in 3D and hence be read out by confocal laser scanning fluorescence microscopy.

Consecutively, in chapter 4, I present a fully integrated multi-material 3D laser microprinter, which was built by adding a custom-tailored microfluidic system on top of a commercial 3D printer. The capabilities of this system are demonstrated by 3D printing highly complex 3D security features. In these security features, the printing of five different fluorescent materials on a micrometer scale is demonstrated.

Subsequently, in part (II) which includes chapter 5, I describe the development of a photoresist that combines 3D printing and self-assembly. Specifically, this photoresist yields a nanoporous polymer upon polymerization, and 3D microstructures can be printed from this nanoporous polymer foam. In particular, I demonstrate that porous as well as non-porous material can be printed from the same single photoresist in-situ by fine-tuning the printing strategy. Hence, this constitutes an approach that is distinct from that in part (I). The photoresist is based on polymerization-induced phase separation, which is the pore-forming mechanism. The volume material properties of the printed structures are examined by ultramicrotomy combined with scanning electron microscopy. Due to the nanoporosity, the material is strongly light-scattering, and hence, it is characterized optically by measuring its light-scattering coefficient. As a possible application, a 3D printed Ulbricht integrating sphere is 3D printed and tested.

Finally, I summarize the results of the present thesis in chapter 6.

2 FUNDAMENTALS

In this chapter, I will discuss fundamental concepts that underlie this thesis. Most importantly, I will introduce 3D laser microprinting, i.e., the 3D printing method employed throughout this thesis. Furthermore, I will briefly discuss fluid mechanics in microfluidic systems, which is targeted towards the microfluidic injection system that is implemented into a 3D laser microprinting setup in chapter 4 of this work.

2.1 3D LASER MICROPRINTING

The following section, which treats the fundamentals of 3D laser microprinting, is structured as follows: I will start by giving an introduction, thereby discussing a number of application examples of this printing technique. Subsequently, I will elaborate on the underlying optical principles, as well as the chemical response from the photoresist. Lastly, I will briefly describe the experimental setup that was used throughout this work.

2.1.1 Introduction

3D laser microprinting is a technique for the additive manufacturing of 3D micro- and nanostructures that emerged roughly 20 years ago [15, 16]. Early demonstrations of the underlying principle, two-photon polymerization, date back to the early 1990s [17]. In the early years, development of this technology was predominantly pushed forward by the photonic crystal community. In this context, fabrication technologies for three-dimensional dielectric micro- and nanostructures were sought-after. Three-dimensional woodpile photonic crystals that were fabricated by 3D laser microprinting with lattice periods on the scale of 1 μm were subsequently demonstrated [18–20]. Since these

early days, the field has seen a vast technological development with respect to printing resolution, printing speed as well as the available photoresist materials. Consequently, the technique has in the meantime been widely adopted for a large variety of applications.

Today, notable application areas include, for example, 3D printing of refractive and diffractive micro-optics [3, 21–24], cages for biological cell-studies [2, 10, 25], interconnects between photonic chips [26], micro-robots [27], and 3D printed metamaterials [28].

2.1.2 Principle

The principle of 3D laser microprinting is illustrated in Figure 2.1. Here, a laser beam is focused into a liquid negative-tone photoresist. In the very focal region of the laser focus, a polymerization reaction is initiated, and hence, a small and locally confined volume element within the laser focus becomes solid. In analogy to “pixels” in two dimensions, this small volume element is commonly termed a “voxel”. By moving the laser focus through the liquid photoresist in three dimensions and thus by successively polymerizing many of such voxels, almost arbitrary three-dimensional polymer structures can be manufactured. After exposure, the sample is washed in organic solvents to remove excessive liquid photoresist, such that only the polymerized three-dimensional structure remains.

In more detail, 3D printing of almost arbitrary shapes can only be realized when making use of a two-photon (or higher order nonlinear) absorption process to trigger the polymerization reaction within the liquid photoresist. Loosely speaking, this leads to a better spatial confinement of the deposited energy dose within the photoresist. However, the reasoning behind the requirement of having two-photon absorption can only be understood in detail when taking into account the photoresist’s response. Hence, I will discuss this aspect in-depth in the following section 2.1.3.

Two-photon absorption was first predicted in 1931 by Maria Göppert-Mayer [29]. Here, the energy dose $D(\vec{r}, t)$ that is deposited in a material by optical absorption during the exposure time t_{exp} is proportional to the *square* of the light intensity $I(\vec{r}, t)$. In a more general sense, for a nonlinear

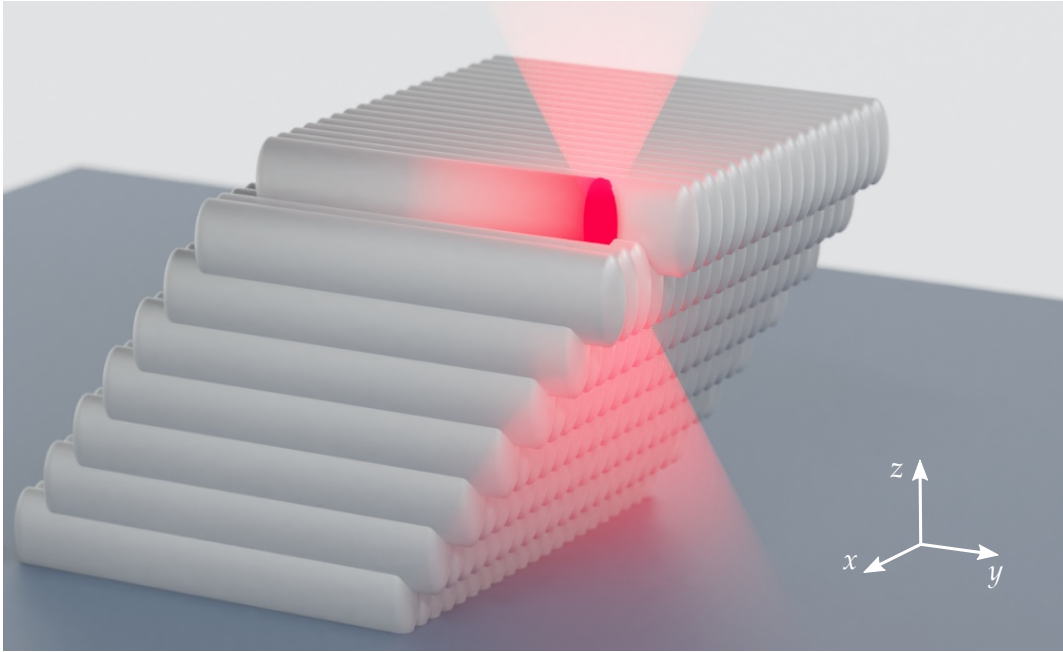


Figure 2.1: Principle of 3D laser microprinting. A liquid photoresist (not depicted) is polymerized by tightly focusing a laser beam into it. This reaction is triggered via two-photon absorption in a spatially confined reaction volume, called voxel. By scanning the laser beam through the photoresist in three dimensions, complex polymer structures can be realized. As indicated in the above scheme, structures are often fabricated in a layer-wise fashion since the laser focus can typically be rapidly scanned within xy -planes, but not in z -direction. In this case, the axial distance (in z -direction) between individual printed lines is called the slicing distance, and the lateral distance the hatching distance.

absorption process of the order N , the deposited dose can be expressed as

$$D(\vec{r}) \propto \int_0^{t_{\text{exp}}} I^N(\vec{r}, t) dt, \quad (2.1)$$

where $N = 2$ for two-photon absorption.

Furthermore, the two-photon absorption cross section that determines the magnitude of two-photon absorption in a molecule is commonly given in units of Göppert-Mayer, i.e.,

$$1 \text{ GM} = 10^{-50} \text{ cm}^4 \text{ s} / \text{photon}. \quad (2.2)$$

Since two-photon absorption cross sections of chemical molecules are typically very small, high optical intensities are required to achieve a significant absorption. Hence, with respect to 3D laser microprinting, the following strategies are pursued:

1. Typically, the laser beam is focused to a tiny spot using immersion objective lenses with high numerical apertures. Typically, the numerical aperture lies in the range from 0.8 to 1.45.
2. Furthermore, pulsed femtosecond lasers are employed. Here, high intensities occurring during the short laser pulses promote two-photon absorption. Most commonly, these lasers are emitting in the near infrared and exhibit pulse durations in the femto- to picosecond regime. Notably, the repetition rate of the laser imposes a maximum focus speed at which connected lines can be printed, because the distance between adjacent laser pulses should be smaller than the voxel size, which can be smaller than 100 nm laterally. This problem is commonly addressed by employing lasers with high repetition rates in the regime of tens of MHz, which results in connected printed lines at common focus velocities on the order of 10 cm s^{-1} .

It is worth mentioning that the photoresist has to be optically transparent at the illumination wavelength λ : due to the high intensities employed in the laser focus, even small linear absorption coefficients will result in uncontrolled excitation and heating of the photoresist. Furthermore, the photoresist should also not exhibit a significant light-scattering coefficient, as this could result in a decreased focus quality and hence reduced peak intensities in the laser focus. Specifically, one can state that the scattering mean free path l_s should be much bigger than the working distance of the objective lens used. This aspect will become of interest in the later chapters of this work (see chapter 5).

2.1.3 *Threshold Model*

The photoresist's chemical response to the energy dose deposited in the photoresist $D(\vec{r})$ is commonly described by a simple threshold model: here, one assumes that the photoresist exhibits a certain polymerization threshold dose D_{th} . Upon exposure, the photoresist becomes solid in regions for which $D(\vec{r}) > D_{\text{th}}$, while regions with $D(\vec{r}) < D_{\text{th}}$ remain liquid. This connection is illustrated in Figure 2.2(A). Furthermore, in this model, one

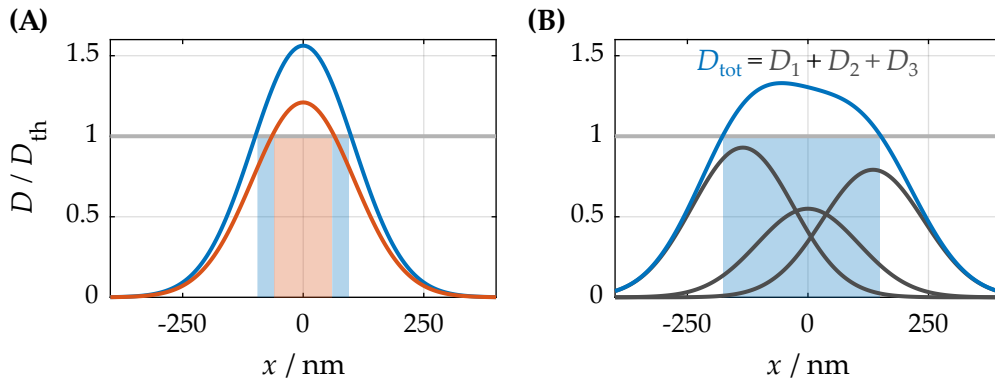


Figure 2.2: In the threshold model, exposure doses above a threshold dose D_{th} lead to solidification of the liquid photoresist. **(A)** The linewidth (shaded regions) increases when increasing the intensity of a laser focus and thereby the dose that is deposited in the photoresist. The spatial intensity profile in the laser focus is approximated by a one-dimensional Gaussian (FWHM = 350 nm). **(B)** For a photoresist that memorizes previous exposures, the dose profiles resulting from exposures that are sequential in time (gray) are added up to a total dose profile $D_{tot}(x)$. Thereby, the photoresist solidifies in a broad region (instead of no polymerization at all).

commonly assumes that the photoresist possesses an infinite memory in time: specifically, this means that the energy doses from multiple sequential exposures are added up linearly. Hence, solidification of the photoresist can also occur in regions that have seen multiple sequential exposures below the threshold value, as depicted in panel (B).

In a more chemical sense, the polymerization threshold value is associated with a certain degree of crosslinking of the polymer upon which it becomes insoluble in the photoresist, and remains as a solid structure after development. In contrast, the threshold model does not consider the rather complex microscopic reaction- and diffusion-related spatiotemporal evolution of the concentration of the different chemical species in the photoresist. Nonetheless, it most often constitutes a good approximation of the behavior observed in experiments.

While the threshold model might appear quite trivial in the first place, it is actually critical for the detailed understanding of why nonlinear absorption is required for the realization of “true” 3D architectures. A thought experiment that is frequently cited in this context is the 3D printing of a slab that is infinitely extended in the xy -plane. The optical axis is oriented along z , such

that the laser focus has to be scanned laterally throughout the entire xy -plane for constant z . In this example, if the photoresist would show a *linear* ($N = 1$) response and would only be weakly absorbing (i.e., such that the intensity does not decay along z), the integral

$$D(\vec{r}) \propto \int_0^{\infty} I(\vec{r}, t) dt \quad (2.3)$$

would yield a constant exposure dose in the entire space, independent from \vec{r} . If this constant exposure dose exceeds the polymerization threshold dose, one would not have 3D printed a slab, but rather polymerized a big block that has no confinement in z -direction. In contrast, for a nonlinear ($N > 1$) absorption process, $D(\vec{r})$ still *does* exhibit a confinement along z —and as a result, 3D printing of the same slab would be possible.

In this example, we have so far assumed that the photoresist remembers any previous exposure. It is however worth noting that the result from this thought experiment drastically changes when considering a photoresist that quickly forgets any previous exposure below the polymerization threshold value D_{th} . For such a photoresist, the requirement $N > 1$ is lifted, and a linear absorption process ($N = 1$) would suffice to experimentally realize the slab as described before. However, from an experimental viewpoint, currently available photoresists do not show this behavior.

2.1.4 Resolution Limits

In the following, I will briefly elaborate on the physical constraints that limit the resolution that can be obtained by 3D laser microprinting. Importantly, the term “resolution” in the following is defined as the minimum distance at which two separated lines can be 3D printed. Another quantity that is distinct from the resolution is the minimally attainable feature size. Within the validity of the threshold model, it can be easily understood that this quantity does *not* exhibit a fundamental lower limit: in Figure 2.2(A), one could easily choose the optical intensity such that the deposited dose exceeds D_{th} only in a small region—and hence, in theory, arbitrarily small feature sizes could be realized. In contrast, the resolution *is* fundamentally limited (at least for a photoresist with a memory), as we will see in the following.

Abbe Diffraction Limit

The fact that the attainable resolution in optical microscopy is fundamentally limited by diffraction was originally formulated by Ernst Abbe around 1873. In particular, he found that the minimum distance between two points d_{lateral} that can still be resolved laterally can be described by

$$d_{\text{lateral}} = \frac{\lambda}{2n \sin(\alpha)} = \frac{\lambda}{2\text{NA}} \quad (2.4)$$

where λ denotes the wavelength, n the refractive index of the immersion medium, α the half opening angle of the objective lens, and $\text{NA} = n \sin(\alpha)$ the objective lense's numerical aperture. This equation can be easily derived when considering the case of imaging a transmission-type grating. In the limit where at least two diffraction orders m are gathered by the objective lens, $m = \{0, \pm 1\}$, the above result is obtained [30].

In analogy, the axial resolution limit can be given as [31]

$$d_{\text{axial}} = \frac{\lambda}{n - \sqrt{n^2 - \text{NA}^2}}. \quad (2.5)$$

For example, for the experimental setup employed in chapter 4 of this work ($\lambda = 780 \text{ nm}$, $n = 1.518$, $\text{NA} = 1.2$) one can calculate a lateral limit of $D_{\text{lateral}} = 325 \text{ nm}$ and a axial limit of $D_{\text{axial}} = 1326 \text{ nm}$. Notably, d_{axial} differs from d_{lateral} by a factor of ≈ 4 . Fundamentally, one can state that $d_{\text{axial}}/d_{\text{lateral}} \geq 2$, with the lower limit obtained in the case of an idealized objective lens that has the maximum numerical aperture of $\text{NA} = n$. This fundamental limitation is commonly also observed in experiments, where the printed voxels exhibit a pronounced axial elongation.

Sparrow's Criterion

Abbe's resolution formula is a resolution criterion that is specifically tailored to the needs of *microscopy*—however, it does not consider the photoresist's detailed response upon illumination. As we have seen previously, the latter is crucial for the understanding of 3D laser microprinting. Hence, a more intuitive resolution criterion with respect to the needs of *lithography* is given by the so-called Sparrow limit [32], which can be applied to the case of 3D laser microprinting [31].

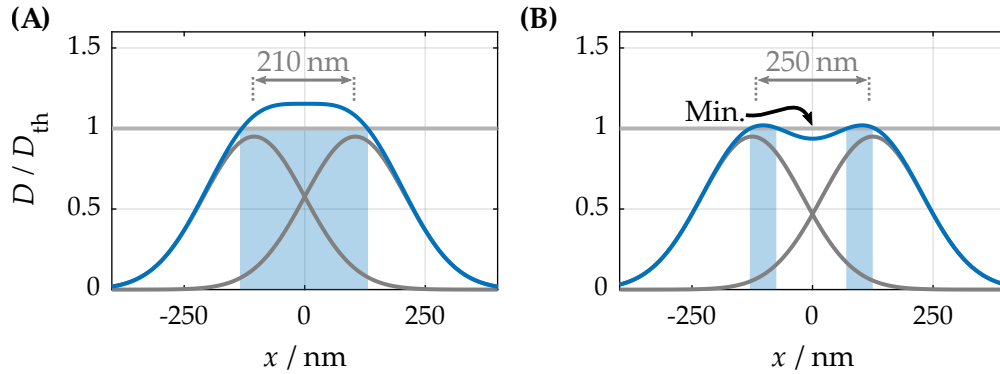


Figure 2.3: Examples illustrating Sparrow’s resolution criterion. Exposure doses from subsequent exposures (Gaussian intensity profiles with assumed FWHM = 350 nm, nonlinearity $N = 2$) are added up to the total exposure profile D_{tot} plotted in blue. The distance between the two exposures is (A) $d = 210$ nm and (B) $d = 250$ nm. Notably, in (B), D_{tot} exhibits a local minimum, such that two separated points (or lines) can be printed by tuning the laser power adequately. Subsequently, the Sparrow criterion defines the resolution as the minimal d at which D_{tot} still exhibits a local minimum.

Here, the resolution is defined as follows: two points (or parallel lines), that are spaced by a certain distance d , are exposed consecutively in the photoresist. Since we assume a photoresist with a memory, the resulting single exposure doses add up to a total exposure dose. This situation is depicted in Figure 2.3(A) and (B), respectively, for different distances d between the single exposures. Whereas the summed-up dose profile exhibits a pronounced local minimum in case (B) ($d = 250$ nm), such a local minimum is not present in case (A) ($d = 210$ nm). As a result, by tuning the deposited dose reasonably close to the polymerization threshold dose D_{th} , in case (B), two separated points (or lines) can be printed—which is unachievable in case (A). Subsequently, a purposeful definition of a resolution criterion is the minimum distance at which the summed-up deposited exposure dose still exhibits a local minimum.

Notably, this definition automatically accounts for the nonlinearity N of the photoresist. However, it is not meaningful in the case of a “forgetting” photoresist: in this case, consecutive exposure doses would *not* sum up. Particularly, the resolution then would be inherently connected to the minimum achievable linewidth, and subsequently, *not* exhibit any lower limit from a physical standpoint (see introduction of section 2.1.4).

In more detail, an approximation for Sparrow’s criterion for the case 3D

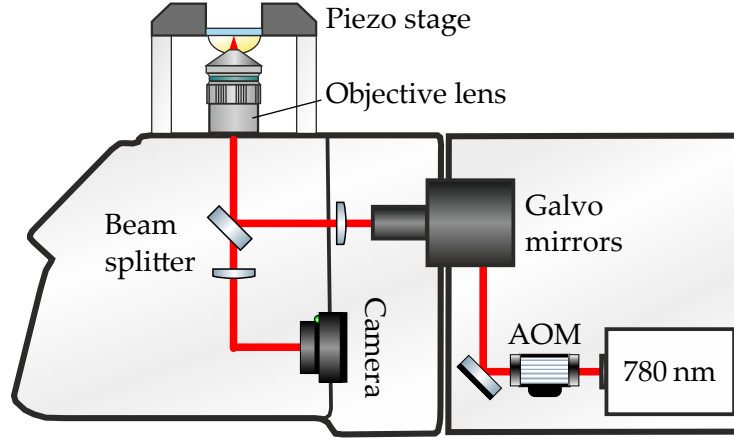


Figure 2.4: Scheme of the 3D laser microprinter used throughout this work. A femtosecond fiber laser is focused into a droplet of photoresist in the sample, triggering a polymerization. 3D printing is carried out by moving the laser focus using the galvo mirrors and the stages through the photoresist droplet, while modulating its intensity using an acousto-optical modulator (AOM). Reproduced from [33].

laser microprinting is given in [31] by introducing the nonlinearity into Abbe's formula. This modified resolution formula then reads

$$d_{\text{lateral}} = \frac{1}{\sqrt{N}} \frac{\lambda}{2NA} \quad (2.6)$$

for the lateral resolution, and likewise

$$d_{\text{axial}} = \frac{1}{\sqrt{N}} \frac{\lambda}{\left(n - \sqrt{n^2 - NA^2}\right)} \quad (2.7)$$

for the axial resolution. For the same experimental parameters as given in the previous section ($\lambda = 780 \text{ nm}$, $n = 1.518$, $NA = 1.2$ and $N = 2$), one subsequently arrives at $d_{\text{lateral}} = 230 \text{ nm}$ and $d_{\text{axial}} = 938 \text{ nm}$. Notably, for these parameters, d_{lateral} is smaller than a third of the fundamental illumination wavelength λ .

2.1.5 Experimental Setup

Throughout this work, the Photonic Professional GT 3D printer is employed. A scheme depicting this 3D laser microprinting system is shown in Figure 2.4.

It features a frequency-doubled erbium fiber laser, emitting femtosecond pulses (pulse length below 100 fs, repetition rate 80 MHz) at a wavelength of 780 nm. For fast intensity modulation of the laser beam, an acousto-optical modulator is used. The laser beam is focused using an objective lens that is most commonly directly immersed into the photoresist (“dip-in writing”). The sample holder is mounted on a piezo as well as on a motorized stage. There are two different possibilities for scanning the laser focus through the liquid photoresist:

1. **Galvo scan mode:** Here, scanning of the laser focus in the xy -plane (perpendicular to the optical axis) is carried out using galvanometric mirrors. Hereby, in the xy -plane, high focus velocities are reached (up to 15 cm s^{-1}). For shifting the sample along the optical axis or over wider lateral distances (exceeding the objective lenses’ field of view) in the xy -plane, one of the stages is used.
2. **Piezo scan mode:** Alternatively, scanning is possible along arbitrary 3D trajectories by moving the sample relative to the fixed position of the laser focus using the piezo stage (with velocities up to $\approx 200\text{ }\mu\text{m s}^{-1}$). The piezo stage has a maximum travel range of $300\text{ }\mu\text{m} \times 300\text{ }\mu\text{m} \times 300\text{ }\mu\text{m}$, and shifting of the sample outside this range is possible using the motorized stage.

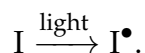
Due to the limited scanning speed in the piezo scan mode, today, the galvo scan mode is most commonly used. The printing process can be monitored using a built-in camera, that images the sample through the very same objective lens that is also used for writing. The printer is controlled from a desktop computer.

2.2 PHOTORESIST CHEMISTRY

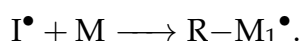
Photoresists for 3D laser microprinting commonly make use of an optically induced radical polymerization. In this reaction, the monomer units contained in the photoresist are crosslinked to form a polymer, such that the photoresist becomes solid in regions that have seen sufficient exposure to light. In the following, I will briefly introduce the reaction sequence that underlies this process:

1. **Radical generation:** First, a radical is generated from a photoinitiator

molecule I that is excited optically:



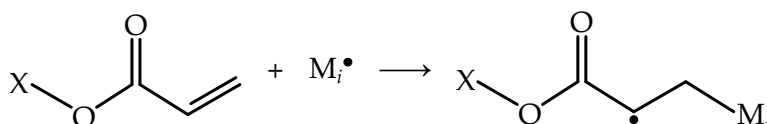
2. **Starting reaction:** Subsequently, this radical reacts with the functional group of a monomer molecule M. As a result, a new (and bigger) radical molecule is obtained (with a rest R):



3. **Chain propagation:** In the next steps, more monomer units are added likewise, and a longer polymer chain is obtained as a result. Hereby, the degree of polymerization, that is the number i of monomer units per polymer molecule, increases:



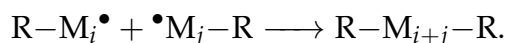
In particular, in photoresists for 3D laser microprinting, the use of monomers with acrylic or methacrylic functional groups is very common. For an acrylate group that is attached to some molecule X, in the propagation reaction, a C=C double bond is broken up, and a propagating polymer M_i^\bullet attaches as depicted below.



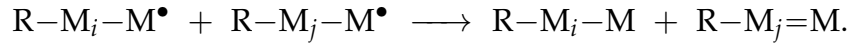
The employed monomers furthermore commonly feature *multiple* functional groups.

4. **Termination reactions:** In radical polymerizations, chain propagation can be terminated by a number of processes.

Radical-radical recombination: Here, two propagating radical chains react and form a saturated chain. Notably, the degree of polymerization strongly increases in this case:



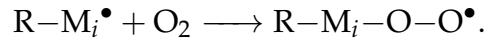
Radical disproportionation: Another possible termination reaction is given by a hydrogen atom transfer from one propagating chain to another. Hereby, two non-radical species are obtained (although one polymer chain is unsaturated and might still be reactive):



Radical quenching: Termination may also occur in combination with a quencher molecule Q, i.e.,



The molecule produced in this reaction may for example be unreactive. More specifically, in radical polymerizations with acrylic monomers, dissolved oxygen plays a crucial role [34]. The oxygen molecule can then be added to the propagating chain as follows:



The resulting $\text{R-M}_i\text{-O-O}^\bullet$ peroxy radical is known to be rather unreactive. Furthermore, *if* undergoing a reaction, these radicals are rather in favor to perform a radical-radical termination reaction [34].

At this point, it should be noted that in bulk polymerizations, dissolved oxygen is often removed prior to polymerization [34]. With respect to photoresists for 3D laser microprinting, the importance of dissolved oxygen in the photoresist on the printing process has been shown in a number of works [35, 36]. Importantly, the polymerization threshold dose D_{th} is inherently linked to the concentration of oxygen dissolved in the photoresist [37]. From this standpoint, in order to reduce the laser powers required for high-speed 3D laser microprinting [24], it would appear beneficial to reduce the polymerization threshold dose D_{th} by reducing the oxygen concentration in the photoresist [38]. However, in doing so, a loss in printing resolution is observed, and hence, this is not an attractive avenue [35, 37]. Notably, 3D printing into a photoresist also leads to spatial *gradients* in the oxygen concentration (see also section 5.2.4). This can in turn lead to, for example, increased linewidths and an impaired printing resolution [39]. In general, the loss in resolution in the proximity of other printed features is referred to as the *proximity effect*. The proximity effect especially can become a problem

when printing bigger structures; however, there are few publications addressing this phenomenon systematically in regard to 3D laser microprinting. An example of a loss in resolution due to oxygen depletion can be found in the appendix of this work in section [A.3](#).

2.3 MICROFLUIDICS

In the following section, I will briefly introduce the basic concepts of microfluidics. Microfluidic systems are particularly popular in the biomedical field, however, there is a vast range of other applications. This section relates to chapter [4](#) of this work, where a microfluidic injection system is integrated into a 3D laser microprinting setup.

The word “microfluidics” refers to the regime where fluidic systems are miniaturized. Within this regime of miniaturization, fluids often show unusual characteristics. Most notably, in fluidic channels with small inner diameters, fluids build up laminar velocity profiles, such that turbulences are absent. It should be noted that the following descriptions are a continuum theory for the involved fluids. Hence, the relevant size scale has to lie well above the size of individual molecules, such that the liquids involved can be treated as a continuum.

2.3.1 Definition of Viscosity

When shearing a body, the body “responds” with a shear stress τ . This response is quite dissimilar for fluids and solids: while for solids, τ commonly depends on the relative deformation, in fluids, the shearing force depends on the *rate* of deformation. This property of fluids, i.e., the resistance of fluids against shearing due to internal friction, is characterized by the viscosity.

More precisely, the viscosity is defined as follows: imagine two infinitely extended parallel planes, as depicted in [Figure 2.5](#). The space between the plates is filled with a thin layer of a liquid, and the upper plate moves into positive x -direction with a velocity u_0 . Due to the movement of the two plates relative to each other, the fluid experiences a shearing force. Newton’s law of viscosity is then given as

$$\tau_{yx} = \mu \frac{\partial u}{\partial y} , \quad (2.8)$$

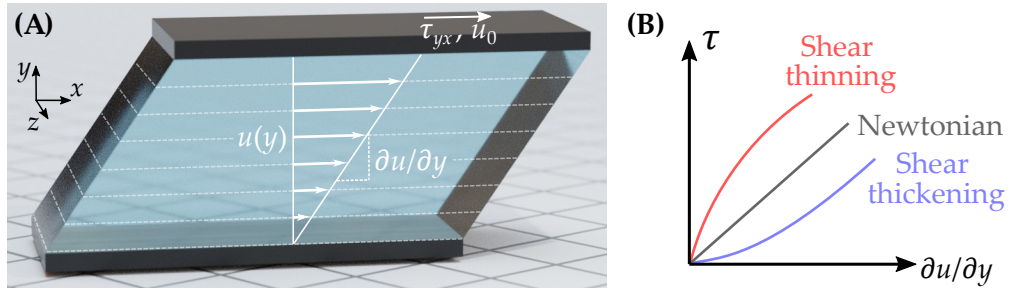


Figure 2.5: Definition of the viscosity. **(A)** A thin and incompressible fluid layer is located between two parallel plates. Upon moving the upper plate into $+x$ -direction with velocity u_0 , a linear velocity profile $u(y)$ builds up in the liquid (Couette flow). Due to internal friction, adjacent fluid layers experience a shear stress τ_{yx} that depends on the gradient $\partial u/\partial y$. **(B)** For Newtonian fluids, the relationship between the shear stress τ_{yx} and the gradient $\partial u/\partial y$ is linear, with the proportionality constant being the dynamic viscosity (see Eq. 2.8). Non-Newtonian fluids show a nonlinear relationship in this plot.

where τ_{yx} denotes the shear stress, $u(y)$ the velocity of the fluid in x -direction, and μ (units $[\mu] = \text{Pa s}$) the *dynamic* viscosity. Notably, for Newtonian fluids the relationship between τ_{yx} and μ is purely linear, which is not true for non-Newtonian fluids (see Figure 2.5(B)).

Furthermore, the dynamic viscosity is distinct from the *kinematic* viscosity, which is given as

$$\nu = \frac{\mu}{\rho}, \quad [\nu] = \text{m}^2 \text{s}^{-1} \quad (2.9)$$

and additionally depends on the mass density ρ of the fluid. However, throughout this work, the dynamic viscosity will commonly be used.

2.3.2 Turbulent vs. Laminar Flow

Generally speaking, the flow of liquids can be turbulent or laminar: whereas the streamlines in the velocity profile u of a laminar flow follow smooth paths, they appear to be chaotic in turbulent flow regimes. For predicting if a flow is turbulent or laminar, in fluid mechanics, the so-called Reynolds number is usually calculated [40]. For the case of a flow through a circular pipe, this quantity is given as

$$\text{Re} = \frac{\rho v d}{\mu}, \quad (2.10)$$

where ρ denotes the fluid's mass density, v the average velocity, and d the pipes' inner diameter. In a more physical sense, the Reynolds number resembles the ratio between viscous and inertial forces. With respect to the flow characteristics, for Reynolds numbers above a critical value $Re < Re_{\text{crit}}$, flows tend to be laminar, because viscous forces dominate. On the contrary, for $Re > Re_{\text{crit}}$ flows tend to be turbulent. A critical Reynolds number of $Re_{\text{crit}} = 2320$ has been determined experimentally [41].

It should be mentioned that this relationship is only a rule of thumb—and the experimental realization of fully developed laminar flows with $Re > Re_{\text{crit}}$ is possible.

2.3.3 The Hagen-Poiseuille Equation

In the following, I will give a mathematical description of a laminar flow through a circular pipe. More specifically, the aim is to derive the Hagen-Poiseuille equation, which connects the pumping pressure ΔP , applied to a circular pipe, to the resulting volume flow rate $Q = \dot{V}$.

In this context, it should be mentioned that different approaches for the derivation of the Hagen-Poiseuille equation can be found in literature: on the one hand, one avenue is to simplify the very complex Navier-Stokes partial differential equations for an incompressible flow, thereby introducing the very same approximations that I will also use below. I will pursue another avenue, which is the derivation by considering a balance of forces acting on an infinitesimal annular volume element in a circular pipe. The derivation goes along the lines of reference [42].

A sketch of a circular pipe, which exhibits an inner diameter R , is depicted in Figure 2.6(A). As the velocity profile $u(r)$ is assumed to be axisymmetric, it is convenient to employ cylindrical coordinates. Furthermore, the flow is assumed to be fully developed, such that its velocity profile $u(r)$ is stationary (i.e., $\partial u / \partial t = 0$). Lastly, the flow is assumed to be laminar, and hence, the velocity profile does not exhibit radial or azimuthal components.

In the following, the forces acting onto a infinitesimal annulus are split up as depicted in Figure 2.6(B). For setting up the differential force element dF_{left} , we consider the pressure p acting onto the surface $2\pi r dr$. In addition, we allow for a pressure gradient $\frac{\partial p}{\partial x}$ along x . The differential force element

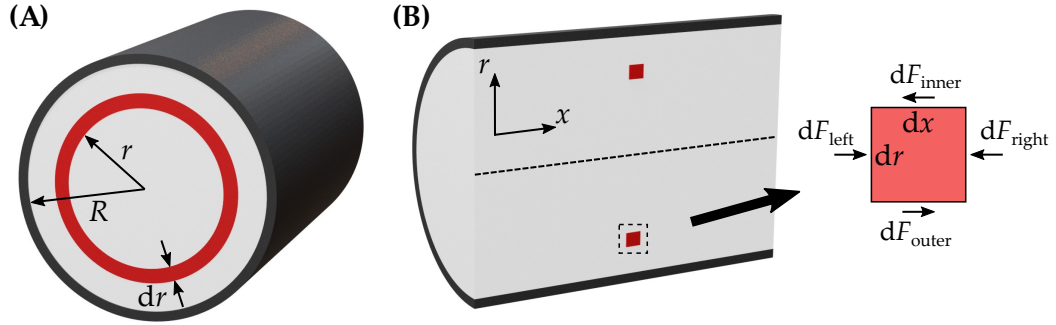


Figure 2.6: Sketches of a pipe with radius R and length l , filled with a viscous fluid that experiences laminar flow due to an applied pressure Δp . An infinitesimal annular volume is displayed in **(A)** as well as in the cross-sectional view of the pipe in panel **(B)**. The infinitesimal force elements required in the derivation of the Hagen-Poiseuille equation are indicated.

dF_{left} then reads

$$dF_{\text{left}} = \left(p - \frac{\partial p}{\partial x} \frac{dx}{2} \right) 2\pi r dr. \quad (2.11)$$

Likewise, the force element acting onto the right surface of the annulus can be written as

$$dF_{\text{right}} = - \left(p + \frac{\partial p}{\partial x} \frac{dx}{2} \right) 2\pi r dr. \quad (2.12)$$

For the inner and outer surfaces, only the differential force elements acting into $\pm x$ direction are considered. Here, forces stem from the viscosity, i.e., the resistance of the fluid itself against shearing. Hence, the differential force elements dF_{inner} and dF_{outer} can be expressed in dependence of the shear stress τ_{rx} as

$$dF_{\text{inner}} = - \left(\tau_{rx} - \frac{d\tau_{rx}}{dr} \frac{dr}{2} \right) 2\pi \left(r - \frac{dr}{2} \right) dx \quad (2.13)$$

and

$$dF_{\text{outer}} = \left(\tau_{rx} + \frac{d\tau_{rx}}{dr} \frac{dr}{2} \right) 2\pi \left(r + \frac{dr}{2} \right) dx. \quad (2.14)$$

As the flow is assumed to be fully developed, the sum of these forces has to vanish, i.e.,

$$dF_{\text{left}} + dF_{\text{right}} + dF_{\text{inner}} + dF_{\text{outer}} = 0. \quad (2.15)$$

Consequently, by plugging in the force elements and rearranging, one obtains

$$\frac{\partial p}{\partial x} = \frac{\tau_{rx}}{r} + \frac{d\tau_{rx}}{dr} = \frac{1}{r} \frac{d}{dr}(r\tau_{rx}). \quad (2.16)$$

Herein, the left-hand side of the equation only depends on x , whereas the right-hand side only depends on r . Hence, both sides have to be constant. Interestingly, one can directly conclude that the pressure p depends linearly on x . Multiplication with r and subsequent integration yields

$$r\tau_{rx} = \frac{r^2}{2} \left(\frac{\partial p}{\partial x} \right) + c_1, \quad (2.17)$$

with an integration constant c_1 . By rearranging and plugging in Newton's law of viscosity (eq. 2.8) one obtains

$$\mu \frac{du}{dr} = \frac{r}{2} \left(\frac{\partial p}{\partial x} \right) + \frac{c_1}{r}, \quad (2.18)$$

where μ denotes the dynamic viscosity. By integrating once more, the velocity profile u

$$u = \frac{r^2}{4\mu} \left(\frac{\partial p}{\partial x} \right) + \frac{c_1}{\mu} \ln(r) + c_2 \quad (2.19)$$

is obtained, with another integration constant c_2 .

For determination of the integration constants c_1 and c_2 , the following boundary conditions are considered: First, the fluid's velocity is assumed to vanish at the interface of the pipe, i.e., $u(r = R) = 0$ (this is a so-called no-slip boundary condition). Secondly, we require the velocity profile to be finite at all points in space. These boundary conditions imply $c_1 = 0$ and $c_2 = -\frac{R^2}{4\mu} \left(\frac{\partial p}{\partial x} \right)$, and the velocity profile can be expressed as

$$u = \frac{R^2}{4\mu} \left(\frac{\partial p}{\partial x} \right) \left(1 - \frac{r^2}{R^2} \right). \quad (2.20)$$

Consequently, the laminar flow in the pipe exhibits a *parabolic* velocity profile with respect to the radius r , as depicted in Figure 2.7.

Finally, the volume flow rate Q is obtained by evaluating the integral

$$Q = \int_0^R u(r) 2\pi r dr = -\frac{\pi R^4}{8\mu} \left(\frac{\partial p}{\partial x} \right). \quad (2.21)$$

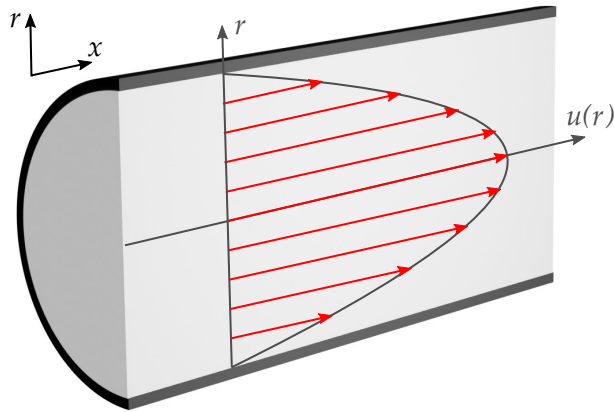


Figure 2.7: The laminar flow exhibits a parabolic velocity profile $u(r)$, which is plotted into a cross-sectional view of the pipe in this sketch.

Since the pressure p decays linearly with the length of the pipe (see eq. 2.16), the substitution $\frac{\partial p}{\partial x} = \frac{\Delta p}{l}$ can be plugged in and one arrives at

$$Q = \frac{\pi R^4 \Delta p}{8\mu l} \quad (2.22)$$

where Δp denotes the pressure drop along the pipe length l . This is the final result, i.e., the Hagen-Poiseuille equation.

Two things are to be noted: First, the flow rate resulting from an applied overpressure Δp heavily depends on the pipe's radius (proportional to R^4). The implications from this strong dependence will be discussed in detail in chapter 4 in the context of the design of a microfluidic injection system for 3D laser microprinting. Second, due to the formal similarity of the Hagen-Poiseuille equation with Ohm's law, laminar flow in a pipe is, for intuition, often compared with electrical conduction. Here, the electrical current I is the analogue of Q , and the voltage U the analogue of Δp . Thinking in this analogy can be helpful (for example, in section 4.2.5.3).

Part I

**MULTI-PHOTORESIST 3D LASER
MICROPRINTING**

3 Chapter 3

FLUORESCENT 3D SECURITY FEATURES

The counterfeiting of products and documents has a huge impact on economies and societies. A common way to ensure the authenticity of a product is the use of security features, which are designed for being difficult to copy. Consequently, the use of security features can help in recognizing product counterfeiting and document fraud, and can thus prevent resulting damage. Among the earliest forms of security features are stamp seals, which have already been in vivid use for centuries. They are typically impressed into a droplet of wax or into clay, and were used for authentication of documents. Obviously, due to considerable technological progress, the use of stamp seals has become largely obsolete in the meantime. And it is until today that also new types of security features share a similar fate: a certain type of security feature can only be used purposefully until a practicable and accessible method to circumvent it has been developed.



Nowadays, there is an ongoing technological race between two parties, with companies and authorities on one side, continuously bringing improved types of security features into use, in order to protect from economical or societal damage—and forgers on the other side, developing methods to circumvent those security features for their own interests.

In this chapter, I will present a novel type of security feature, which differs from the vast majority of previous security features in that it consists of

truly *three-dimensional* (3D) microstructures, as opposed to security features that are only manufactured by 2D or 2.5D fabrication methods and are thus easier to fake. These microstructures consist of *multiple photoresist materials* that exhibit different fluorescence properties. For readout and hereby for verification of the multi-material security features, confocal laser scanning microscopy (LSM) is employed.

While the use of these structures in terms of a security feature is a well-perceivable application of 3D laser microprinting, they are also interesting for their manufacturing process: herein, multiple sequential lithography steps are carried out, printing one photoresist material after another into one multi-material structure. The lessons learned from the fabrication of these structures also led to the development of the integrated multi-material 3D laser microprinting system that will be presented in the next chapter.

The work presented in this chapter has been carried out within a collaboration between employees of the company ZEISS (most importantly, Dr. Stefan Richter) and our group. All experiments presented have been carried out by me, including structure and photoresist development, structure fabrication, and characterization. The original idea for pursuing this project resulted from a joint effort between our group and the ZEISS employees.

3.1 INTRODUCTION

Generally speaking, security features should fulfill two basic requirements: first, the security feature has to be very difficult to fake. In order to achieve this, many approaches make use of advanced or highly specialized fabrication methods. Hence, expensive machinery and detailed process knowledge is required in order to copy the security feature. Second, there has to exist an efficient method for readout, thus enabling the verification of authenticity of the security feature. Depending on the exact realization, readout can potentially require a specialized device.

In order to take a short look at the design principles of common security features, it is quite instructive to briefly discuss security features from everyday life: a good and conceptually rather simple example is the use of microprinting on banknotes. Here, text is printed onto the bank note at very small font sizes. Subsequently, in this case, the counterfeiting security stems from the simple fact that “normal” digital printers that most people do have access to simply couldn’t print it due to limited printing resolution. Thus, to copy the security feature, more specialized printing machinery would be

required. Besides this rather simple example, there exists quite a variety of security features based on 2D printing methods, such as the printing of optically variable ink [43–45]. Here, special pigment particles are aligned during printing using magnetic or electric fields, giving the printed letters an optical appearance that is dependent on the viewing angle. Optically variable ink is commonly found on Euro banknotes and has seen wide use throughout the last decades. For both of these two examples—microprinting and optically variable ink—verification of authenticity is quite simple, as both of these examples do not need highly specialized tools for readout, and can be performed by employing a magnifying glass, or even looking at them with the bare eye.

With growing need of more forgery-proof security features, the field of security features based on 2D fabrication methods has naturally seen quite a development of novel approaches. In particular, today, computer-generated holograms are ubiquitously employed, some of which require specialized devices for verification of authenticity [46, 47]. They are usually fabricated by planar fabrication methods such as combinations of electron-beam lithography and hot embossing. A further notable field of ongoing research is the use of luminescent particles that exhibit characteristic spectral fingerprints and are difficult to synthesize [48–53]. For verification, these approaches usually rely on spectroscopic devices for readout. Finally, another approach based on 2D fabrication methods is the use of plasmonic structures that can be read out using Raman spectroscopy [54, 55].

So far, I have only discussed two-dimensional security features. In contrast, three-dimensional fabrication methods offer a higher degree of complexity and thus an increased level of counterfeiting security. Along these lines, first concepts have been proposed [56] and methods for 3D optical data storage exist that can be employed as security features [57–60].

A different approach towards unforgeable security features are so-called physical one-way functions. In contrast to the previous discussion, these approaches do not rely on highly advanced specialized fabrication methods, but instead on the characterization and subsequent fingerprinting of physically highly complex systems. In this context, for example, 3D light-scattering samples have been characterized by recording laser speckles [61]. These samples typically consist of dielectric light-scattering particles, embedded into a transparent matrix at random locations. Along the same line, stochastically distributed quantum dots in 3D printing inks have been demonstrated [62].

Finally, invisibility cloaks in diffusive light-scattering media could be reinterpreted in terms of security features [63]. These structures are virtually

invisible for stationary incoherent illumination and detection, but can be uncovered by detecting their transient response [64] or by an analysis of laser speckles [65].

3.2 3D SECURITY FEATURE DESIGN

3D laser microprinting offers the possibility to fabricate truly three-dimensional micro- and nanostructures that could not be fabricated with other fabrication methods. It is therefore standing to reason to use this prerequisite for the fabrication of advanced and highly forgery-proof security features.

A conceptual rendering of the security feature we developed is depicted in Figure 3.1, which consists of a three-dimensional microstructure that is 3D-printed from multiple materials with different fluorescence properties: it features a non-fluorescent support structure, which incorporates a 3D cross-grid surrounded by walls for mechanical support. The walls have a thickness of 5 μm and incorporate holes, which are for drainage of liquid photoresist and organic solvents during the fabrication procedure. Most importantly, fluorescent markers with different emission colors are distributed in the 3D cross-grid in a targeted manner. The total width of the whole three-dimensional microstructure by design is 112 μm , and the height is 54 μm . It could therefore be embedded into a thin layer of plastic foil and integrated into a security label. Security labels typically consist of an adhesive tape that cannot be removed from a surface without destroying it.

The structure itself features 845 different positions onto which fluorescent markers can be purposefully 3D-printed: in the structure, the markers are arranged in five layers which are spaced by 9 μm . Each of these layers contains 13×13 markers with a lateral spacing of 7.5 μm . Figure 3.1 hence only displays one possible configuration of markers. Depending on the number of different fluorescent emission colors employed, a certain number of different states can be realized for each marker position and information can be stored in the security feature.

In order to read out the security feature, it is necessary to detect the fluorescence signal for every single marker position in the security feature. For this purpose, confocal laser scanning fluorescence microscopy (LSM) is chosen, since this technique enables optical sectioning and thus the acquisition of truly three-dimensional fluorescence micrographs.

From a distant point of view, one could be tempted to compare the

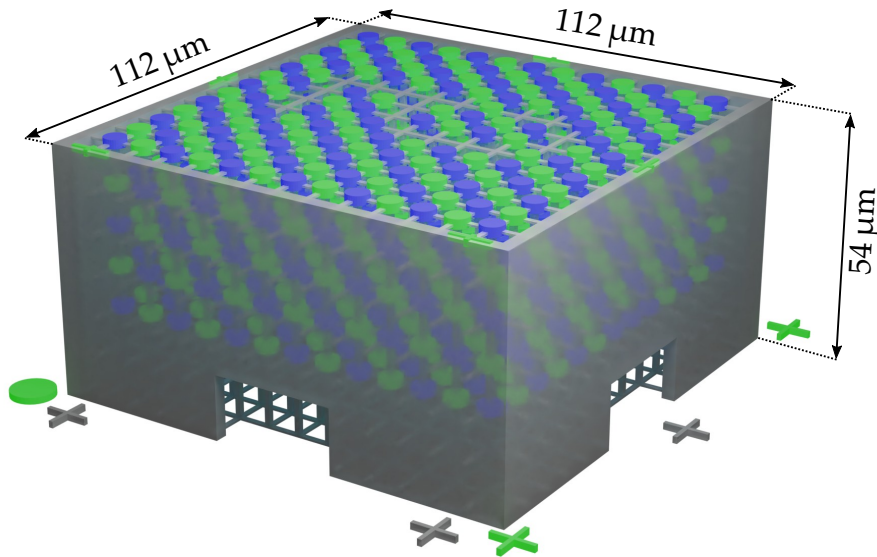


Figure 3.1: Design for the three-dimensional fluorescent security feature proposed in this work. It consists of a non-fluorescent 3D backbone, which acts as a mechanical support, and markers printed into it, which fluoresce in different colors. The width of the full 3D structure is comparable to the thickness of a human hair. Adapted from [66] with permission.

microstructure proposed here with well-known approaches from optical data storage, that could be also reinterpreted in terms of a security feature [57–60]. However, these approaches are quite dissimilar in that they usually rely on the direct inscription of dots into a transparent solid material, thus locally altering the optical material response in terms of light scattering or fluorescence. In comparison, 3D laser microprinting potentially allows for a greater spectrum of different material responses within one structure by sequential additive manufacturing of multiple materials into one single structure. Typically, these approaches inspired by optical data storage aim for a high amount of information that can be stored in a small volume. With respect to security features, an ultimately high information density is not the ultimate goal in the end. The approach in this work rather offers, due to the use of 3D printing, great flexibility in terms printable materials with different optical responses, and thus the possibility to print very complex and hence forgery-proof 3D microstructures.

The amount of information that can be stored in the security feature depends on the number of fluorescence colors that are printed into the

microstructure: for example, when employing two different fluorescent emission colors, for each marker position there are 3 different possible states (color A, color B or no marker). This equals to ≈ 1.6 bit of information stored per marker position in this case. Overall, the amount of information that can be stored in the structure scales proportional to $\log_2(N + 1)$, where N is the number of fluorescent colors. Taking into account all the different marker positions, the whole microstructure can store 1.3 kbit of information, at an information density of 3.1 Gbit/cm³. For comparison, in the field of optical data storage, information densities on the order of 100 Gbit/cm³ can be realized [60]. While both the absolute amount of information stored as well as the scaling behavior with increasing number of different fluorescent emission colors might seem unfavorable from a standpoint where the microstructure should be actually used as a storage device, this point is not of importance when designing a microstructure that is to be used as a security feature.

3.3 SAMPLE FABRICATION

The vast majority of 3D microstructures that is commonly fabricated using 3D laser microprinting consist of one single material—in contrast to this work, where the structures are to be printed from a number of different materials with different fluorescence properties. Thus, in the fabrication routine, it is necessary to build up the microstructures from the different photoresists in sequential 3D printing steps. Similar multi-step lithography procedures have been employed in other publications, primarily in studies on cell cultivation in 3D printed microstructures [2, 25], but also for the fabrication of optical components, responsive materials or micro-robots [3, 9, 13, 21, 67, 68]. However, typically, these structures are significantly less complex in their geometry.

In this section, I will describe the details of the photoresists for printing, and the fabrication workflow itself.

3.3.1 *Fluorescent Photoresist Containing Quantum Dots*

For the experimental realization of the microstructure design shown above, there is the necessity of having non-fluorescent and fluorescent photoresists at hand. Thus, I have designed the photoresists such that the basic ingredients, i.e., monomers and photoinitiator, show no or merely weak fluorescence. Furthermore, fluorescent colloidal quantum dots (and in chapter 4

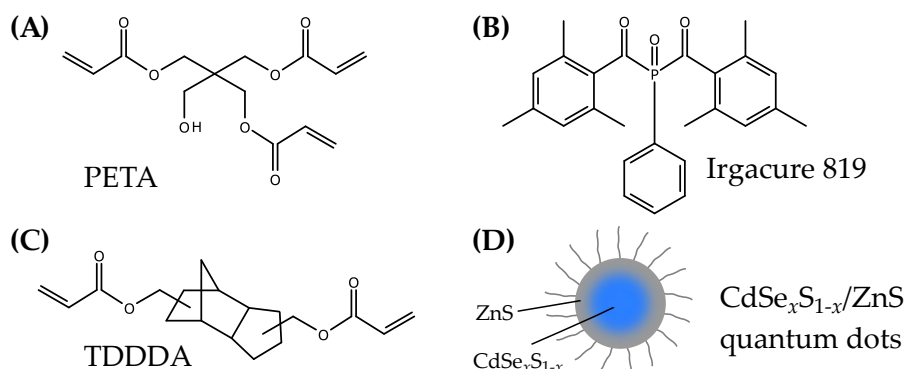


Figure 3.2: Chemicals used in the photoresists. **(A)** Monomer: pentaerythritol triacrylate (PETA). **(B)** Photoinitiator: Irgacure 819, selected due to its low fluorescence quantum yield. **(C)** Monomer: tricyclo[5.2.1.0^{2,6}]decanedimethanol diacrylate (TDDDA), selected for better stability of the quantum dots in the photoresist. **(D)** Colloidal semiconductor quantum dots. The non-fluorescent resist uses (A)-(B), whereas the fluorescent resists use (A)-(D).

also chemical fluorescent dyes) are added to specifically add fluorescence properties, such that the polymerized photoresists forms a quantum dot polymer nanocomposite. This section summarizes the basic considerations that had to be met when designing the photoresists. A detailed overview of all resist compositions can be found in the appendix (section A.1.1).

The components of the non-fluorescent photoresist are depicted in Figure 3.2 (A) to (B) and the components of the fluorescent resists in Figure 3.2 (A) to (D). In particular, the non-fluorescent photoresist only includes two ingredients: A monomer and a photoinitiator. As monomer, the trifunctional pentaerythritol triacrylate is used. This monomer is commonly used in resists for 3D laser microprinting since it shows advantageous writing properties and enables the fabrication of 3D microstructures with a high resolution [31]. In the selection of the photoinitiator, particular attention is paid to the fluorescence quantum yield, which should ideally be as low as possible. This quantity is defined as the ratio between the number of photons emitted by fluorescence and the number of photons absorbed. Judging by this figure of merit, among common photoinitiator molecules, Irgacure 369 and Irgacure 819 are suitable with quantum yields on the order of $\leq 0.2\%$ [69]. Throughout this thesis, Irgacure 819 has been employed in all photoresists at a mass concentration of 2% with respect to the monomer.

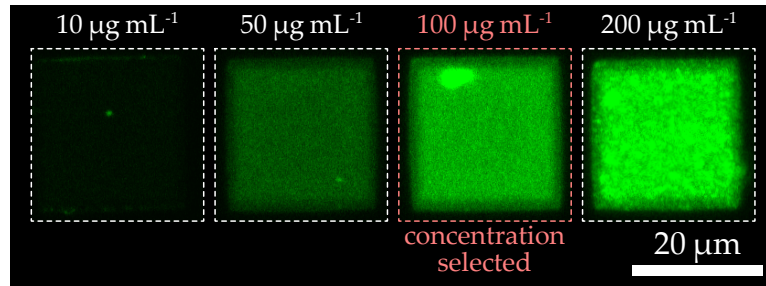


Figure 3.3: Different concentrations of quantum dots in photoresist emitting at $\lambda_2 = 525 \text{ nm}$. Using photoresists with different concentrations of quantum dots, blocks were printed next to each other on the same substrate. The different blocks have been printed onto one single substrate, such that they can be imaged within one single fluorescence image. Naturally, brighter fluorescence is observed for higher concentrations of quantum dots. For the highest concentration, significant formation of agglomerates is observed, which is not favorable. Thus, quantum dot concentrations in the order of $100 \mu\text{g mL}^{-1}$ are used.

The fluorescent photoresists contain two additional components: as fluorescent additives, commercial colloidal semiconductor CdSeS/ZnS core-shell quantum dots with different emission colors are dispersed in the photoresist. Core-shell semiconductor quantum dots were selected in favor of organic dyes due to their bright fluorescence and their excellent stability versus photobleaching [70]. Another favorable property of quantum dots is that their fluorescence emission bands are typically spectrally sharper as compared to organic dyes. This facilitates spectral multiplexing, as spectral overlap of the different emission spectra is easier to avoid.

To achieve a better dispersion and therefore in order to avoid the common problem of agglomeration of the quantum dots in the photoresist, the non-polar monomer tricyclo[5.2.1.0^{2,6}]decanedimethanol diacrylate (TDDDA) is contained at a mass concentration of 50%. A non-polar environment is a purposeful choice in this case because the quantum dots exhibit a non-polar oleic acid surface functionalization. Furthermore, its refractive index $n = 1.506$ is similar to the one of PETA, which avoids strong optical aberrations in later sequential 3D printing steps (see section 3.3.2). More details on the photoresist preparation can be found in the appendix in section A.1.1.

In order to determine a reasonable concentration of quantum dots, simple blocks (dimensions $25 \times 25 \times 20 \mu\text{m}^3$) were printed from different photore-

sists onto one single substrate. Fluorescence images of these blocks taken by LSM are shown in Figure 3.3. For recording these images, an excitation wavelength of $\lambda_{\text{exc}} = 405 \text{ nm}$ is used. All blocks shown are recorded in one single image. As expected, the observed fluorescence intensity increases with increasing concentration of quantum dots. However, for the highest concentration shown ($200 \mu\text{g mL}^{-1}$) the formation of quantum dot agglomerates is observed in the printed structures. Thus, the highest concentration that still appears to be spatially homogeneous in fluorescence is selected, which is $100 \mu\text{g mL}^{-1}$.

At this mass concentration, a mean distance between quantum dots of $\approx 200 \text{ nm}$ can be roughly estimated from the quantum dot's mass density. In other words: for the 3D laser microprinting setup employed in this work, the voxel size lies in the range of $(450 \text{ nm})^3$ —and hence, one can expect a single voxel to contain on average ≈ 11 quantum dots. However, if one was using high-resolution 3D laser microprinting techniques (like STED-inspired approaches [31]) in order to reduce the structure size of the fluorescent microstructures, it could become necessary to increase the concentration of quantum dots in the photoresist.

3.3.2 Printing Routine

For the fabrication of the fluorescent microstructures, subsequent printing of the different parts of the structure from the different photoresists is necessary. The fabrication sequence is outlined in Figure 3.4. First, the non-fluorescent support-grid is printed with the non-fluorescent photoresist, depicted in gray. In this step, alignment markers are additionally printed onto the substrate, which enable spatial alignment in the subsequent printing steps. After the initial printing of the support structure has been accomplished, the sample is taken out of the lithography machine and the unpolymerized photoresist is washed off by washing consecutively in acetone and isopropyl alcohol. The sample is then dried under a gentle flow of nitrogen.

Afterwards, the fluorescent markers are then printed into the structure in the next step: for this purpose, a fluorescent photoresist is drop-casted onto the substrate with the already printed support structures. The photoresist hereby fills up the already existing structures, and the holes in the walls of the support structures ensure that no air bubbles remain inside. The sample is then installed again in the 3D printer. An alignment procedure

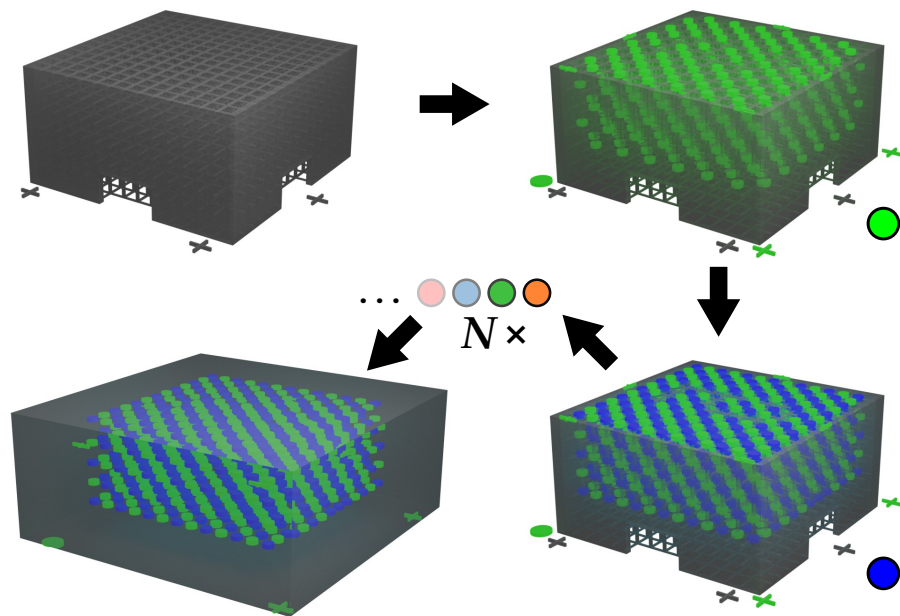


Figure 3.4: Manufacturing routine of the 3D microstructures. First, a non-fluorescent 3D cross-grid is printed from a non-fluorescent photoresist. Afterwards, fluorescent markers can be distributed in the structure in subsequent 3D printing steps using photoresists with different fluorescence colors. This step can be repeated with a variety of different photoresists. In between each printing step, it is necessary to remove excessive photoresist from the sample and to apply the next one. Finally, the sample is encapsulated into transparent polymer, protecting it from damage. Adapted from [66] with permission.

is performed subsequently, such that the parts printed in the next step are well-positioned with respect to the non-fluorescent support structure, and the printing process is performed.

Depending on the number N of different fluorescent colors in the structure, this sequence—washing off unpolymerized photoresist and printing the next one—is repeated several times. At this point, it should be highlighted that for the quantum-dot containing photoresists, an *additional* washing step in a stirred toluene bath for 5 to 10 min is carried out, which effectively removes quantum dots sticking to surfaces of non-fluorescent parts of the structures.

Finally, the resulting structure is embedded in a transparent polymer film with a thickness of $100\ \mu\text{m}$, using again the non-fluorescent photoresist and curing it using flood illumination by a UV lamp.¹ This embedding serves as

¹ UVAHAND 250, Dr. Hönle AG

a mechanical protection from the environment, and furthermore provides refractive index matching which facilitates readout.

In this context, there is a notable difference between 3D laser microprinting and many other 3D printing techniques. Using 3D laser microprinting, it is possible to print through already printed material. Therefore, when printing the 3D fluorescent security features, for each material, all parts of the individual material can be printed in one single step. For most other approaches, such as many stereolithography-inspired printing techniques, it is *not* possible to print through already printed material. In this case, for each z-slice of the structure, all photoresists would have to be printed consecutively, which would result in an enormously high number of photoresist exchange steps that would be necessary for printing a structure like the fluorescent 3D security feature.

Still, also for 3D laser microprinting, there are certain requirements and limitations when printing through already printed material: first, and most importantly, light-scattering has to be avoided during printing. In order to do so, the refractive indices of the already printed material and of the liquid photoresist to be printed should not differ strongly: otherwise, the quality of the writing focus suffers, in turn impairing the quality of the printed structures or even making printing impossible. In case of the security features, this requirement is reasonably fulfilled with a difference in refractive indices between photoresists and the already printed structures on the order of $\Delta n = 0.02$ [71]. Second, printing all structure elements from every single photoresist in one step is only possible if the height of the structure does not exceed the working distance of the objective lens. In case of the fluorescent 3D security features, this is not an issue, since the height of the security features ($54\ \mu\text{m}$) is way smaller than the working distances of objective lenses commonly used in 3D laser microprinting.

Specifically, the structures shown in this chapter are printed using a “sandwich” writing scheme. This arrangement is explained in Figure 3.5. Most commonly, in 3D laser microprinting the so-called dip-in configuration is used, where the objective lens is dipped directly into the photoresist. In this case, the photoresist thus serves as both the immersion medium as well as the printing “ink”. This writing scheme is displayed in Figure 3.5(A). In contrast, using the sandwich writing scheme as displayed in Figure 3.5(B), the photoresist is sandwiched between two substrates spaced by a distance of $100\ \mu\text{m}$. The objective itself is dipped into conventional immersion oil, such that the objective lens does not have to be cleaned after the individual

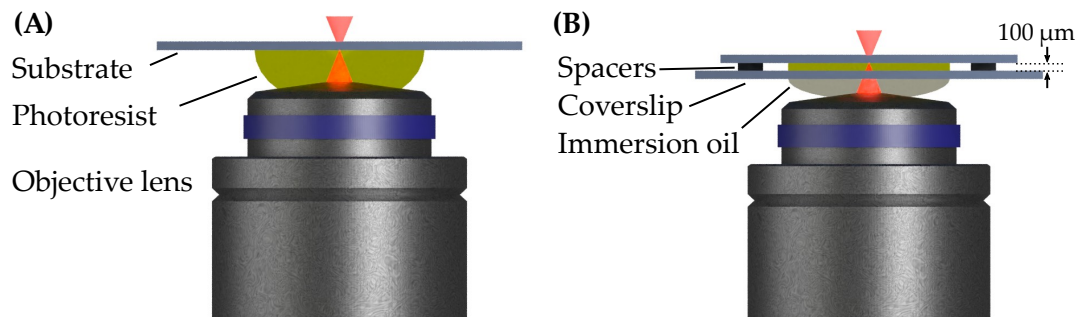


Figure 3.5: **(A)** Dip-in Lithography: conventionally, in 3D laser microprinting, the objective lens is dipped directly into the index-matched photoresist, enabling the fabrication of structures not limited by the free working distance of the objective lens. **(B)** In contrast, here, the photoresist is sandwiched between two parallel coverslips that are spaced by $100\ \mu\text{m}$, and the objective lens is immersed into conventional immersion oil.

writing steps in different photoresists. However, writing the security features from the different photoresists, it is necessary to open the sandwich after each printing step in order to develop the sample and to apply the next photoresist. All fluorescent security features presented in this chapter have been printed in the presented sandwich configuration, using a $63\times/1.40$ objective lens.² This configuration has also served as a starting point for development of the integrated multi-material printing system presented in the following chapter 4.

3.4 FLUORESCENCE MICROSCOPY ON FABRICATED STRUCTURES

For the 3D fluorescent security feature to be effective, there must be an efficient possibility for readout of the information stored inside the microstructure. Since the fluorescent markers inside the microstructure form a truly three-dimensional arrangement, for readout of the structures, also an experimental method has to be chosen that reflects this property. Therefore, confocal laser scanning fluorescence microscopy (LSM) has been selected, since this method allows for optical sectioning along the optical axis and thus for the retrieval of 3D fluorescence image data.

² Plan-Apochromat $63\times/1.40$, Carl Zeiss

3.4.1 One Emission Color

For microscopy, a commercial LSM³ is used, which is equipped with a number of laser lines for excitation, a set of filters for discrimination of fluorescence signals, a set of different objective lenses, and different detectors. In particular, it features two photomultiplier tubes, such that two different fluorescence signals can be recorded simultaneously.

Fluorescence images recorded from a sample written using two photoresists (i.e., one fluorescent color) are depicted in Figure 3.6. For imaging, a droplet of immersion oil is applied onto the samples, which are embedded in a transparent polymer film as described in section 3.3.2, and an oil-immersion objective lens is used.⁴ Typically, image stacks of ≈ 150 images with a spacing of $0.37\ \mu\text{m}$ along the z -axis are taken. Further experimental details can be found in the appendix (section A.2.2).

To obtain an intuitive visualization of the measured data, 3D reconstructions are calculated from the entire image stacks using the software Imaris. Such a 3D reconstruction, showing iso-intensity surfaces, is depicted in Figure 3.6(A). In this 3D reconstruction, it is clearly visible that the five layers of markers printed from the photoresist fluorescing at 525 nm have been printed evenly. In particular, it is also visible that the different markers can still be discriminated axially as well as laterally, even if almost every possible marker position is occupied. The tooth-like shape of the individual markers stems from the non-fluorescent 3D cross-grid into which the fluorescent markers are printed.

Raw fluorescence images and their respective z -positions in the microstructure are shown in Figure 3.6(B): specifically, the layer of the substrate and the five different layers with fluorescent markers are displayed. In these images, the image brightness is equally normalized with respect to the peak section intensity I_n , which is the mean intensity of the brightest image taken in the image stack. This image normalization is chosen since it depends less on the precise z -bounds for recording the image stack, as opposed to a normalization with respect to the global mean intensity. From these images, one can conclude that for one fluorescent emission color this structure can in fact be nicely written—but more different fluorescent colors would increase structural complexity and hence also counterfeiting security further.

³ LSM 510 Meta, Carl Zeiss

⁴ Plan-Apochromat 63 \times /1.40, Carl Zeiss

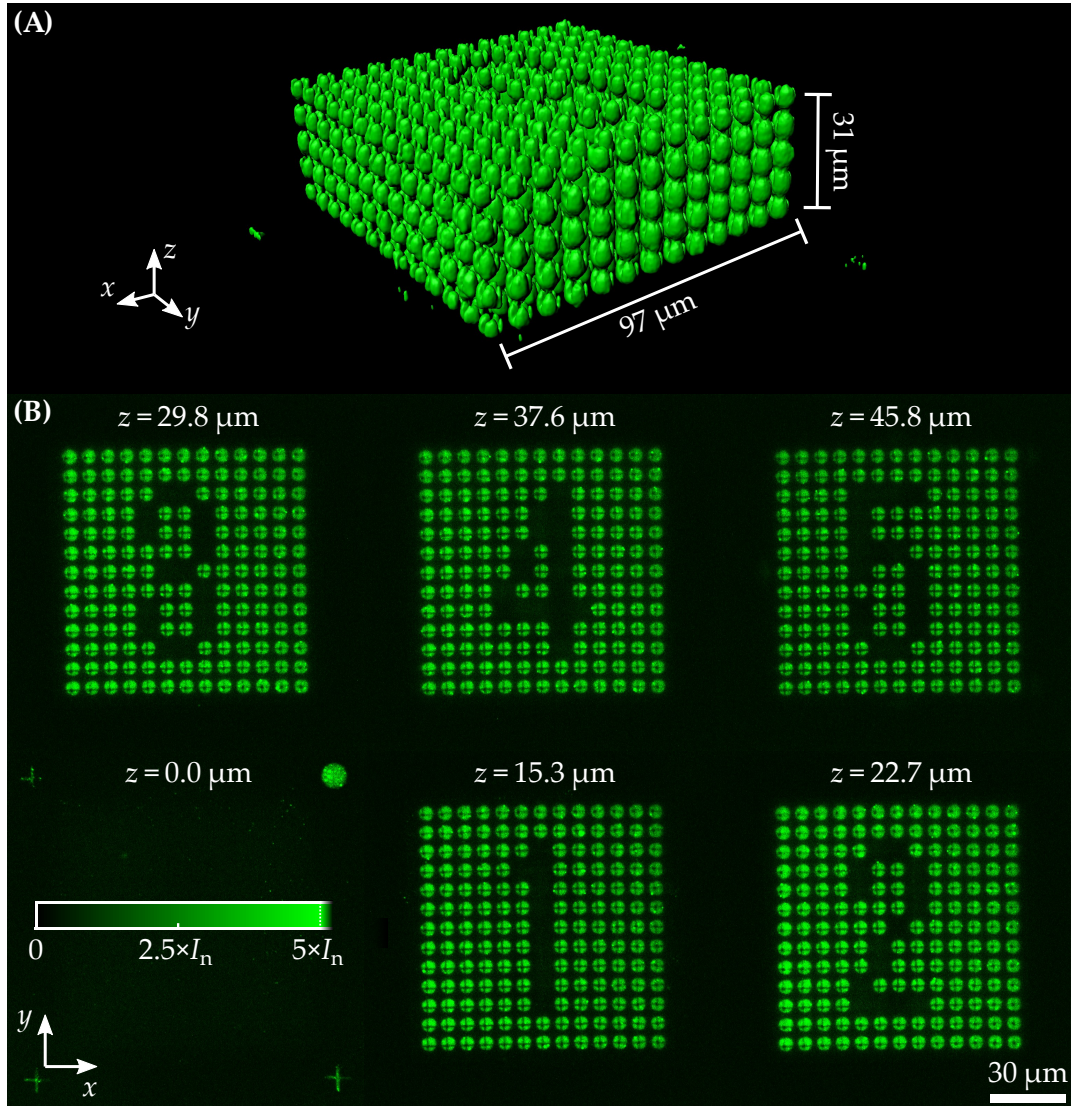


Figure 3.6: Laser scanning fluorescence microscopy images of a 3D security feature printed using a non-fluorescent and a fluorescent photoresist. The fluorescent photoresist contains colloidal quantum dots emitting at a wavelength of $\lambda_1 = 525$ nm. **(A)** 3D reconstruction calculated from the whole fluorescence image stack taken, showing isointensity surfaces. The five layers of fluorescent markers are clearly visible. The tooth-like shape of the individual markers stems from the non-fluorescent support structure. **(B)** Fluorescence image sections for different z -positions in the sample, showing the different layers of fluorescent markers. The intensities are normalized with respect to the peak section intensity I_n . Adapted from [66] with permission.

3.4.2 Two Emission Colors

To increase the complexity of the 3D fluorescent security features, structures comprising more than one fluorescent colors were printed, still following the fabrication routine described in section 3.3.2. In analogy to Figure 3.6, a microstructure printed from *three* different photoresists rather than two is depicted in Figure 3.7. For imaging this sample, both fluorescence channels are imaged simultaneously, as described in the appendix (section A.2.2).

The respective test patterns in the individual layers have been chosen such that they exhibit a high occupation of possible positions with fluorescent markers, since this renders to be the most difficult case for printing as well as for readout. In particular, during printing, two problems may arise due to a high density of markers: first, due to the proximity effect, markers printed from the fluorescent photoresist may touch each other. Second, due to a high filling fraction of printed material, exchanging the photoresists inside the microstructures could become a problem during the fabrication routine, due to blocking of flow paths inside the microstructure. This would result in badly printed fluorescent markers, and the writing parameters have been optimized such that these cases do not occur.

For further examination, the fluorescence intensities, averaged per image section (i.e., averaged over xy), are plotted over z in Figure 3.8. Panels (A) and (B) refer to the structures shown in Figures 3.6 and 3.7, respectively. In particular, in these intensity curves, there is a distinct decrease in fluorescence intensity visible in between the individual layers of markers. This is a good indication that the fluorescent markers have been 3D printed with a good separation in z -direction, even for the printed test pattern where almost every marker position is occupied. Like in Figures 3.6 and 3.7, the intensity curves are normalized with respect to I_n for each color of fluorescence.

From all the fluorescence images of single layers taken, as well as from the 3D reconstructions shown in Figures 3.6 and 3.7 and the intensity curves in Figure 3.8, one can conclude that the microstructures have been written in a well-resolved manner, can be read out, and show homogeneous fluorescence brightness across the complete structures.

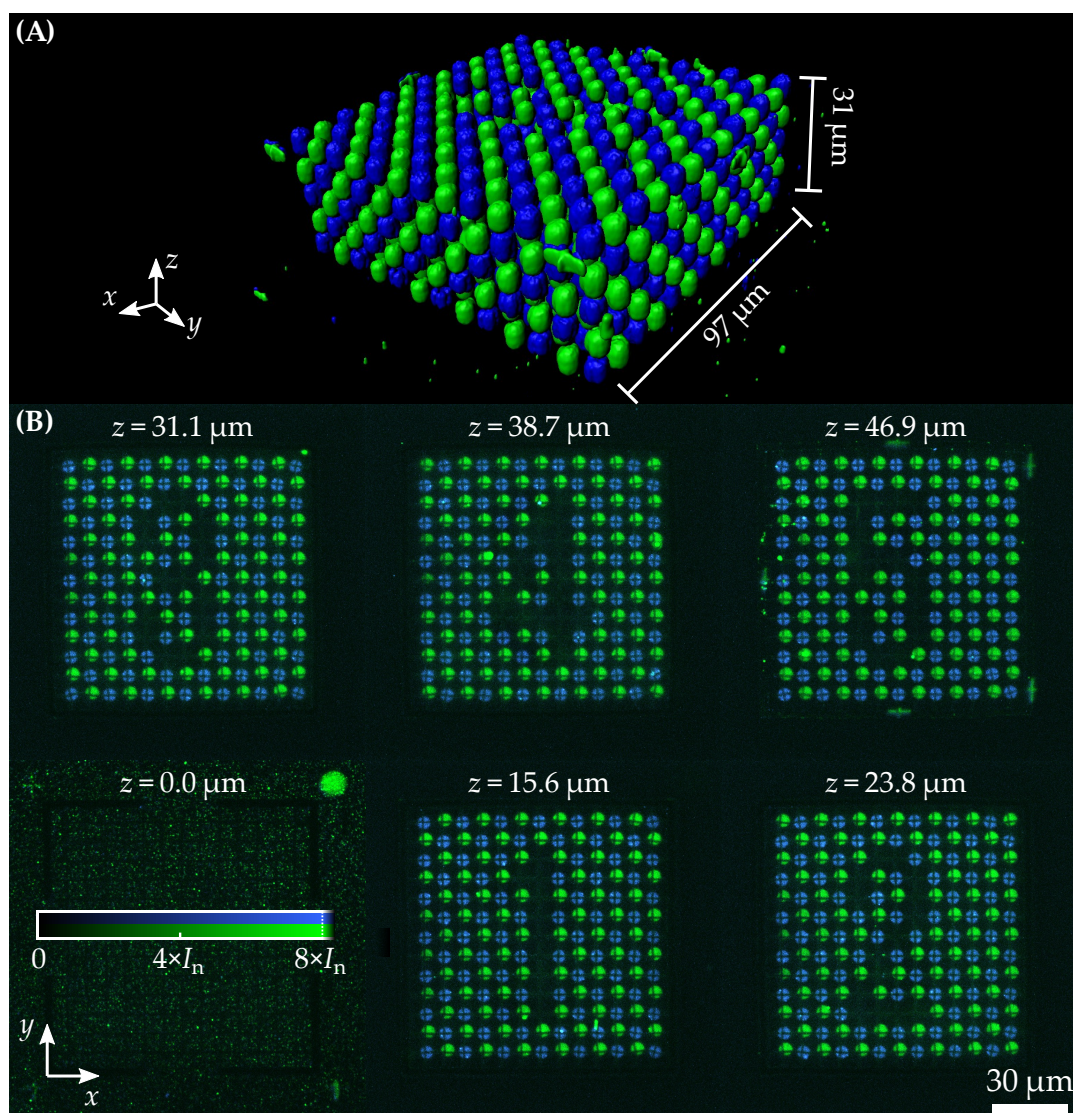


Figure 3.7: Same as Figure 3.6, but sample printed using two different fluorescent photoresists, emitting at $\lambda_1 = 525\ \text{nm}$ and $\lambda_2 = 450\ \text{nm}$. The different fluorescent materials have been printed in a well-defined manner. Adapted from [66] with permission.

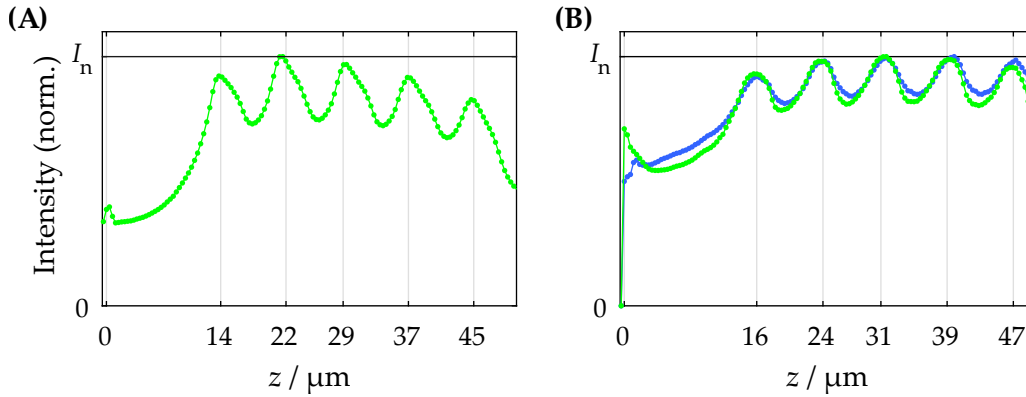


Figure 3.8: Average fluorescence intensities per image section for the samples shown in (A) Figure 3.6 and (B) Figure 3.7. The z -positions of the raw fluorescence images shown in these Figures are indicated, respectively. The fluorescence intensities are normalized to the peak section intensity I_n , respectively, which is the average intensity of the brightest slice in the particular image stack.

3.4.3 Fluorescence Stability

... During Readout

When using the fluorescent microstructures as a security feature, a high stability against degradation processes would be desirable. Therefore, experiments were carried out to test the stability against photobleaching. Photobleaching is the degradation of fluorescence intensity over time, when the fluorophore is continuously excited by light. While this process is primarily observed in chemical dyes, colloidal semiconductor quantum dots usually exhibit a vastly increased resistance against photobleaching [70].

To test the stability of our structures, continuous readout using the LSM was carried out on printed microstructures. For this purpose, the excitation laser was scanned continuously over the sample in a small regions of interest for an extended period of time, while recording images regularly to observe the change in fluorescence intensity. These experiments are depicted in Figure 3.9. Here, panel (A) refers to a structure that has been stored for 6 months under atmospheric conditions and has not been encapsulated. In contrast, panel (B) refers to a structure that has been encapsulated, and that was tested directly after fabrication. For the non-encapsulated sample,

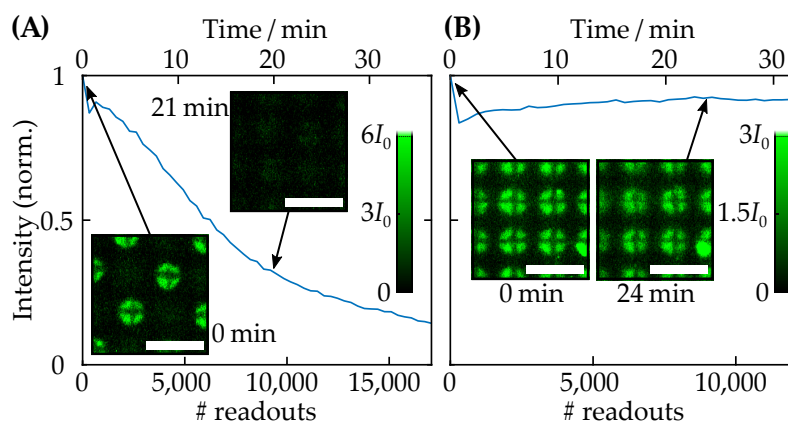


Figure 3.9: Observed fluorescence intensity over time. To examine fluorescence stability, small regions of interest of the printed microstructures were read out continuously. The excitation power was $155 \mu\text{W}$ at 405 nm . The scale bars in the insets have a length of $10 \mu\text{m}$. Panel (A) refers to a non-encapsulated structure, and (B) to an encapsulated one. While there is a significant decrease in fluorescence intensity observed over a couple of thousand readouts observed for (A), structure (B) shows high stability. The slight variations in (B) observed at early times are due drifting of the sample. Adapted from [66] with permission.

a significant decrease in fluorescence intensity is observed over a period of half an hour, corresponding to almost 15000 readouts in the LSM. In contrast, the encapsulated sample remains stable over a time period of 12000 readouts. These findings indicate that the embedding of the samples may not only serve as a protection from mechanical damage and for index-matching during imaging, but also for protection against chemical influences from the atmosphere (i.e., oxygen). In any case, a couple of thousand readouts seem sufficient for using the fluorescent microstructure as a security feature—and even the structure shown in Figure 3.9(A) should already exhibit sufficient stability for this application.

... During Printing

Further conceivable degradation of the quantum dots could already occur during the writing process where the photoresist is exposed by the means of two-photon induced polymerization. All in all, there are two possible processes that could lead to a degradation of the quantum dots that are contained in the formed polymer quantum dot composite: first, the polymerization takes place under chemically harsh conditions, and the radicals

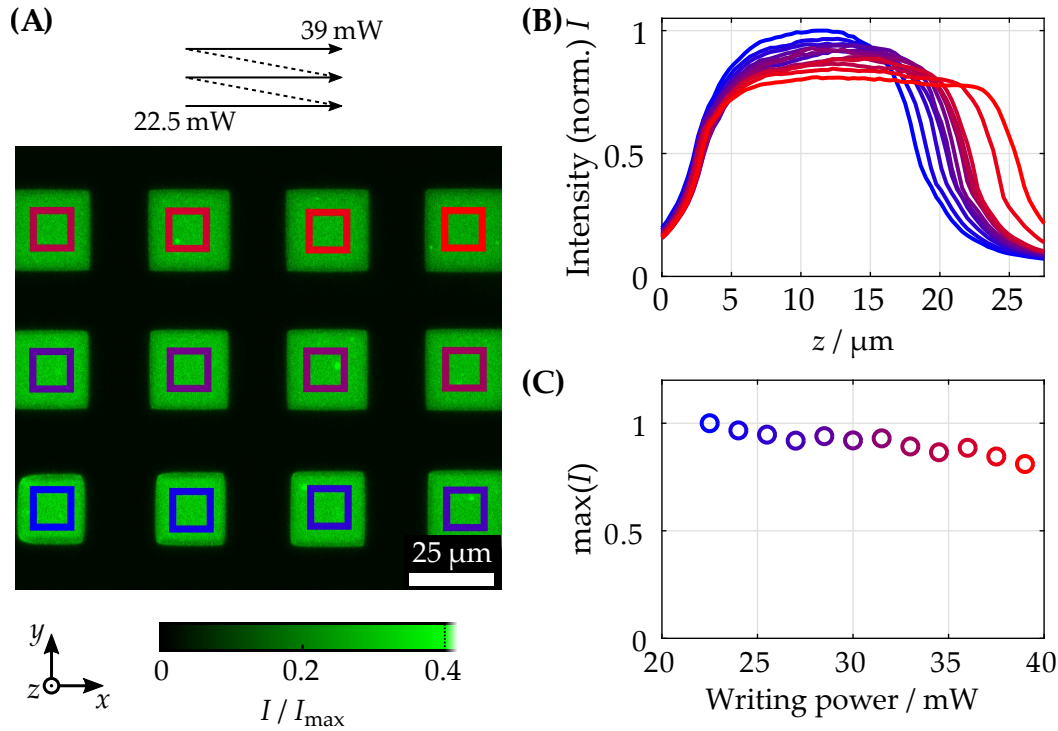


Figure 3.10: Testing of potential degradation of quantum dots during writing. Blocks ($25 \times 25 \times 20 \mu\text{m}^3$) were written with increasing power of the writing laser (22.5 to 39 mW) and observed in the LSM. **(A)** Raw fluorescence image of an array of blocks, normalized with respect to the intensity I_{max} of the brightest pixel contained in the image. Regions of interest (ROIs) are indicated by small rectangles. **(B)** Fluorescence intensity profiles plotted over z , obtained by averaging over xy for each ROI in (A). **(C)** Peak intensities from (B) in dependence of the writing power. A moderate decrease in fluorescence intensity is observed with increasing writing power, which can be explained by a lower density of quantum dots for higher writing powers due to reduced shrinkage.

present during polymerization could potentially also react with the passivating polymer and semiconductor layers around the core-shell quantum dots. Such processes could generate surface defect states, thereby leading to a decrease of the quantum yield and thus to a decrease of the observed fluorescence intensity. Second, colloidal semiconducting quantum dots typically exhibit a significant two-photon absorption cross-section [72]. Consequently, one has to assume that the quantum dots have already seen some exposure during the writing process of the printed microstructures.

Hence, to examine if there is a significant degradation of the quantum dots during writing, a series of small blocks (25 μm side length, 20 μm height) was written with different powers of the writing laser, increasing from 22.5 to 39 mW, and a constant scan speed of 5 cm s^{-1} . Then, the fluorescence intensity of these blocks was examined in the LSM. All blocks were printed in close proximity to each other onto the same substrate and were imaged within one field of view of the LSM. The results from these experiments are depicted in Figure 3.10.

Figure 3.10(A) shows a single fluorescence image of the block array—however, the actual 3D image stack taken in the LSM covers the whole volume of the structures. In this fluorescence image, small rectangles indicate the regions of interest (ROIs) for analysis in the following steps. The intensity normalization of the fluorescence image is with respect to the intensity of the brightest pixel I_{max} contained in this image. By averaging the image intensity values over x - and y -direction for each ROI, intensity profiles can be plotted over z as shown in panel (B). The colors of these curves match the colors of the corresponding ROIs in (A). In these intensity profiles, two effects are visible: first, with increasing power of the writing laser, the widths of the intensity profiles increase. Second, with increasing power of the writing laser, a slight decrease of the maximum value of the intensity profiles is visible, as plotted in panel (C).

While the decrease in fluorescence intensity might appear to be linked to a degradation of the quantum dots caused by increased writing powers, it can actually also be explained by shrinkage: after writing, the polymer shrinks during the development process. For common PETA-based photoresists, the linear shrinkage usually takes values on the order of 5 to 10 %, depending on the exposure power employed. Reduced shrinkage at higher exposure powers is, in addition to an increased voxel size, a main contributor to the increased width in z -direction of the fluorescence profiles plotted in (B). Regarding fluorescence intensity, shrinkage after polymerization is a key factor because it increases the spatial density of quantum dots in the quantum dot-polymer composite. And since higher writing powers lead to a lower shrinkage, this is a viable explanation for the observed variations.

In summary, for typical powers of the writing laser employed throughout this work, a significant degradation of the quantum dots caused by the 3D printing process could not be observed in this experiment.

3.5 CONCLUSION

In this chapter, I have presented a novel type of security feature. In particular, this type of security feature consists of three-dimensional microstructures that fluoresce in different colors. These microstructures consist of a three-dimensional non-fluorescent backbone, into which markers with different colors of fluorescence are printed in a three-dimensional arrangement of positions. In order to experimentally realize the different colors of fluorescence, within the fabrication workflow, multiple different photoresist materials containing colloidal quantum dots with different emission wavelengths are 3D printed sequentially into one single structure. Readout and thereby the verification of authenticity of these security features is carried out by confocal laser scanning microscopy, which enables the imaging of the structure in three dimensions. Since the fluorescence properties in the security features are realized by the incorporation of core-shell semiconductor quantum dots, fluorescence of these structures proves to be resistant against photobleaching.

Consequently, these 3D fluorescent microstructures could practically be employed as security features: in particular, they are fabricated by a highly developed fabrication technique (i.e., 3D laser microprinting) which makes them difficult to fake. Moreover, they can be designed to be durable against mechanical damage and photobleaching. Finally, verification of authenticity is efficiently possible by fluorescence microscopy, which could be integrated into a portable readout device.

Within this chapter, the sequential 3D printing of different photoresist materials required plenty of manual processing. In particular, with increasing number of different materials to be printed into one structure, this manual processing increasingly becomes painful and prone to errors. Even in a streamlined workflow in the laboratory, exchanging one photoresist by another during fabrication roughly required half an hour of manual processing, before printing the next photoresist could be pursued. For the structures shown in this chapter, in contrast, printing the fluorescent markers only required a couple of *seconds* of printing time. As a result, only an unfavorably small fraction of time is actually used for printing the structures. Consequently, an increased amount of automation and improved fabrication strategies would be desirable. In this context, the work presented within this chapter has served as a starting point for the development of the integrated multi-material 3D laser microprinting system that will be presented in the

next chapter. Herein, the security feature structures from this chapter will serve as a “drosophila” for this new system, and multi-material structures composed of up to five different photoresists printed at reduced structure sizes will be presented.

4 INTEGRATED MULTI-MATERIAL 3D LASER MICROPRINTING

In contrast to two-dimensional inkjet printers, parallel printing of several different printing inks is not possible in 3D laser microprinting—here, just one single printing ink, i.e., one photoresist, can be printed at a time. Just like in chapter 3, this implies that for the fabrication of multi-material structures, multiple sequential printing steps are necessary, with processing steps in between for removing excessive photoresist and applying the next one. While it is of course possible to carry out all these steps in a manual fashion, this excessive manual processing not only becomes increasingly painful for structures composed of *many* materials, but also a major source for fabrication defects. Motivated by the work on three-dimensional fluorescent security features, these problems led us to re-thinking the fabrication of multi-material, i.e., multi-photoresist structures using 3D laser microprinting.

In this chapter, I will present a microfluidic injection system that was built as an add-on onto an existing commercial 3D laser microprinting system (Nanoscribe Professional GT). This combination effectively constitutes a fully integrated multi-material 3D printer, capable of 3D printing almost arbitrary

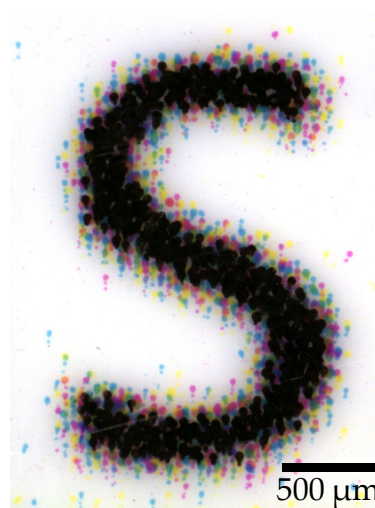


Figure 4.1: As opposed to conventional inkjet 2D printers (microscope image above), most 3D printers are limited to *one single* printing ink within one printout.

multi-material microstructures. The central part of this experimental setup is a specialized sample holder incorporating a microfluidic chamber. The chamber is filled with photoresist, and structures can be printed into it. During printing, the chamber can be flushed with different photoresists and organic solvents, which enables in-situ printing of different photoresist materials. Thus, this system vastly facilitates the fabrication of multi-material structures by eliminating any manual processing steps during the printing process, and allows for the fabrication of highly complex multi-material microstructures. As benchmark structures, fluorescent security features composed of five different fluorescent photoresist materials are presented.

Unless indicated otherwise, all experiments in this chapter have been carried out by me. The original idea for developing a system for photoresist exchange was developed by Martin Wegener and myself. While the basic concept of the sample holder incorporating the microfluidic chamber has been conceived by me, the detailed computer-aided design (CAD) drawings of this part were prepared together with our technician Johann Westhauser.

4.1 INTRODUCTION

The following section is meant to give a brief overview of approaches and concepts that have been published in regard to 3D printing of multi-material structures. This overview will be limited to purely *optical* 3D additive manufacturing methods.

Nowadays, 3D laser microprinting is a fabrication technique that has been commercially available for over a decade—and while a number of multi-material structures have already been published by our and other groups [2, 9, 13, 21, 25, 67], previous to our work [73], there have been no publications on integrated multi-material 3D laser microprinting.

At the same time, though, there has already been a number of publications on systems for multi-material printing in the field of (projection-based) stereolithography. Most commonly, this has been realized by printing into exchangeable vats which are filled with different photoresists [74–77]. Furthermore, combinations of stereolithography and projection-based 3D printing with a fluidic deposition system for multi-material printing have previously been demonstrated [78–80]. However, here, structures composed of only two different materials were demonstrated. Finally, an implementation making use of a flow chamber for the fabrication of objects has been published [81], which enables the manufacturing of 2.5D structures. In conclusion, although

there have been a number of publications on multi-material printing in the field of stereolithography, usually structures consisting of only two materials or 2.5D structures (i.e., topographies instead of 3D structures) are presented. Furthermore, stereolithography does not allow for the same printing resolution as 3D laser microprinting. Hence, the realization of the multi-material microstructures (composed of five photoresists) that will be presented at the end of this chapter would not have been possible with these systems.

Notably, combinations of lithography with microfluidics have previously been published [82–86], and the fabrication of micro- and nanoparticles by polymerization of photoresist in microfluidic channels has been demonstrated in this context. However, most commonly, those systems are designed for the fabrication of microparticles that consist of *one single* photoresist. In this context, however, also the fabrication of particles composed of two different materials has been demonstrated [83]: in particular, lithography is carried out into a parallel co-laminar flow of two different photoresists. This results in a material transition along one spatial direction within the fabricated particles. In summary, these approaches do not allow for the fabrication of almost *arbitrary* multi-material 3D structures.

Further publications on similar fabrication strategies for micro-stereolithography and 3D laser microprinting have also appeared after our article [73] was published [68, 87–89]. A recent review on multi-material printing for a variety of different (also non-optical) 3D printing techniques can be found in [90]. Further examples are shown in [1, 91].

Another notable avenue for the fabrication of complex multi-material microstructures is the printing of different material properties from one single photoresist. This approach is therefore distinct from the one presented in this work, where different photoresists are employed to achieve different printed materials. For the former, development of photoresists that are selective towards ambient or exposure conditions (for example, selective towards the intensity or wavelength of the writing laser) is necessary. Along these lines, multi-component mechanical microstructures incorporating parts with different mechanical properties have been realized. In these works, conventional commercial photoresists are employed, and mechanical properties are tuned by changing the exposure dose during writing, which is also called gray-tone lithography [92–94]. However, these approaches are typically highly specialized and hence limited in terms of the different material properties that can be 3D printed from one resist. In contrast, the microfluidic injection system can be used in combination with almost any available photoresist, and hence a wide range of material properties is readily attainable.

4.2 EXPERIMENTAL REALIZATION

In this section, I will describe the experimental realization of the microfluidic injection system developed in this work. I will start by giving an overview of the setup, and by highlighting the most important design restrictions that led to the specific realization presented in this work. Subsequently, I will feature the most important components of the microfluidic system in more detail. Finally, I will discuss the flow characteristics of the system based on the Hagen-Poiseuille equation.

4.2.1 Overview of the Microfluidic Injection System

A schematic overview of the microfluidic injection system is depicted in Figure 4.2. For pumping the different liquids through the fluidic system, pressure-driven microfluidics is used. Here, an electronic pressure controller¹ is used to simultaneously apply a defined overpressure to liquid containers, which are filled with the different liquids to be pumped. The electronic pressure-controller itself is fed with an overpressure from a nitrogen bottle, and hosts a piezo-actuated proportional valve monitored by a gas pressure sensor. The liquid containers feature outlet tubings dipping into the liquids in the containers. Hence, the overpressure applied to the containers acts as a driving force for ejecting all the liquids at the same time. To achieve control over the pumping of individual liquids, the outlet tubes from liquid containers are connected to a home-built selection valve. This part hosts solenoid valves at each input port and hence enables to switch each flow path coming from the liquid containers on and off. In the selection valve, all flow paths are furthermore combined into one before being guided into the microfluidic chamber, and eventually into a waste container. In between the selection valve and the microfluidic chamber, an overpressure valve is installed in order to protect the microfluidic chamber from any possible overpressure that could potentially lead to damaging the chamber. In the flow path of one of the solvents, a flow resistor is installed to artificially increase flow resistance of the low-viscosity solvent (see section 4.2.5.3).

In particular, pressure-driven microfluidics is employed in this system because it can be easily extended in terms of the number of liquids that can be pumped. For the system presented in this chapter, pumping of up to ten

¹ Elveflow OB1 MK III, 0 to 8 bar

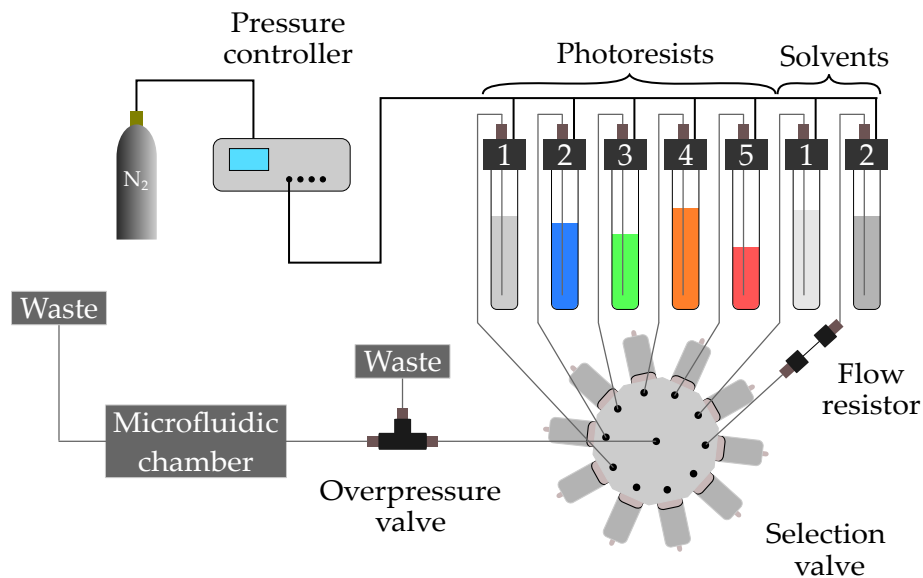


Figure 4.2: Schematic overview of the microfluidic setup: in pressure-driven microfluidics, an electronic pressure controller is used to apply a gas overpressure to different liquid containers simultaneously. This overpressure serves as the driving force for pumping the different solvents and photoresists. A selection valve combines all the different output tubes from the containers into one flow path and allows for the selective pumping of individual liquids. The liquid flow is then guided through an overpressure valve, and eventually into the microfluidic chamber. Excessive liquid is gathered in waste containers, respectively. Adapted from [73] (CC BY 4.0).

different liquids is possible, only limited by the number of solenoid valves installed at the selection valve. Also, when using fluidic components that are sensitive to overpressures, using pressure-driven microfluidics can be advantageous, since the pressure applied to the system is directly controlled. However, as opposed to the case of using syringe pumps, quantities like the volume flow rate are not inherently known and hence have to be measured or calculated. Other advantages of pressure-driven microfluidics include a vastly increased flow stability and a better responsivity; however, are of lesser interest for the injection system.

4.2.2 Basic Design Guidelines

For the practical realization of a microfluidic injection system for multi-material 3D laser microprinting, there are a number of difficulties that have to be considered. Hence, the following section is meant to give a quick overview over the main considerations to be met in the design phase.

The microfluidic sample holder is meant to host the microfluidic chamber into which samples can be printed, and to be flushed with different photoresists and solvents during the printing routine. The printing arrangement that was used for the fabrication of three-dimensional fluorescent security features in chapter 3 serves as the starting point for designing this part. This arrangement is depicted in Figure 4.3: Here, a droplet of photoresist is placed between two coverslips, which are spaced by a distance of 100 μm . Printing into the chamber formed by the space between the two coverslips is carried out by using the objective lens in oil-immersion mode, as described in section 3.3.2. While panel (A) for clarity is not drawn to scale, in panel (B), the thickness of the coverslips is to scale with respect to the dimensions of the objective lens and its working distance.

From this scheme shown in Figure 4.3(A), one important design constraint becomes immediately clear: The fixed working distance of the high-NA oil-immersion objective lens used for printing imposes a geometrical restriction: the maximum realizable height of the chamber is ultimately limited by the full working distance of the objective lens used, minus the thickness of the coverslip onto which oil-immersion is carried out. In turn, the height of the chamber given by the distance of the two coverslips ultimately limits the maximum height of microstructures that can be printed into the chamber. The microfluidic sample holder presented in this chapter is designed to be compatible with the high-NA objective lens Plan-Apochromat 63 \times /1.40, Carl Zeiss, which is commonly used in combination with the Nanoscribe Professional GT printer and features a full working distance of 360 μm . When performing oil-immersion using a conventional coverslip with a thickness of 170 μm , thus, a free working distance of 190 μm remains when subtracting the thickness of the coverslip.² In the following, the height of the chamber will be fixed to 100 μm , which is sufficient to fit in the fluorescent security features from chapter 3 into the microfluidic chamber, and leaves enough safety distance to avoid crashing the objective lens into the sample holder.

² Note, however, that the sample holder will later also be used with another objective lens (LD LCI Plan-Apochromat 63 \times /1.2 Imm Korr DIC, Carl Zeiss).

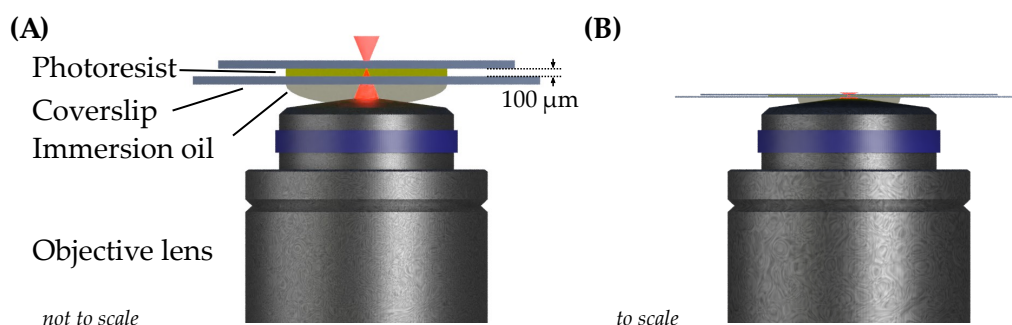


Figure 4.3: The “sandwich” writing mode used in chapter 3 serves as a starting point for conceiving the microfluidic sample holder. Here, the photoresist is sandwiched between two glass substrates, and the objective lens is used in combination with regular immersion oil. For clarity, panel (A) is *not* drawn to scale, while in (B), the thickness of the coverslips is to scale with respect to the dimensions and the working distance of the objective lens.

Particular attention in the design of the injection system also has to be directed towards the viscosity of the photoresists to be used. While some photoresists can exhibit smaller viscosities comparable to water, other resists do have a very high viscosity. As an example, the common monomer PETA has a dynamic viscosity μ between 0.6 and 1 Pa s at a temperature of 25 °C—comparable to the viscosity of honey.³ In general, highly viscous fluids are problematic for the injection system because they inherently lead to high necessary pumping pressures to achieve a given volume flow rate. High overpressures are in turn unfavorable in combination with the thin glass windows employed in the microfluidic chamber. Furthermore, consecutive injection of fluids with a large difference in their dynamic viscosities (for example, a highly viscous photoresist followed by a low-viscosity solvent) can impose a difficulties that will be addressed in section 4.2.5.3.

At the same time, the swept volume, i.e., the volume of photoresist that has to be flushed through the microfluidic system when performing a photoresist exchange step, is also of major interest. To reduce unnecessary consumption of photoresist, this quantity should be minimized. The inner diameters of all fluidic components used should therefore be kept as small as possible. However, smaller inner diameters inherently lead to strongly increased flow resistance: for a laminar flow in a circular pipe, the flow resistance scales with d^4 , where d is the inner diameter of the pipe (see section 2.3.3). This

³ Data taken from <https://www.union-pigment.com/china/radiation-curable-3524.html>, accessed on June 14th, 2020.

results in a trade-off between swept volume and the required pumping pressures.

Finally, after printing a photoresist material using 3D laser microprinting, unexposed photoresist is removed from the microfluidic chamber by flushing with organic solvents such as acetone, isopropyl alcohol or toluene. Hence, all components have to be built from materials that are chemically resistant to common substances employed in this step. This implies that for all polymeric wetted parts, fluorinated polymers or polyether ether ketone (PEEK) are the materials of choice.

4.2.3 *The Microfluidic Sample Holder*

The arguably most important part of the microfluidic injection system is the sample holder, hosting the microfluidic chamber into which samples are eventually 3D printed. In this section, the practical implementation of such a sample holder, realized in the scope of this thesis, will be presented. The most important design guidelines for this part have already been discussed in section 4.2.2.

A schematic of the microfluidic sample holder is displayed in Figure 4.4. For clarity, this drawing is not to scale. Figure 4.5 shows a to-scale cross-sectional exploded view of the actual model. The sample holder is fabricated from stainless steel by the means of CNC milling.⁴ In order to put in and take out substrates for printing structures onto, it is possible to open the sample holder. In particular, it features a top part, hosting a larger glass window (24 mm diameter, 170 μm thickness) on the objective side, and a bottom part, hosting the smaller glass substrate (10 mm diameter, 170 μm thickness) onto which structures are printed. The two parts are sealed by an O-ring (14 \times 1.78 mm made from FEP-encapsulated⁵ Viton, Eastern Seals Ltd.). The glass substrate is intentionally chosen to be substantially smaller than the glass window for practical purposes in the design.

In addition, the lower part of the sample holder features microfluidic input and output ports. Hence, conventional microfluidic tubings with an outer diameter of 1.59 mm can be directly connected to it using conventional 1/4''–28 flat-bottom flangeless fittings.⁶ Typically, for good chemical com-

⁴ All metal parts were milled by our institute's mechanical workshop.

⁵ FEP: Fluorinated ethylene propylene

⁶ For example: XP-235X, IDEX Health & Science

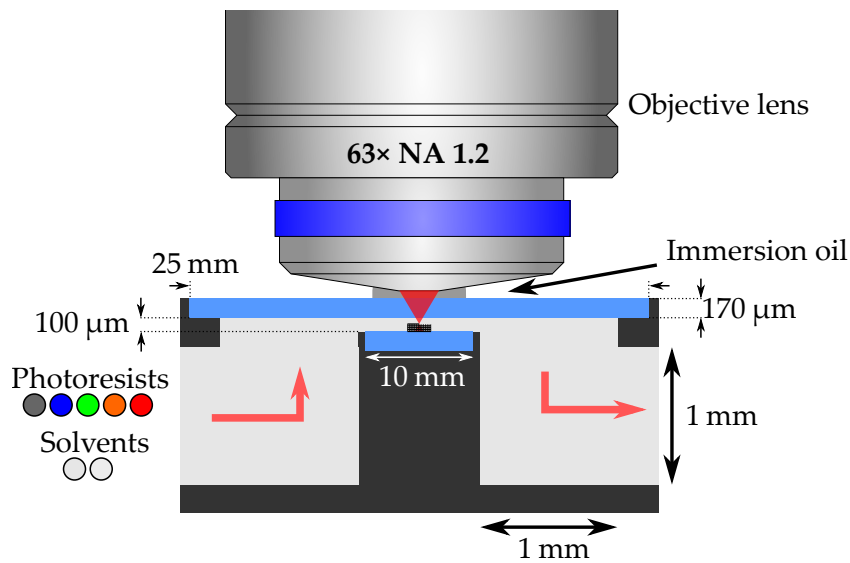


Figure 4.4: Schematic cross-sectional view of the microfluidic sample holder, incorporating the microfluidic chamber. The sample holder features input and output ports for connecting the microfluidic tubing. It also hosts a substrate with a diameter of 10 mm onto which structures are printed. A glass window in parallel to the substrate, spaced by 100 μm , allows for writing inside the chamber using common oil-immersion objectives. An important consideration for the design of this sample holder were tight space restrictions, stemming from the finite working distance of high-NA objective lenses commonly used for 3D laser microprinting, and from limited space in the 3D printer. The chamber design, as shown here, allows for the printing of structures with a maximum height of 100 μm . Adapted from [73] (CC BY 4.0).

patibility, connectors made from PEEK together with ferrules made from ETFE⁷ and microfluidic tubing made from PTFE⁸ or FEP are employed.

For assembly, the glass window on the objective side is glued permanently to the upper part of the sample holder. For this purpose, an epoxy glue⁹ is used, since it is resistant against most organic solvents (including isopropyl alcohol, acetone and toluene) and provides strong bonding of the glass coverslip to the stainless steel part. In case the glass window has to be replaced, it can be removed again by soaking the glue in dichloromethane.

⁷ ETFE: Ethylene tetrafluoroethylene

⁸ PTFE: Polytetrafluoroethylene

⁹ UHU plus endfest 300, UHU GmbH & Co. KG

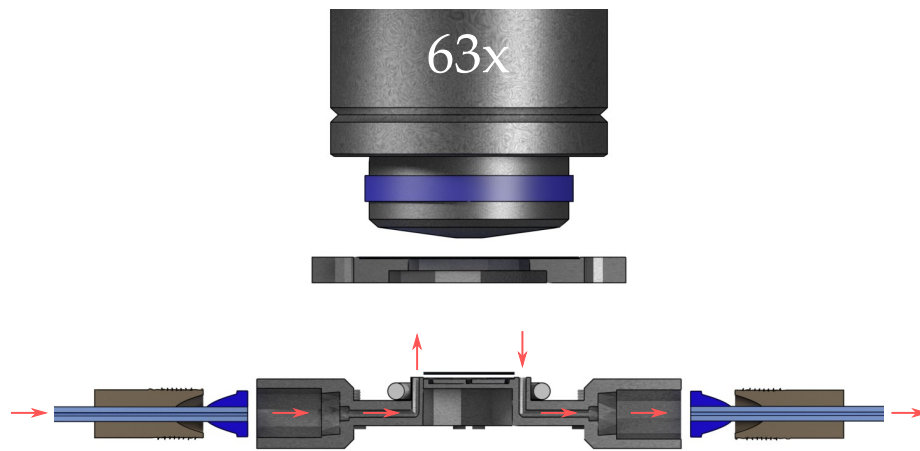


Figure 4.5: CAD model of microfluidic chamber, cross-sectional exploded view. The chamber's top part features a glass window for the objective lens to look into the chamber, and the bottom part holds the small substrate onto which structures can be printed. In addition, the bottom part features liquid connectors. A chemically inert O-ring in between seals the chamber. Adapted from [73] (CC BY 4.0).

Similarly, for printing, the small glass substrate inside the chamber is temporarily glued into the sample holder using a tiny droplet of photoresist¹⁰, which is cured by UV light. The gluing does not have to resist strong forces in this case, but it should be easy to remove the substrate from the sample holder after printing. Using IP-S for gluing, it was possible to take out the substrate by removing it mechanically from the sample holder using tweezers.

During normal operation of the microfluidic system, the microfluidic chamber itself is not expected to experience a significantly increased pressure as compared to the surrounding, since microfluidic tubing with a relatively large inner diameter of 1 mm is attached to its output port. However, since the glass window is very thin (170 μm) and breaking of the glass window would lead to photoresists and organic solvents being spilled into the 3D printing system, tests were carried out to minimize the probability of this scenario. In this context, one case where the microfluidic chamber may in fact experience significant overpressure would be a situation where the output port of the microfluidic chamber is clogged. In this case, for intuition,

¹⁰ Nanoscribe IP-S

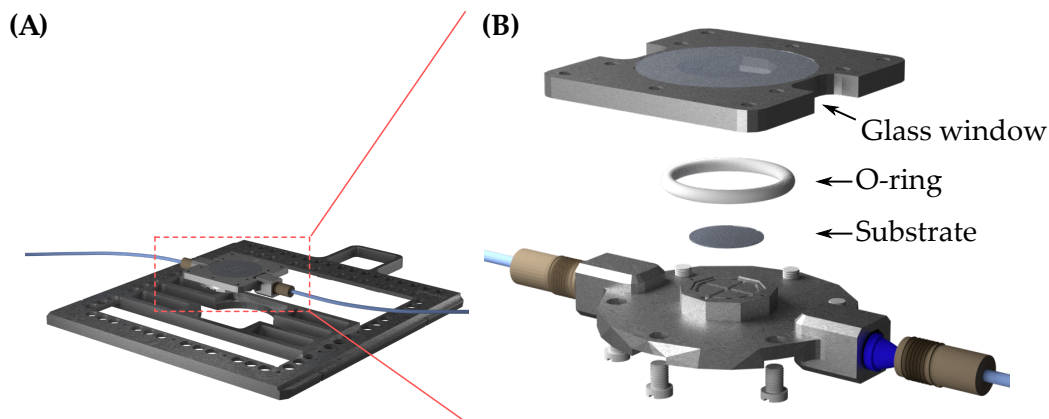


Figure 4.6: **(A)** Computer rendering of the fully assembled sample holder, including the outer frames to fit it into the commercial 3D printer. **(B)** Exploded view of the inner part of the microfluidic sample holder. Adapted from [73] (CC BY 4.0).

if an overpressure of 2 bar was applied to the chamber, a glass window with a diameter of 15 mm would experience a force of about 35 N.

In particular, for measuring the critical overpressure up to which the glass window is stable, an overpressure was applied to the chamber using the electronic pressure controller and increased until the glass window burst. This test was repeated for a number of glass windows. Typically, the glass windows exhibited a critical overpressure of over 3 bar, with the most stable glass windows resisting pressures of up to 4.5 bar. Consequently, for pumping, overpressures above 2 bar are never applied, which should render the thin glass window safe. In addition, an overpressure valve is connected to the input flow path of the microfluidic chamber, which consists of a back pressure regulator¹¹ connected to a T-piece¹² (as displayed also in Figure 4.2). This part protects the microfluidic chamber from overpressures exceeding 1.4 bar, which could potentially occur if the output flow path of the chamber was blocked.

¹¹ P-791, IDEX Health & Science

¹² P-612, IDEX Health & Science

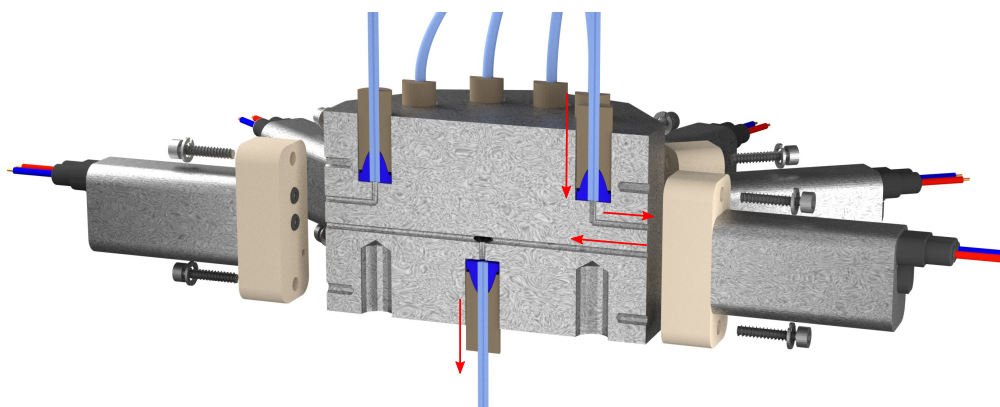


Figure 4.7: Computer rendering of the home-built 10-to-1 selection valve assembly (cross-sectional view). It consists of commercial solenoid valves mounted on a custom-made manifold piece. Using this arrangement, liquid input flows from ten different flow paths can be switched on and off individually. The flow paths are eventually combined into one and then guided into the microfluidic sample holder. The swept volume of this part is 49 μL . Adapted from [73] (CC BY 4.0).

4.2.4 The Selection Valve

In the microfluidic system, liquids are pumped from the respective containers by applying a pneumatic nitrogen pressure to them. Since the system makes use of only one electronic pressure controller, it is only possible to pressurize all liquid containers present in the system at the same time, as discussed in section 4.2.1 and as indicated in Figure 4.2. Pumping of an individual liquid is only possible by blocking all the output ports of the liquid containers except one. This functionality is provided by the selection valve, which connects to all the outlets of the different liquid containers and combines the flow paths into one output. From there, the liquid flow is eventually guided into the microfluidic sample holder.

Originally, throughout this work, a commercial liquid chromatography selection valve¹³ was employed for this purpose. After a short time of usage, this selection valve was irreparably damaged by polymerized photoresist in between the rotor seals, causing the sealing surfaces to develop scratches. Hereby, the valve started to leak.

¹³ MXX778-605, IDEX Health & Science

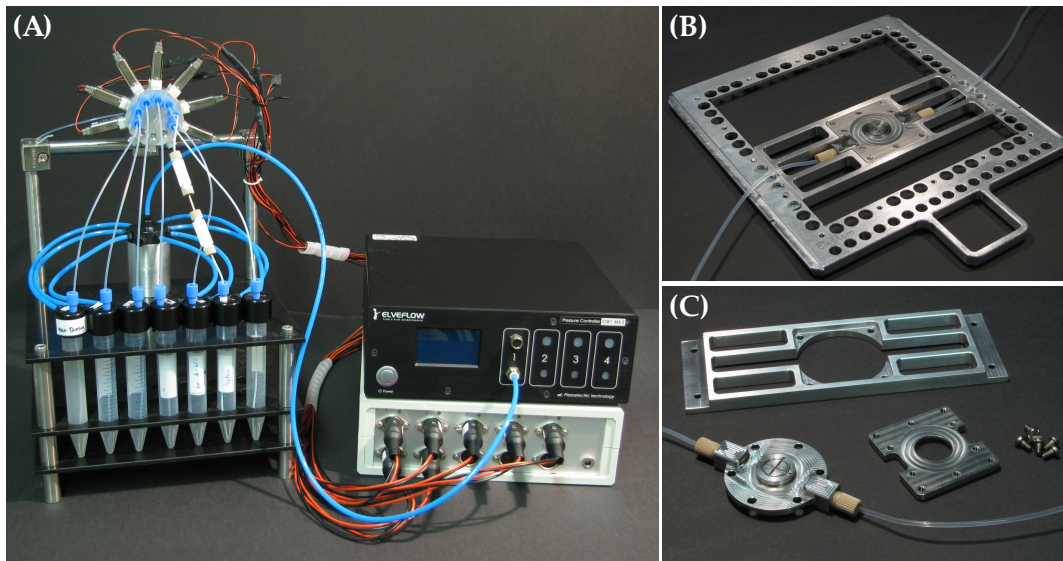


Figure 4.8: Photographs showing the experimental setup. **(A)** Overview of the injection system. On the left-hand side, the liquid containers connected to the star-shaped selection valve via thin microfluidic tubing are visible. On the right-hand side, the electronic pressure controller (black box) is shown, connected to the liquid containers via the nitrogen-carrying blue hoses. The gray box is for electronic control of the selection valve. **(B)** Photograph of the sample holder, with the microfluidic chamber in its center. **(C)** Opened microfluidic chamber. The part on the bottom left hosts the small round coverslip, into which structures are printed. Adapted from [73] (CC BY 4.0).

Hence, as a more robust approach, a star-shaped selection valve providing the very same functionality was built by attaching ten commercial solenoid valves¹⁴ onto a home-built aluminum 10-to-1 manifold, which additionally guides each input flow path through an individual solenoid valve. This assembly is displayed schematically in Figure 4.7. Photographs of the complete microfluidic system are displayed in Figure 4.8. Herein, the star-shaped selection valve which is connected to the different liquid containers is depicted in panel (A), while panels (B) and (C) show the microfluidic sample holder which has already been discussed in the previous section.

For controlling the valve assembly from the computer, a microcontroller board (Arduino Uno) is used. The home-built valve assembly has proven to be reliable so far and none of the solenoid valves has failed in the course of carrying out the experiments shown in this work.

¹⁴ LVM09R3Y1-5C-6-Q, SMC Corporation

4.2.5 Flow Considerations

The viscosity of the photoresists and the high resulting pumping pressures are a major concern for the layout of the microfluidic injection system. Another challenge arises from the high differences in viscosity between the photoresists and the solvents to be used. Hence, in this section, I will give a brief summary over the fluid dynamics in the microfluidic system.

For the flow resistance of the entire microfluidic system, the major contribution to this quantity is expected to stem from the microfluidic tubing connecting all the different fluidic components. Hence, in the following considerations, the flow resistance of the selection valve and the microfluidic chamber itself will be neglected. Instead, only the flow resistance stemming from the microfluidic tubing will be considered.

4.2.5.1 Validity of the Hagen-Poiseuille Equation

In microfluidic systems, liquid flow typically exhibits laminar flow characteristics. Hence, as described in section 2.3, it can be described by the Hagen-Poiseuille equation, which connects the flow rate dV/dt to the applied overpressure Δp . For a circular pipe with radius r and length l filled with a liquid of dynamic viscosity μ , it is given as

$$\Delta p = \frac{8\mu l}{\pi \cdot r^4} \frac{dV}{dt}. \quad (4.1)$$

The validity of this description holds true as long as the flow is laminar. This assumption can be tested by calculating the Reynolds number, which weighs inertial against viscous forces in the flow and is typically used as a figure of merit for testing if a flow is laminar.

For a circular pipe, the Reynolds number can be calculated from

$$\text{Re} = \frac{\rho \cdot v_m \cdot d}{\mu}, \quad (4.2)$$

where v_m denotes the average fluid velocity, d the pipe's inner diameter and μ the dynamic viscosity. For Reynolds numbers below a certain value Re_{crit} , viscous forces dominate and hence the flow is laminar. For Reynolds numbers above Re_{crit} , inertial forces become significant and hence the flow is typically turbulent. From experimental analysis of the transition from

Table 4.1: Reynolds numbers for a flow with $v_m = 5 \text{ cm s}^{-1}$ through microfluidic tubing with an inner diameter of 1 mm, calculated for different chemicals to be used in the microfluidic system. In all cases, the Reynolds numbers stay well below the critical Reynolds number $R_{\text{crit}} \approx 2320$.

Chemical	μ in Pa s	ρ in kg m^{-3}	Reynolds Number Re
Acetone	$0.38 \cdot 10^{-3}$	784	103
Isopropyl alcohol	$2.37 \cdot 10^{-3}$	786	17
PETA	1	1180	0.06

laminar to turbulent flow, the critical Reynolds number has been determined to assume a value of $Re_{\text{crit}} \approx 2320$ [41].

In the microfluidic injection system, microfluidic tubing with an inner diameter of $d = 1 \text{ mm}$ or smaller is to be employed. Hence, to estimate an upper bound of the Reynolds numbers to be expected, a rather high average flow velocity of 5 cm s^{-1} and an inner tubing diameter of $d = 1 \text{ mm}$ are assumed. Table 4.1 lists the resulting Reynolds numbers calculated for two exemplary solvents to be used, and for PETA, which is the basis for many photoresists for 3D laser microprinting. All resulting Reynolds numbers stay well below the critical Reynolds number $R_{\text{crit}} \approx 2320$ and hence the flow of all different chemicals can always be assumed to be laminar within the microfluidic tubing.

4.2.5.2 Swept Volume versus Required Pumping Pressure

Minimization of the swept volume of the whole system is of interest, as it determines the photoresist consumption per exchange step. The swept volume of the different parts of the microfluidic system realized in this thesis is illustrated in Figure 4.9. Herein, it immediately becomes clear that the dominant contribution stems from the microfluidic tubing. Hence, reducing the inner diameter as well as the length of the microfluidic tubing employed is important. However, according to Hagen-Poiseuille's equation, reducing the inner diameter d strongly increases the required pumping pressure proportional to d^4 . Hence, the chosen inner diameters result from a trade-off between swept volume and flow resistance. In contrast, reducing the lengths of the tubing is favorable in any case, since this reduces both swept volume and flow resistance. Thus, tubing lengths are generally chosen as short as possible.

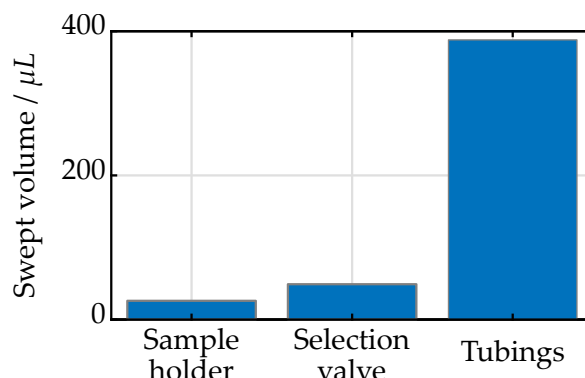


Figure 4.9: Swept volume of different components of the microfluidic system. The major contribution stems from the microfluidic tubing (length $l = 1$ m, diameter $d = 762 \mu\text{m}$.) The plotted swept volume for the tubing is for the flow path of a photoresist, and accounts for the tubing length from the liquid container to the sample holder. Fluidic components in the flow path after the microfluidic sample holder do not contribute to the swept volume, and hence their inner diameters are chosen bigger to not unnecessarily increase flow resistance. Due to the swept volume of the different parts, the photoresist consumption per injection step sums up to approximately 0.5 mL per injection step for the system realized in this thesis.

As a sideline, the internal volume of the microfluidic tubing connecting the output port of the microfluidic chamber to the waste container does not increase the swept volume of the system. Hence, for this part, there is no trade-off between swept volume and flow resistance. Consequently, large diameters of tubing should be deployed here, and the resulting flow resistance can be neglected.

In the experimental setup built throughout this thesis, the length of the microfluidic tubing from the liquid container to the microfluidic chamber sums up to 1 m, and an inner diameter of 0.76 mm is employed for the photoresists. This implies that if the entire flow path was filled with the rather viscous PETA ($\mu = 1 \text{ Pa s}$), a maximum pumping pressure $\Delta p = 2 \text{ bar}$ would lead to a volumetric flow rate of $\dot{V} = 100 \mu\text{L min}^{-1}$. The maximum pumping pressure is chosen for safety reasons (see section 4.2.3), and the calculation is carried out for PETA since it is the most viscous liquid to be used in the microfluidic system throughout this thesis. Since the summed-up swept volume of the entire system accounts to roughly 0.5 mL, it would take about 5 min for a full exchange of PETA with PETA. However, when

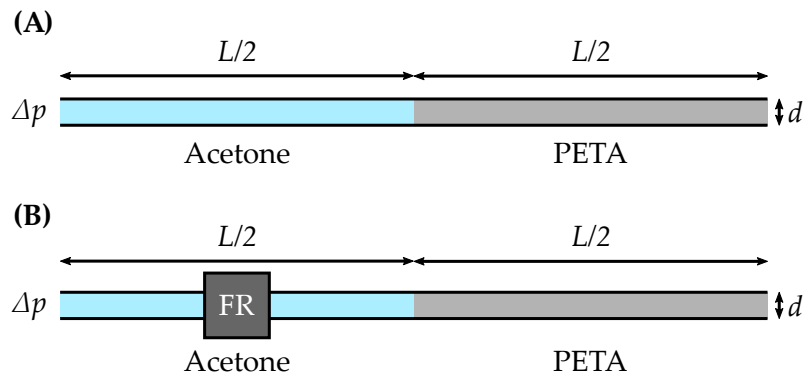


Figure 4.10: A flow resistor in the flow path of acetone is used to reduce differences in flow resistance during the exchange of viscous photoresist with low-viscosity acetone: Schematics of a microfluidic channel with diameter $d = 1$ mm and length $L = 1$ m. One half is filled with acetone, whereas the other half is filled with PETA. Acetone is injected into the channel from the left, and a pumping pressure of 1.5 bar is applied. **(A)** In the situation where no flow resistor is present, during injection of the acetone, the flow rate would shoot up by a factor of ≈ 1307 , rendering damage to the already printed structures likely. **(B)** On the contrary, if a flow resistor is installed into the flow path of acetone (capillary with inner diameter $65 \mu\text{m}$ and length 5 cm), the flow rate only increases moderately by a factor of 2.4 during the injection.

using the microfluidic system for photoresist exchange during printing, photoresists are typically exchanged with low-viscosity solvents, which reduces the times necessary for a single liquid exchange. As we will see later, an entire exchange step (including washing with organic solvents and injecting a new photoresists) will take less than 5 min for the structures to be printed in this work.

4.2.5.3 Implementation of a Flow Resistor

In a typical fabrication routine employing the microfluidic system, after having printed into one photoresist, it is necessary to replace the photoresist present in the system with an organic solvent for development. This situation is particularly problematic, since the flow resistance, due to the different viscosities of the liquids involved, changes dramatically during this exchange step. An example for such an exchange step is illustrated in Figure 4.10(A). Herein, a microfluidic channel with an inner diameter of

1 mm and a length of 1 m is filled with PETA in one half and with acetone in the other. This setting corresponds to the situation in the microfluidic system where the flow path between the selection valve and the microfluidic sample holder is filled with PETA, and acetone is injected by opening the corresponding input in the solenoid valve. Acetone is pumped by applying a pressure of 1.5 bar. The dynamic viscosities of the involved liquids differ by a factor of $\mu_{\text{PETA}}/\mu_{\text{Acetone}} = 2600$. Hence, following Hagen-Poiseuille's equation, during the exchange step, the flow rate would shoot up by a factor of $\mu_{\text{PETA}}/(2 \cdot \mu_{\text{Acetone}}) = 1300$ (i.e., if the entire channel was filled with PETA, the flow rate would even increase by $\mu_{\text{PETA}}/\mu_{\text{Acetone}} = 2600$). In an experiment, this would obviously not be acceptable, as the already printed microstructures would likely be damaged.

Obviously, this problem could be resolved by additionally introducing a flow sensor, combined with a fast control loop adjusting the pumping pressure continuously. However, in this work, a passive, more simple solution to this problem is employed: as depicted in Figure 4.10(B), a flow resistor is installed into the flow path of acetone. This part consists of a capillary (diameter $d = 65 \mu\text{m}$, length $L = 5 \text{ cm}$) and artificially increases the flow resistance in the acetone flow path. It is chosen such that the left half of the microfluidic channel depicted in (B) introduces a flow resistance on the same order as the right half. As a consequence, during pumping of the acetone at constant pressure, the flow rate only increases by a moderate factor of 2.4, which is acceptable for the experiments presented in the following sections.

4.3 FLUORESCENT SECURITY FEATURES AS BENCHMARK STRUCTURES

After having discussed the design principles and the detailed practical implementation of a microfluidic injection system for multi-material 3D laser microprinting in greater detail in the previous section 4.2, I will present the printing of benchmark structures in the following. In particular, 3D fluorescent security features similar to the ones discussed in chapter 3 are printed. However, due to the fully integrated fabrication procedure, it is easily possible to scale up the number of different fluorescent photoresists printed into one single structure. In addition, alignment between the single printing steps is vastly facilitated. Consequently, security features employing five different photoresists (using four fluorescent colors instead of two) are presented, printed at a four-fold density of markers per area.

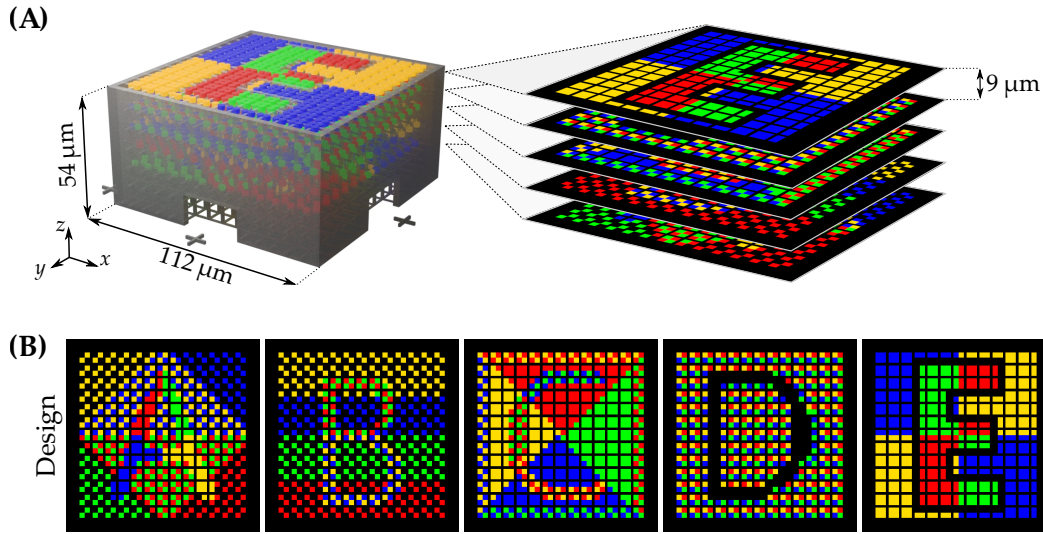


Figure 4.11: Design for the 3D fluorescent security features printed for demonstrating the capabilities of the microfluidic injection system. **(A)** Like in chapter 3, the structures consist of a non-fluorescent 3D cross-grid surrounded by walls as a support structure (depicted in gray). A three-dimensional arrangement of markers with four different colors of fluorescence are printed into the non-fluorescent grid in five different layers. **(B)** Test patterns of the different layers of fluorescent markers stored in the microstructure. Each layer features 26×26 possible marker locations. Adapted from [73] (CC BY 4.0).

4.3.1 Microstructure Layout

The layout for the benchmarking microstructures to be printed is depicted in Figure 4.11(A). Like the 3D security features presented in chapter 3, they are composed of a 3D nonfluorescent support grid surrounded by walls, with fluorescent markers printed into this support structure in five different layers. In particular, the support structures are identical to those from chapter 3: the lateral diameter of the rods in the 3D support grid is approximately $0.75 \mu\text{m}$, and the thickness of the walls is $5 \mu\text{m}$. Moreover, the walls feature holes for drainage of unpolymerized photoresist. The lattice constants are $a_x = a_y = 7.5 \mu\text{m}$ and $a_z = 9 \mu\text{m}$, respectively. The fluorescent test patterns to be printed into the support structures are depicted in Figure 4.11(B). In each layer, there are 26×26 marker positions at which markers can be printed into the support structure. Each of the markers has a lateral extent

of about 3 μm . As compared to the structure presented in chapter 3.4.2, the density of information that can be stored in the structure hereby increases from around 3.1 Gbit/cm³ to 18 Gbit/cm³. In total, the structure could store around 7.8 kbit of data.

For benchmarking the microfluidic system, these fluorescent security features are a particularly good choice for demonstrating the capabilities of the microfluidic injection system. Specifically, the fabrication of these structures requires the printing of many different photoresists into a single structure at relatively high resolution. In the printing steps, the capability of 3D laser microprinting to print through already polymerized material has to be exploited, which is not possible for many other 3D printing methods. Moreover, in between, unpolymerized photoresist has to be removed efficiently not only from the microfluidic chamber, but also from the *interior* of the already printed support structure. Finally, printing a structure employing materials with different fluorescence properties, laser scanning microscopy (LSM) can be employed for characterization. This enables the detailed analysis of the entirety of the 3D printed structure, and the structure can be checked for defects. In doing so, an incomplete exchange of photoresist in the fabrication would be visible in the printed structure due to missing parts or due to “wrong” fluorescence properties. However, as we will see, using the microfluidic injection system, reasonably clean structures can be obtained without the need for further processing steps.

4.3.2 Fabrication Routine

Conceptually, printing of the benchmarking microstructures is carried out in the same sequence as described in chapter 3. However, due to the microfluidic injection system, the sample does not leave the 3D printer during fabrication. Figure 4.12 visualizes the printing sequence of the different parts of the multi-material 3D benchmark microstructure. In particular, computer renderings, as well as in-situ optical microscope images are shown, recorded during printing using the 3D printer’s built-in camera. Herein, imaging is carried out through the same microscope objective that is also used for printing. For clarity, in these microscope images, the fluorescent parts of the microstructure have been overlaid with the corresponding colors of fluorescence. For all images, only the structure’s uppermost marker layer is visible, as indicated in the corresponding computer renderings.

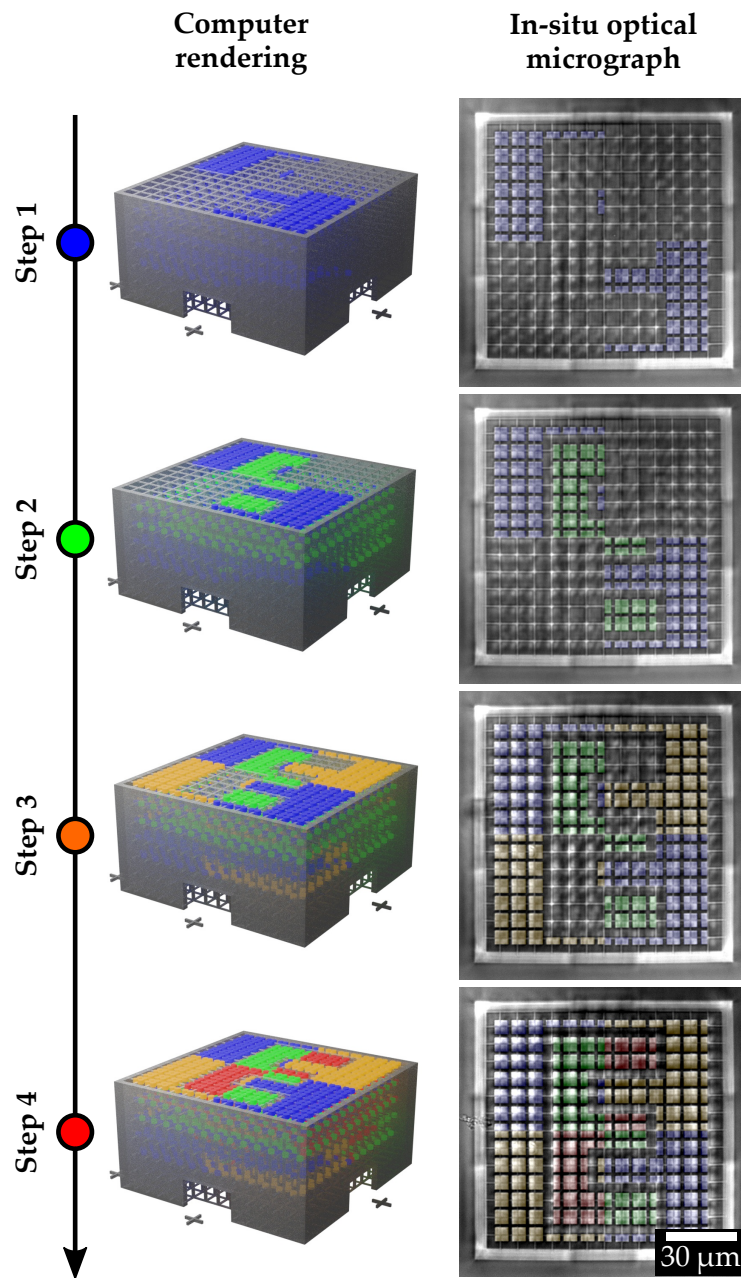


Figure 4.12: The test samples are printed in several consecutive steps from the different photoresists, exhibiting different fluorescence colors. Widefield optical microscope images, taken using the 3D printer's built-in camera, are depicted on the right-hand side. Corresponding computer renderings of the 3D structure are displayed on the left-hand side. For the optical microscopy images, only the sample's top layer is visible. Parts printed from fluorescent photoresists have been artificially overlaid with the corresponding color. Adapted from [73] (CC BY 4.0).

Table 4.2: Process parameters and injection routine for the different liquids during microstructure fabrication. The routine is repeated identically for all fluorescent photoresists. The numbers given are for the initial state where all tubings in the microfluidic system are “clean” and thus filled with air.

Liquid	Pressure p /mbar	Time t /s
PETA photoresist (#1)	2000	120
<i>0th Printing Step: Support Structure</i>		
Acetone	1500	60
mr-Dev 600	150	60
Fluorescent photoresist (#2)	500	45
<i>1st Printing Step: Fluorescent Markers</i>		
Acetone	1500	60
mr-Dev 600	150	60
Fluorescent photoresist (#3)	500	45
<i>2nd Printing Step: Fluorescent Markers</i>		
...		

In the fabrication routine, first, the microfluidic sample holder is prepared by inserting a substrate into it, which is glued by UV-curing a tiny droplet of photoresist.¹⁵ In particular, to improve adhesion of the printed structures to the substrate, a silanized substrate is used (see section A.2.5). The fully assembled sample holder is then inserted into the 3D printer and connected to the microfluidic system.

Subsequently, the first photoresist is injected into the sample holder and printing of the non-fluorescent support structure is started. For printing the support structure, typically, an exposure power of 34.5 mW and a writing velocity of 1.5 cm s^{-1} are used. A long-working-distance objective with a correction ring for the refractive index of the immersion medium is employed.¹⁶ After finishing the first printing step, unexposed photoresist is removed from the sample holder and thereby from the printed support structures by flushing with acetone and mr-Dev 600 (micro resist technology GmbH).

¹⁵ Nanoscribe IP-S

¹⁶ LD LCI Plan-Apochromat $63\times/1.2$ Imm Korr DIC, Carl Zeiss

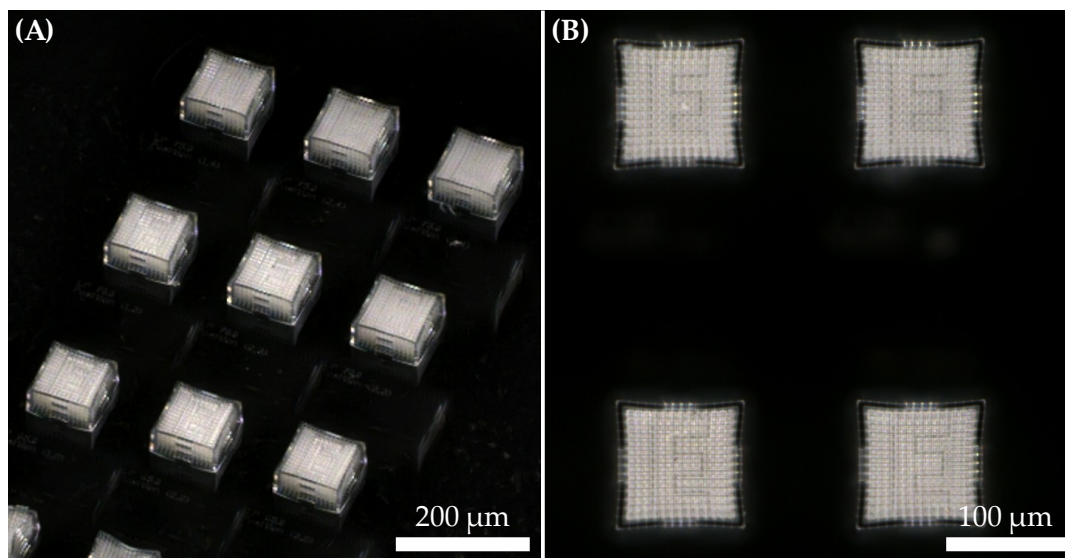


Figure 4.13: Optical microscopy images of a sample printed using the microfluidic system, captured using a digital microscope (Zeiss Smartzoom 5, reflection-mode ring illumination). (A) Oblique view of an array of security features printed from five different photoresists (extended depth of field image). (B) Top view of the printed structures. The uppermost marker layer is visible.

Hence, thereafter, the first fluorescent photoresist is injected and fluorescent markers are printed into the support structure. For printing the fluorescent markers, a scanning speed of 1 cm s^{-1} is used. The exposure power increases linearly from 34.5 mW for the topmost layer to 42.5 mW for the bottom layer.

These steps—flushing with acetone and mr-Dev 600, injecting fluorescent photoresists and printing markers—are then repeated until all different elements of the structure have been printed from the different fluorescent photoresists. The detailed injection sequence, as well as the pumping pressures and times are summarized in table 4.2. In particular, for washing away unexposed photoresist, both acetone as well as mr-Dev 600 are used, as this procedure efficiently washes away quantum dots sticking to the polymer surfaces of the printed structures, important for producing “clean” structures. After printing the last resist and flushing with the organic solvents, the microfluidic sample holder is taken out of the 3D printer, opened, and the sample is dried under a gentle flow of nitrogen. Widefield optical microscope images of a sample, as it is obtained after printing, are depicted

Table 4.3: Photoresists used for printing of multi-material benchmark structures. All photoresists additionally contain 2 % Irgacure 819 with respect to the monomer mass. More detailed photoresist recipes can be found in the appendix in section A.1.1. The fluorescent additives have been selected such that spectral overlap in their fluorescence emission is minimal, such spectral separation is possible for fluorescence microscopy.

	Color	Monomer	Fluorescent Additive
#1	—	100 % PETA	none
#2	Blue	50 % PETA, 50 % TDDDA	QDs, $\lambda_{em} = 450$ nm
#3	Green	50 % PETA, 50 % TDDDA	QDs, $\lambda_{em} = 525$ nm
#4	Yellow	50 % PETA, 50 % TDDDA	Atto 565 alkyne
#5	Red	50 % PETA, 50 % TDDDA	Atto 647N alkyne

in Figure 4.13. Herein, an array of multi-material test structures are shown. While panel (A) displays an oblique view of the sample, panel (B) shows a view from the top. Herein, the uppermost layer of markers is visible (i.e., the “E”).

The main components of the photoresists employed for the printing of the multi-material test structures are summarized in table 4.3. In regard to the fluorescent photoresists, two photoresists make use of colloidal quantum dots as fluorescent additives. The other two contain organic dyes, which are functionalized with an alkyne group. Thus, they can undergo a radical polymerization and can hereby be integrated into the polymer network. The detailed recipes for these photoresists can be found in the appendix in section A.1.1.

4.3.3 Fluorescence Microscopy on Fabricated Structures

In order to investigate the printed multi-material benchmark structures in detail, fluorescence laser scanning microscopy (LSM) is employed in analogy to chapter 3 (see section 3.4). Hereby, imaging of the full 3D structure is possible and thus the quality of the multi-material print can be examined.

A commercial LSM¹⁷ is employed for this purpose. For imaging, a droplet of immersion oil is applied on top of the printed structures and a 63×/1.4

¹⁷ LSM 510 Meta, Carl Zeiss

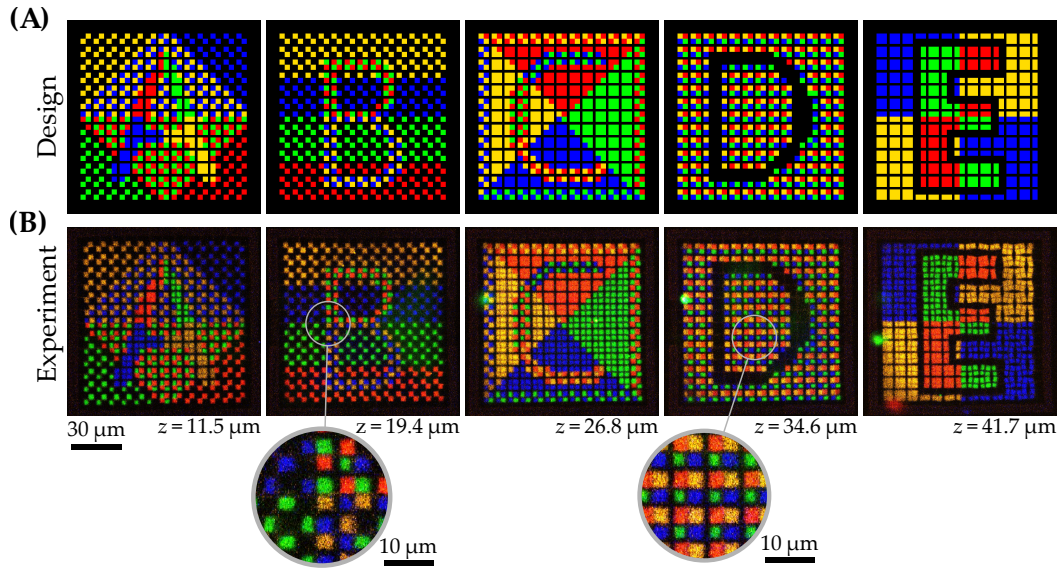


Figure 4.14: Images recorded by Fluorescence Laser Scanning Microscopy (LSM). **(A)** Computer design of fluorescent marker patterns printed in five different z -layers into the multi-material 3D fluorescent microstructure. **(B)** Recorded fluorescence images. The computer-test patterns are reproduced with high accuracy in the 3D printed multi-material structure. Insets show the high resolution at which many different photoresists (i.e., materials) can be reliably printed using the microfluidic injection system. Adapted from [73] (CC BY 4.0).

objective¹⁸ is used. Since this microscope features two independent detection channels with spectral filters and a photomultiplier tube, two different color channels can be recorded simultaneously. Hence, for recording four different fluorescence colors present in the printed structures, each z -section has to be scanned *twice* (with different filter settings in the detection beam paths for each scan) in order to record all fluorescence emission colors present in the three-dimensional microstructure. The experimental details can be found in the appendix (section A.2.2).

Fluorescence images recorded in this fashion are depicted in Figure 4.14. Herein, the computer-generated test patterns as depicted in panel (A) can be compared directly to the fluorescence images in (B). It is easily visible that the actual printed test patterns reproduce the computer-designed patterns in

¹⁸ Plan-Apochromat 63 \times /1.40, Carl Zeiss

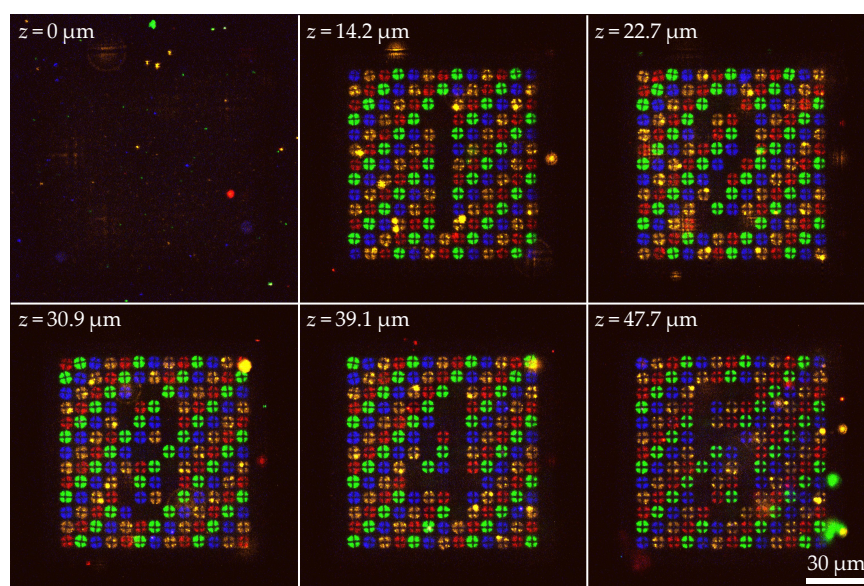


Figure 4.15: Fluorescence microscopy images recorded from another 3D multi-material test structure. This 3D fluorescent security feature incorporates fluorescent test patterns that are similar to those presented in chapter 3, however extended to four different fluorescent colors. In contrast to the sample shown in Figure 4.14, all photoresists contain colloidal quantum dots as fluorescent additives. Different image sections for different z values are shown, displaying the five different patterns of fluorescent markers printed into the microstructure, and the plane of the glass substrate located at $z = 0 \mu\text{m}$.

great detail. The insets in panel (B) display the resolution at which multiple different photoresist materials can be printed at using the microfluidic injection system: Here, up to five different photoresists are 3D printed on a micrometer scale into one single microstructure. In addition, using the microfluidic injection system, increasing the number of different photoresists is straightforward.

A different test sample, printed using the same printing sequence as used for the sample shown in Figure 4.14, is displayed in Figure 4.15. However, this sample features a more simple test pattern of fluorescent markers, similar to the test patterns presented in chapter 3. Since these patterns feature a four-fold lower density of markers than the one shown in Figure 4.14, these samples constitute a less challenging test structure. In this case, all of the fluorescent photoresists used in the fabrication of this structure contain

colloidal quantum dots as fluorescent additives in the different photoresists¹⁹. From the confocal fluorescence images shown, one can similarly deduce that also these structures are manufactured at high accuracy.

4.4 CONCLUSION

In this chapter, I have presented a custom-tailored microfluidic injection system that can be combined with 3D laser microprinting setups. Hereby, the fabrication of multi-material structures, composed of many different photoresist materials, is enabled. In particular, the microfluidic injection system is capable of injecting different chemicals, i.e., photoresists and organic solvents, into a tailor-made sample holder hosting a microfluidic chamber. 3D printing is carried out inside this microfluidic chamber, and therefore easy switching between different photoresists during 3D printing is possible. To the best of my knowledge, this setup represents the first experimental implementation of a fully integrated multi-material printer based on 3D laser microprinting with the capability of fabricating almost arbitrary multi-material 3D structures.

It is well conceivable that the concept presented here—or similar combinations of microfluidics with 3D laser microprinting—may become a common experimental method for the fabrication of three-dimensional multi-material microstructures. In the future, to make the concept more versatile, one important limitation should be addressed however: the microfluidic sample holder presented in this work inherently limits the build height of printed microstructures. This maximum build height is ultimately limited by the fixed working distance of the objective lens used for 3D printing. Hence, to circumvent this problem, future designs could for example feature microfluidic chambers with adaptive height.

¹⁹ Trilite Fluorescent Nanocrystals (Cytodiagnostics), with central emission wavelengths of $\lambda_1 = 450$ nm, $\lambda_2 = 525$ nm, $\lambda_3 = 575$ nm, and $\lambda_4 = 665$ nm. See section [A.1.1](#) for photoresist preparation.

Part II

COMBINING 3D PRINTING AND
SELF-ASSEMBLY

5 Chapter 5

3D LASER MICROPRINTING OF NANOPOROUS POLYMERS

Within the first part of this thesis, the realization of multi-material 3D microstructures was demonstrated by the sequential 3D printing of different photoresist into one single structure. In doing so, three-dimensional structuring of the printed object was only determined by the top-down approach of 3D printing. Owing to the great freedom of design and the increasingly fast speed at which almost arbitrary three-dimensional structures can be manufactured by these techniques, they have become increasingly popular over the last years [24, 95, 96]. However, 3D printing is usually limited to minimal printing resolutions in the regime of hundreds of nanometers [31], and is generally limited in fabrication speed [24].

In contrast, 3D structuring can also be introduced by the mechanism of self-assembly [97]. Here, interactions between disordered building blocks (for example, molecules) lead to the formation of ordered 2D films or 3D structures. Hence, complex 2D and 3D functional assemblies can be realized, which often exhibit a structuring on the nanoscale. Examples include 2D self-assembled monolayers, micelles, protein structures, as well as three-dimensional nanostructures [98–101]. In contrast to 3D printing, self-assembly inherently is a parallel process—and therefore, fabrication times do typically not increase drastically when processing larger areas or volumes. Conse-

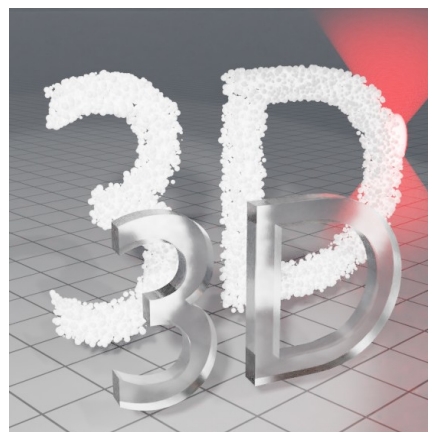


Figure 5.1: The photoresist presented in this chapter enables the printing of *porous* polymers, with pore sizes below 100 nm.

quently, due to this scalability, large quantities of such nanostructures can be realized in a short amount of time.

Consequently, combining the two approaches of self-assembly and 3D printing, and thereby combining the advantages of 3D printing with those of self-assembly, appears promising. Ideally, this would allow for the manufacturing of arbitrary three-dimensional hierarchical microstructures, with a 3D structuring on both the microscale (by 3D printing) as well as on the nanoscale (by self-assembly).

Along these lines, I will present a photoresist for 3D laser microprinting that allows for the 3D printing of inherently porous polymers in this chapter. In particular, the porosity of the material printed from the photoresist is achieved by a so-called polymerization-induced phase separation (PIPS). Thereby, the photoresist itself introduces a porosity on the scale of tens of nanometers, and arbitrary three-dimensional microstructures can be printed from it by 3D laser microprinting. Therefore, besides multi-material printing using multiple different photoresists, this method constitutes another approach for the printing of highly complex microstructures. As we will see, the porosity of the printed material can be tuned during printing—and in this sense, multiple materials can be printed from one single photoresist. Furthermore, this photoresist could also be printed in combination with the microfluidic injection system presented in the previous chapter. The hierarchical micro-/nanostructures obtained by printing this photoresist could not have been realized using other techniques: in particular, due to limited printing resolution, 3D printing the same structures from a conventional photoresist would have previously not been possible by the means of 3D laser microprinting.

For characterization of the printed material, scanning electron micrographs are recorded from ultramicrotome sections. Subsequently, for further characterization, image analysis is carried out on those images. In addition, the light-scattering properties of the material are investigated. It is found that the porosity (and thereby the light-scattering coefficient) of the printed material can be tuned during printing, such that porous as well as non-porous material can be printed from the same photoresist. Finally, as an application example, a 3D printed Ulbricht integrating sphere is demonstrated.

Unless indicated otherwise, all experiments in this chapter have been carried out by me, including photoresist development, process optimization and 3D printing of all microstructures presented. Notably, ultramicrotomy of samples and subsequent imaging by scanning electron microscopy was carried out by the group of Prof. Rasmus Schröder (Heidelberg University).

5.1 POROUS MATERIALS

Porous materials are ubiquitously found in nature, as well as in technological applications. In nature, prominent examples include porous stones, wood and bone. Owing to their multifaceted properties, there is also a wide range of applications in technology.

One important property of porous materials is their unusually large surface area. This property is commonly exploited in chemistry, for example as porous catalysts in reactions, for filtration techniques, or when using activated carbon for the adsorption of particles [102]. In batteries or fuel cells, porous separators and electrodes are employed, since they are permeable for liquids and allow ion transport throughout their volume.

In optics, porous polymers can exhibit strong light scattering due to the difference in refractive indices of the constituent materials. This property can for example be observed on eggshells or on paper. Hence, they can for example be used for the creation of materials with very high diffuse reflectivities, which are yet free from scattering particles such as titanium dioxide [103].

In mechanics, porous materials offer the ability to create lightweight yet mechanically strong architectures. Examples for this property can be found in nature (such as bone or wood), but also increasing research effort is put into such materials being created by additive manufacturing in terms of 3D printed microlattices [104, 105].

In this context, rendering 3D laser microprinting able to 3D print inherently porous materials appears like a promising avenue towards materials with interesting properties for chemical, biological, mechanical or optical applications. Furthermore, a range of volume material properties that are poorly attainable within a printable photoresist—like optical absorption or electrical conductivity—might be realizable by means of post-processing, where another material is deposited into the pores of the porous polymer.

5.2 PHOTORESIST DEVELOPMENT

In this section, I will give a short overview of methods that can in principle be used for the development of inherently porous 3D printing inks. Also, I will briefly review publications that report on research work into a similar direction. Subsequently, I will explain polymerization-induced phase separation (PIPS), which is the porogenic mechanism that I will use to develop

a printing ink for 3D laser microprinting. During 3D printing of this resist, spatial inhomogeneities resulting from oxygen concentration gradients in the photoresist droplet occur: I will therefore discuss strategies on how to cope with these difficulties. These strategies enable the fabrication of structures with a very homogeneous porosity throughout the volume.

5.2.1 Introduction

The manufacturing of porous polymers can be accomplished by a number of different techniques. Typically, when producing a porous polymer from a polymerization mixture, pores are introduced into the material during the reaction by so-called templates. Alternatively, templates can also be introduced into molten polymers. In particular, templates are chemically inert substances that occupy space in a liquid mixture which is then solidified, such that solidification of polymer cannot take place in the space occupied by the template. Hence, after the solidification (i.e., polymerization or freezing) is finished, polymer is only present at points in space that were not occupied by a template. Substances in gaseous, liquid or solid state can be used as templates, and often have to be removed from the then porous polymer using a solvent.

In terms of printing inks for 3D printing, first steps towards the printing of inherently porous materials have been made. In extrusion-based 3D printing, salt particles (i.e., solid templates) have been introduced into the 3D printing filament. After washing out the template from printed structures, a porous material remains, with pore sizes in the range of 20 to 70 μm , which is determined by the size of the salt particles [106]. Similarly, in the context of stereolithography, photopolymerizable resins loaded with salt particles have previously been published [107]. In stereolithography, porous materials have also already been printed from photoresists that form a high internal phase emulsion with a liquid porogen emulsified in the photoresist [108]. Emulsion- and foam-based inks (i.e., using liquid and gaseous templates) have also already been developed for 3D direct ink writing, from which porous ceramics can be obtained by sintering the 3D printed parts [109, 110]. Notably, porous 3D printed polymers with pore sizes on the scale of tens of micrometers have also been realized by adding foaming agents to the photoresist. Heating of the 3D printed parts then causes the foaming agent to degas, leading to an expansion of the material and due to pores generated throughout the material [111].

When discussing optical 3D printing methods, one problem persists for all template-based approaches: a photoresist developed along these lines is typically spatially inhomogeneous in the sense that particles or droplets are distributed in a monomer matrix. Since the refractive indices of the different phases of such a photoresist typically differ, light scattering occurs. With respect to 3D laser microprinting, pronounced light scattering would lead to a strong decrease of the quality of the writing focus, and hence to a decreased printing resolution and increased required laser powers. Hence, when following the approach of a template-based method for the development of a new photoresist, one would have to spend particular attention to index-matching the different phases of the photoresist. Strategies into this direction have also been deployed in the development of sol-gel based photoresists for the printing of glass structures [112].

In contrast to the previous discussion, when employing polymerization-induced phase separation, templates are *not* required for the manufacturing of porous polymers [113]. It is hence typically referred to as a “template-free” method.

With respect to porous polymers produced in the bulk by the means of polymerization-induced phase separation, typical applications include membranes and monolithic columns for filtration and separation techniques [113–116]. Furthermore, it has been employed for the realization of superhydrophobic surfaces, making use of the exceptionally large surface area due to a roughness on the micro- and nanoscale [117].

5.2.2 Polymerization-Induced Phase Separation (PIPS)

The underlying mechanism, polymerization-induced phase separation (PIPS) is illustrated schematically in Figure 5.2. In particular, the polymerization mixture (i.e., the photoresist) contains so-called porogens, and monomers. Porogens are substances, usually organic solvents, that are miscible with the monomer. Hence, this mixture is spatially homogeneous, and light-scattering is nonexistent in this state.

However, if a polymerization reaction is triggered in this mixture, polymer chains start to grow. In the case of 3D laser microprinting, this polymerization reaction is triggered via nonlinear excitation only in the focal region of the laser focus. As the polymer chains increasingly grow longer, at a certain point they become *immiscible* in the porogen, and hence, a phase separation

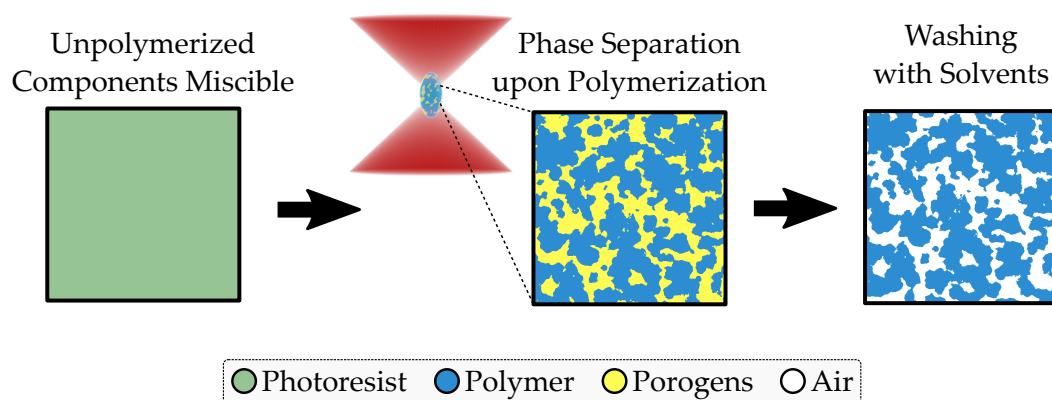


Figure 5.2: The photoresist contains monomers and porogens (i.e., organic solvents), which are miscible in the unpolymerized state. Polymerization is triggered optically by nonlinear excitation and subsequent radical generation in a laser focus. During polymerization, polymer chains start to grow, which then become immiscible with the porogens. Hereby, a phase separation occurs, and the polymer structure is “frozen” at a certain degree of polymerization. Subsequently, a porous polymer structure is obtained, with the pores being filled with a porogen-rich phase. By washing the polymerized structure with organic solvents, a porous polymer structure is obtained, with the pores being filled with air. Adapted from [118] (CC BY 4.0).

occurs and they start to agglomerate. This eventually results in a porous polymer, inside which the pores are filled with a polymer-lean phase (i.e., with porogen).

After the polymerization, i.e., after 3D printing has been finished, unpolymerized material is removed from the pores of the printed structures by washing with organic solvents. In particular, in this work, washing is carried out in acetone for 30 min. Supercritical drying of the printed structures is performed subsequently to reduce structural distortions or shrinkage during drying (see section A.2.4).

Two important properties to describe porous structures are the porosity Φ and the pore size distribution. In particular, the porosity is defined as the volume fraction of the pores in the porous structure. In polymerization-induced phase separation, for reactions in the bulk, this quantity is largely determined by the volume fraction of the porogen. In contrast, the choice of the porogen determines the grain size during polymerization, and therefore the mean pore size [113].

In more detail, for PIPS in the bulk, it has been found that porogens that are “poor” solvents (with respect to the monomer) lead to smaller particle sizes in the resulting polymer, and vice versa. This relation can be qualitatively explained as follows: after the polymerization has been initiated, polymer chains start to grow in the polymerization mixture, and hereby, the degree of polymerization increases with time. At a certain point in time, there is an onset in phase separation upon which the polymer chains precipitate. Hence, polymer particles start to grow larger and coalesce. This process is eventually halted as soon as a certain degree of polymerization is reached. Depending on the choice of the porogen, the onset of phase separation occurs at different times in the polymerization reaction: for “poor” solvents, phase separation occurs at earlier times, leading to bigger polymer particles. On the contrary, for “good” solvents, phase separation occurs at later times, leading to smaller particles [119, 120]. Since the porosity is determined by the volume of the porogen in the polymerization mixture, different particles sizes are directly correlated with different pore sizes. In addition, the obtained pore sizes have also been found to strongly depend on quantities like the surrounding temperature and the rate of polymerization [113].

In the field of stereolithography, photoresists that can be seen in analogy to the resist presented within this work have already been developed [121]. In these resists, during polymerization, a phase separation between growing polymer chains and glass precursor molecules occurs. After printing, structures are thermally sintered to obtain porous and non-porous glass structures. These photoresists are similar in the sense that they also make use of a polymerization-induced phase separation; however, they enable the printing of porous glass instead of porous polymer structures. Furthermore, in this work, 3D laser microprinting instead of stereolithography is employed, offering an improved spatial 3D printing resolution. Lastly, in-situ control of the porosity during 3D printing is demonstrated in this work, which to the best of my knowledge has not yet been achieved before.

5.2.3 A Photoresist Based on PIPS

The substances contained in the phase-separating resist presented in this work are depicted in Figure 5.3. In particular, we start from the very common monomer pentaerythritol triacrylate (PETA), combined with the common radical-generating photoinitiator Irgacure 819. These two substances have

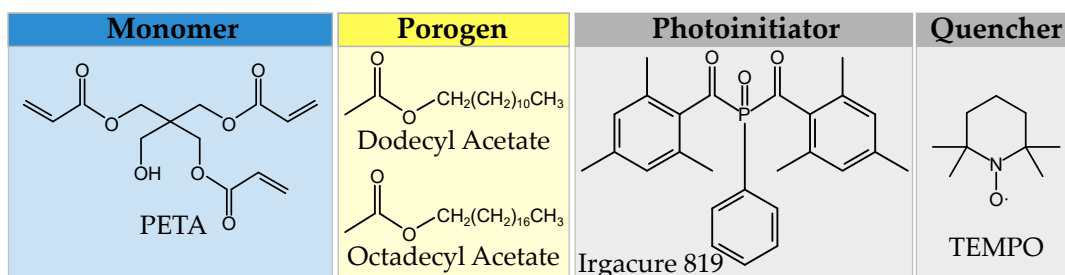


Figure 5.3: Composition of the phase-separating photoresist. For monomer and photoinitiator, the common substances pentaerythritol triacrylate (PETA) and Irgacure 819 are used, respectively. Dodecyl acetate and octadecyl acetate are contained as porogens. Additionally, 2,2,6,6-tetramethylpiperidinyloxy (TEMPO) is added as a radical quencher. Adapted from [118] (CC BY 4.0).

already been used in the photoresists presented in the previous chapters. However, in addition, dodecyl acetate and octadecyl acetate are added as porogens into the photoresist (mass fraction 22 % each). Lastly, 2,2,6,6-tetramethylpiperidinyloxy (TEMPO) is added as a radical quencher, which will be discussed in the following section. The detailed photoresist composition is listed in the appendix, section A.1.2.

Example structures printed from the phase-separating photoresist are depicted in Figure 5.4. Conventionally, the vast majority of photoresists for 3D laser microprinting yield 3D printed structures that exhibit a transparent, glass-like appearance. The nanoporous structures, however, exhibit a fundamentally different optical appearance: for illustration, panel (A) displays a reflection-mode oblique-view optical micrograph¹ of a cylinder (diameter $d = 350 \mu\text{m}$, height $h = 100 \mu\text{m}$) 3D printed from a common commercial photoresist (Nanoscribe IP-S) for 3D laser microprinting. In contrast, the same cylinder printed from the phase-separating photoresist exhibits a white appearance, which results from strong light-scattering within the volume of the nanoporous polymer. In order to show that arbitrary 3D structures can be fabricated from this resist, panel (B) depicts a nanoporous woodpile structure (rod spacing $30 \mu\text{m}$, beam width $15 \mu\text{m}$).

To gain further insights into the properties and the self-assembled nanostructure of the 3D printed material, panel (C) shows an overview electron micrograph of a printed flat cylinder, and a zoom-in into the same cylinder on the right-hand side. From these pictures, one can presume that the the

¹ Taken using a ZEISS Smartzoom 5 digital microscope and off-axis ring illumination

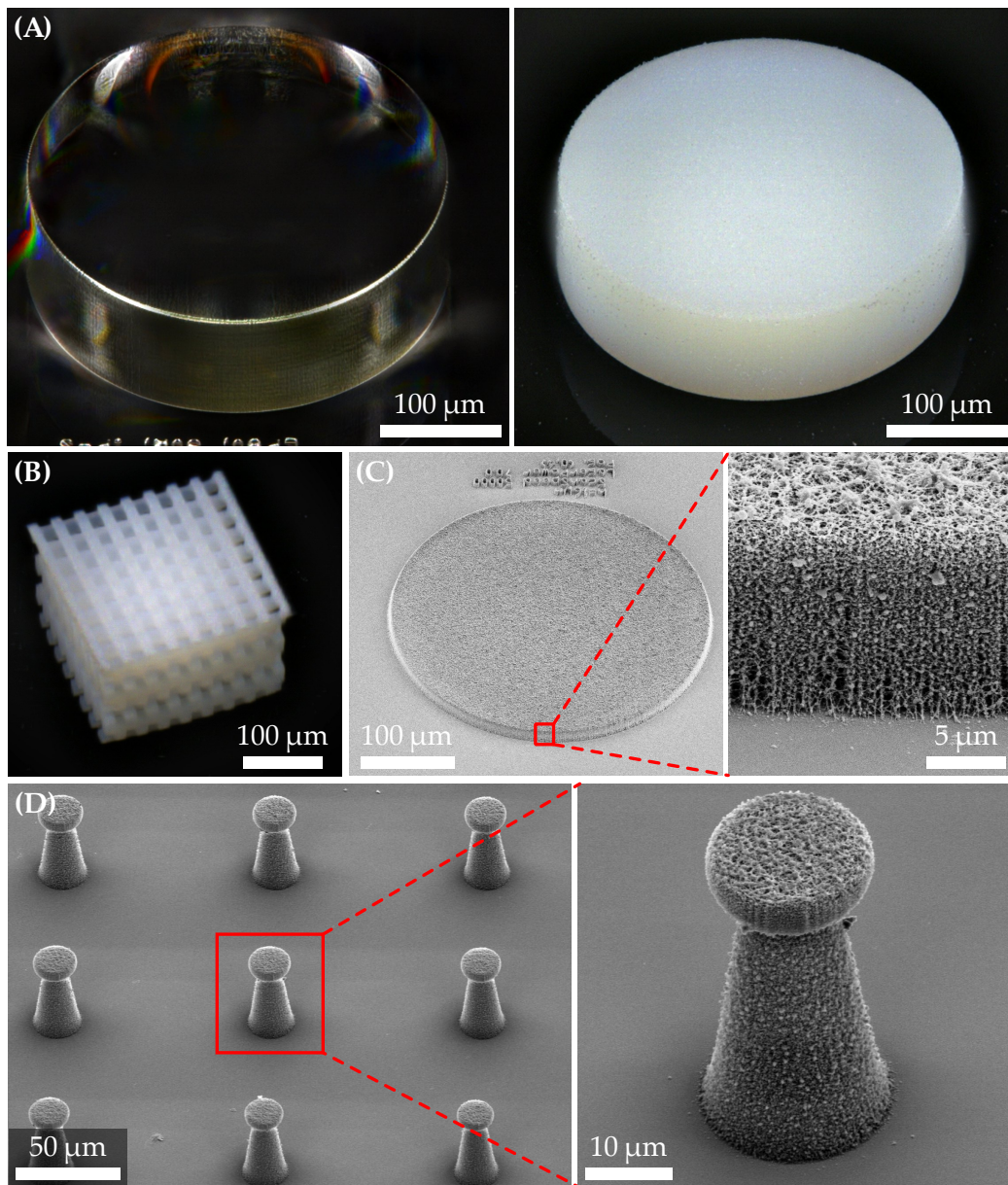


Figure 5.4: Nanoporous example structures printed from the phase-separating photoresist. (A) Cylinders (diameter $d = 350$ nm, height $h = 100$ μm) printed from a conventional (Nanoscribe IP-S, left-hand side) and from the phase-separating resist. Due to strong light-scattering, the nanoporous cylinder appears white, whereas the non-porous cylinder has a glass-like transparent appearance. (B) Nanoporous 3D woodpile structure. The rod spacing is 30 μm, and the width of the rods 15 μm. Panels (C) and (D) show scanning electron micrographs of a nanoporous cylinder ($h = 16$ μm) and an array of nanoporous pillars, respectively. These samples have been sputtered with 10 nm of gold for SEM imaging. Adapted from [118] (CC BY 4.0).

pore size at the surface of the material lies in the range of tens of nanometers. However, conventional scanning electron microscopy does not allow for the imaging of the *volume* of such structures. Hence, the volume of such a structure could potentially be non-porous, while exhibiting a rough or thin porous layer at the surface. Hence, in section 5.3, methods that enable the evaluation of the volume properties and that were employed in this work will be discussed. Panel (D) shows more electron micrographs of example structures 3D printed from the phase-separating resist. In particular, microstructures with feature sizes down to a couple of microns can be fabricated using the phase-separating resist.

However, as will be discussed in the next section, the so-called proximity effect is more prominent than in conventional photoresists—resulting in a slightly decreased spatial resolution as compared to conventional (for example, purely PETA-based) photoresists.

5.2.4 Oxygen Depletion During Printing

In the previous sections, I have described the porogenic mechanism and the photoresist composition that was used throughout this work. As it turned out, however, adopting a custom-tailored writing strategy is crucial to not only obtain structures with a porosity at the surface, but structures with a very *homogeneous* porosity throughout the entire *volume*, as well as reproducible results. Detailed investigations on this matter finally led to the adoption of a writing strategy where 1) the oxygen concentration is depleted in the photoresist droplet and 2) a radical quencher, TEMPO, is added to the photoresist to counteract the loss in resolution due to oxygen depletion.

Reproducibility Problems

Initially, structures were printed under ambient atmosphere. The photoresist was identical to the one described previously, except that it did not contain an additional quencher (i.e., no TEMPO). Under these writing conditions, strong reproducibility problems and inhomogeneous porosity were observed.

A sample for highlighting these problems is depicted in Figure 5.5(A). In particular, it shows a transmitted-light optical micrograph (view from top) of a series of nominally identical 3D cylinders² printed next to each

² Printing parameters for all cylinders: diameter $d = 350\ \mu\text{m}$, height $h = 100\ \mu\text{m}$, hatching

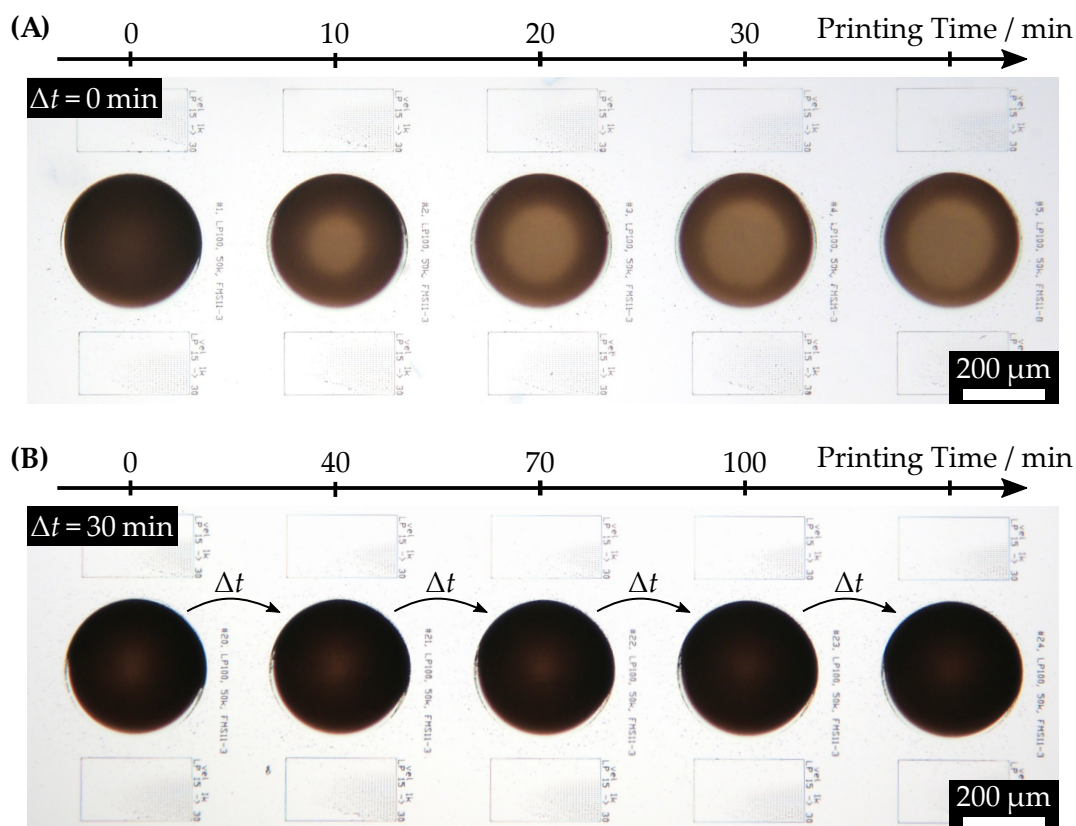


Figure 5.5: Sequences of nominally identical cylinders 3D printed under ambient atmosphere for testing the reproducibility of the porosity in one 3D printing job (view from top). The images are taken using transmission-mode optical microscopy. The brown color of the structures is linked to increased light-scattering and hence less transmission towards blue wavelengths. **(A)** Prominently, with progressing printing time, the central region of newly printed cylinders becomes increasingly transparent. This transparency is caused by reduced porosity and hence less light-scattering towards the center of the cylinders. In turn, the reduction in porosity is linked to a location-dependent depletion of the oxygen concentration in the photoresist during writing. **(B)** If printing is paused in between cylinders for a waiting time of $\Delta t = 30$ min, the oxygen concentration has sufficient time to equilibrate. Hence, the resulting 3D printed cylinders exhibit an identical but still spatially inhomogeneous appearance. The planar structures above and below the cylinders are for determination of the photoresist's threshold power before and after printing the individual cylinders, as will be discussed in Figure 5.6. The samples shown in panels (A) and (B) in this Figure correspond to the data presented in panels (D) and (C) of Figure 5.6.

other onto the same substrate. In these images, dark regions in the cylinders correspond to less light transmission, linked to strong light scattering due to a pronounced porosity. In turn, brighter regions in the cylinders transmit more light because of a lack in porosity. Two major aspects are to be observed: first, some cylinders look inhomogeneous in the sense that they exhibit a brighter region in their center, linked to a locally reduced porosity. Second, nominally identical cylinders printed at different times have a different appearance: while the first printed cylinder is homogeneously dark (i.e., porous), a bright region appears in the center of the following cylinders at later printing times.

Both of these problems could be traced back to a local depletion of oxygen in the photoresist: in particular, when printing the same testing sample, but introducing pauses of 30 min, cylinders with a reproducibly identical but still spatially inhomogeneous appearance could be printed, as depicted in Figure 5.6(B). Based on this finding, one can assume a process in the photoresist that is reversible by the means of diffusion, which is oxygen depletion and diffusion. Oxygen is known as a quencher for excited photoinitiator molecules [122] and as an inhibitor for radical polymerizations. The role of the complex interplay between oxygen depletion and reaction kinetics has been addressed in various works [35, 36, 39].

5.2.4.1 Spatial Polymerization Threshold Gradients

To further investigate this matter, the polymerization threshold value was determined by printing corresponding testing structures before and after each cylinder. Such tests are also visible above (before) and below (after) each cylinder in Figure 5.5. The polymerization threshold power is influenced strongly by the oxygen concentration in the photoresist [37]. Hence, if the oxygen-depleted region extends over a larger region around the printed cylinder, the difference in threshold power caused by the printing of such a cylinder may be measurable.

Results from such investigations are displayed in Figure 5.6. In particular, panel (A) shows a transmitted-light optical micrograph of the test-pattern. Here, the test structure for determination of the polymerization threshold power $P_{\text{th},1}$ is printed first (left-hand side). For this purpose, single lines are printed with increasing power of the writing laser in positive y -direction

distance $0.5\ \mu\text{m}$, slicing distance $1\ \mu\text{m}$, laser power $P = 50\ \text{mW}$, scanning velocity $v = 5\ \text{cm s}^{-1}$. Unless indicated otherwise, these parameters are used in all structures.

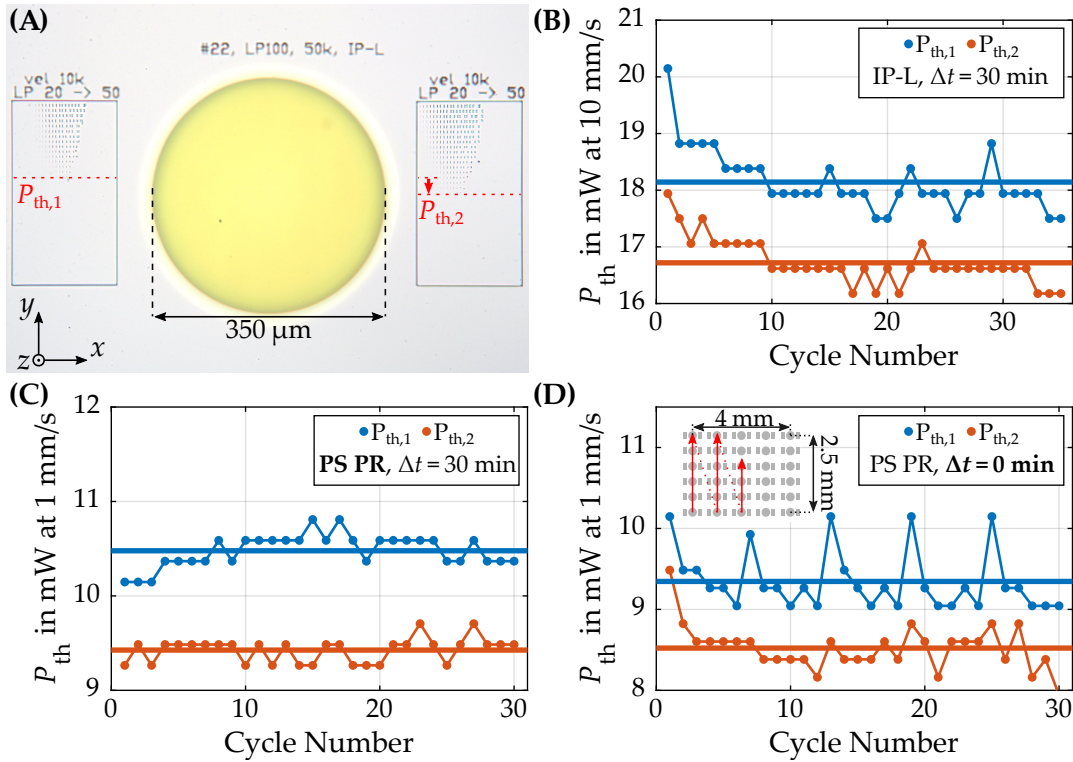


Figure 5.6: Measurements of polymerization threshold power before ($P_{th,1}$) and after ($P_{th,2}$) 3D printing a solid cylinder. Due to depletion of the local oxygen concentration during printing, lower polymerization threshold values are measured after printing a bigger volume than before. **(A)** Transmitted-light optical micrograph of test pattern that is printed repeatedly (photoresist: Nanoscribe IP-L). In each pattern, first, a test structure for determination of $P_{th,1}$ is printed. Subsequently, a solid cylinder ($d = 350 \mu\text{m}$, $h = 100 \mu\text{m}$) is printed, followed by a second test structure in close proximity for determination of $P_{th,2}$. **(B)** Threshold powers $P_{th,1}$ and $P_{th,2}$ plotted over the number of repetitions for the commercial photoresist Nanoscribe IP-L. A significant difference in threshold power is observed before and after printing the big cylinder. After waiting for $\Delta t = 30$ min for the system to equilibrate, the test is repeated to ensure consistency of this behavior. **(C)** Same, but for the phase-separating resist (PS PR, without TEMPO added). **(D)** Same as (C), but for $\Delta t = 0$ min. The writing order of the test patterns onto the glass substrate is indicated by the small sketch in the top left. The jumps in threshold power can be explained by large spatial gradients in oxygen concentration in the photoresist droplet as compared to (C) (due to $\Delta t = 0$ min). Maxima in $P_{th,1}$ occur when printing on a position that is comparatively far away from the previous position on the substrate. Printing parameters for all panels are the same as for the sample in Figure 5.5.

(and for different z positions at different x positions). Then, a bigger cylinder ($d = 350 \mu\text{m}$, $h = 100 \mu\text{m}$) is printed with the same printing parameters as described previously for the sample shown in Figure 5.5. Finally, a second threshold power test for determination of $P_{\text{th},2}$ is printed. Printing of one test pattern takes ≈ 10 min. This procedure is repeated for a number of times to ensure consistency of the observed behavior. In between each repetition, printing is paused for a time span of $\Delta t = 30$ min in order to allow diffusive processes in the photoresist to proceed (i.e., to let oxygen diffuse into depleted regions).

For comparison of the results, this test is carried out in an “ordinary” commercial photoresist as well as in the phase-separating photoresist. Panel (B) in Figure 5.6 displays the results obtained in the conventional photoresist (Nanoscribe IP-L). Notably, $P_{\text{th},1}$ is consistently smaller than $P_{\text{th},2}$. Following the interpretation that changes in the threshold value are predominantly linked to changes in the oxygen concentration, this implies that oxygen is not only depleted in the polymerized volume, but also in the *vicinity* of the printed structure, i.e., in a region of tens to hundreds of microns away from the structure.

Panel (C) displays the results obtained for the phase-separating photoresist, written under ambient atmosphere and without any additional quencher added (i.e., not containing TEMPO). Also in this case, a significant difference between $P_{\text{th},1}$ and $P_{\text{th},2}$ is observed reproducibly.

In Panel (D), behaviour of the phase-separating photoresist is depicted, for the case where the waiting step in between the printed test patterns (i.e., $\Delta t = 0$ min) is left out. In this case, pronounced peaks occur in $P_{\text{th},1}$. These peaks stem from the fact that due to $\Delta t = 0$ min, the oxygen concentration is not allowed to equilibrate throughout the resist, and hence, larger spatial gradients remain in the photoresist when printing the subsequent test pattern. The patterns are printed column-wise in an array of 5×6 patterns, as indicated in the small sketch in panel (D). Maxima in $P_{\text{th},1}$ occur when moving to the next column, i.e., when moving over a large distance of ≈ 2.5 mm, as opposed to moving only $500 \mu\text{m}$ when printing within one column. Hence, the peaks in $P_{\text{th},1}$ can be seen as a direct result from the spatial gradients in oxygen concentration in the photoresist.

In summary, these results can be seen as strong indications that both irreproducibilities as well as spatial porosity gradients observed in nanoporous structures (see Figure 5.5) may well stem from spatial differences in oxygen concentration. These differences build up during printing, and are overlaid by continuous in-diffusion of oxygen from the surrounding. Notably, the

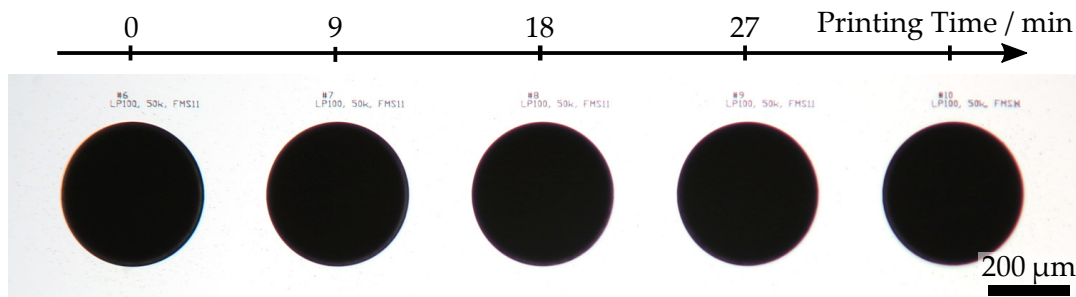


Figure 5.7: Transmitted-light micrograph of cylinders ($d = 350 \mu\text{m}$, $h = 100 \mu\text{m}$) printed under nitrogen atmosphere (i.e., under the absence of oxygen) and with the polymerization quencher TEMPO added to the photoresist. The appearance of these cylinders can be directly compared to those shown in Figure 5.5. In particular, they appear homogeneously dark, and reproducibly the same. This is an indication for homogeneous porosity throughout the volume, which will be examined in more detail in the later sections of this chapter.

results furthermore indicate that spatial gradients in oxygen concentration can also build up in conventional commercial photoresists (Nanoscribe IP-L). It is well conceivable that this in turn results in spatially slightly inhomogeneous material properties of printed structures also for such photoresists (for example, regarding the refractive index or the Young's modulus). However, the implications from this effect appear to be less severe and hence only of minor interest in this case.

5.2.4.2 Photoresist and Writing Strategy Modifications

In regard to the process that leads to the depletion of the oxygen concentration in a distance of tens of microns away from the polymerized material, one has to assume that this process is diffusion-dominated: in particular, following the reasoning from above, oxygen molecules from the surrounding diffuse into the direction of the exposed volume due to the concentration gradient. Hence, reducing the diffusion constant of the radical quencher could potentially help. Thus, another radical quencher, 2,2,6,6-tetramethylpiperidinyloxy (TEMPO), is introduced into the photoresist at a concentration of 0.07% (mass) with respect to the monomer. TEMPO is, just like oxygen, known to be an efficient radical quencher also in the context of 3D laser microprinting [37]. However, TEMPO is a substantially larger

molecule than oxygen and thus exhibits a smaller diffusion constant. In turn, oxygen was removed from the photoresist prior to printing by bubbling it with nitrogen gas for 5 min. Additionally, before starting the actual printing job, printing is started by writing a row of 5 to 10 cylinders in advance to further deplete residual oxygen in the photoresist droplet (printing parameters as before, exposure power 50 mW). Transmitted-light microscopy images of cylinders printed after these preparations have been met are depicted in Figure 5.7, that can be directly compared to those shown in Figure 5.5. Indeed, it turns out that these structures appear homogeneously dark, indicating a homogeneous porosity throughout their volume. Furthermore, the printed structures look reproducibly the same in these micrographs. Seemingly having found a promising method for printing homogeneously porous structures, these results are a starting point for more in-depth characterizations in the following chapters. As we will see, this method in fact yields structures with very homogeneous porosities throughout their volume.

5.3 METHODS FOR DETAILED MATERIAL CHARACTERIZATION

In this section, I will elaborate on the methods employed throughout this work for a detailed characterization of the volume properties of the 3D printed nanoporous polymer. Two distinct approaches are followed: on the one hand, scanning electron microscopy is combined with sectioning techniques. In particular, ultramicrotome sections are cut from the samples and imaged. This allows for the imaging of cuts through the porous structures. On the other hand, the structures are characterized by light-scattering experiments, i.e., by measuring the light-scattering coefficient μ_s , which is a *volume* property of the material, and hence can also give insights into the internal porosity.

5.3.1 Scanning Electron Microscopy

Scanning electron microscopy on sections prepared by ultramicrotomy was carried out in Prof. Rasmus Schröder's group (Heidelberg University). I prepared the porous polymer structures by 3D printing, and further preparation of the samples, ultramicrotomy and SEM imaging was carried out by Prof.

Rasmus Schröder's group.³ Subsequent image analysis for the extraction of porosity and pore size distributions was carried out by me.

5.3.1.1 Preparation of Sections by Ultramicrotomy

Ultramicrotomy is a common technique for the preparation of ultrathin sections, and is often used on biological samples. However, ultramicrotomy can be used in combination with a large variety of materials, including polymer samples [123]. In particular, it relies on mechanical cutting of the sample using a diamond knife. Commonly, the obtained sections are subsequently imaged by light or electron microscopy methods.

The preparation sequence that was carried out on the porous polymer structures is displayed in Figure 5.8. In particular, panel (A) shows the preparations prior to ultramicrotomy. The starting point is a glass substrate with the porous polymer structures printed onto it. This sample has been dried by supercritical drying (see section A.2.4), and hence, the pores of the porous polymer structures are filled with air. Next, the 3D printed porous polymer structures are taken off of the substrate. To facilitate this step, the glass substrate was not silanized prior to 3D printing (see section A.2.5). Thereafter, the polymer structures are stained by immersing them into a solution of 2% osmium tetroxide in acetone for 24 h. Hence, in this step, the nanoporous microstructures are wetted again—and the following steps are tailored such that the samples do not fall dry again, which could result in damaging the porous substructure. Consequently, the sample is embedded in Epon resin.⁴ In the procedure, first, the samples are infiltrated for 3 h with a mixture of 50% Epon in acetone. Finally, the samples are embedded into pure Epon. Hereby, also all the pores are filled with the resin, facilitating subsequent ultramicrotomy. Polymerization is carried out at 60 °C for 2 days.

Subsequently, the Epon blocks are trimmed, and ultrathin (thickness 80 nm) sections are cut using a diamond knife attached to a water-filled boat, as depicted in Figure 5.8(B). After cutting, sections float on the surface of the water in the cutting boat and can be captured and directly placed onto a silicon substrate. A intuitive and detailed explanation of a similar experimental technique can be found in [124].

³ People involved were Daniel Ryklin, Ronald Curticaen, Dr. Irene Wacker, and Prof. Rasmus Schröder.

⁴ Epon resin composition: 42.4 g glycid ether 100, 29.6 g 2-dodecenylsuccinic acid anhydride (DDSA), 18.4 g methyl nadic anhydride (MNA), and 2.4 g dimethylbenzylamine (BDMA).

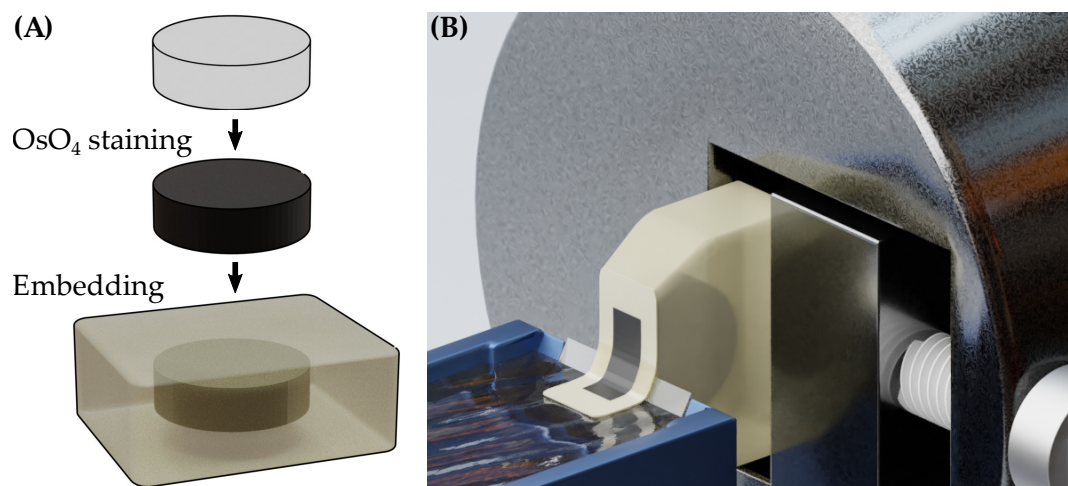


Figure 5.8: Preparation sequence of ultrathin sections cut from nanoporous structures. **(A)** The 3D printed nanoporous test structures are detached mechanically from the substrate. Subsequently, they are stained using osmium tetroxide in acetone solution. This improves contrast in later SEM imaging when detecting back-scattered electrons. The samples are then embedded into an epoxy resin. Thereby, all pores are filled with the resin as well. **(B)** Then, ultrathin (80 nm) sections are cut by the means of ultramicrotomy using a diamond knife attached to a water-filled boat. After cutting, the slices float on the water film and are subsequently placed onto a silicon substrate.

The result of this procedure are sections of the porous polymer samples, embedded into Epon resin. Importantly, also all the pores are filled with the Epon resin. Naturally, one would not expect large contrasts between those two material phases when using electron microscopy methods, since both Epon and the porous material are polymers [123]. However, the polymer of the porous material was previously stained with osmium tetroxide, and hence, there is adequate contrast in images taken by SEM, detecting the back-scattered electrons.

Finally, SEM images are recorded from the ultramicrotome sections. A primary electron energy of 1.5 keV is employed, using a field-emission scanning electron microscope (Ultra 55, Carl Zeiss). Electrons are detected using the ESB detector. Typically, in the images, pixel sizes between 3 and 20 nm are chosen.

5.3.1.2 Image Analysis

Besides the experimental techniques that allow for scanning electron microscopy of sections of the porous structures, image analysis routines are important for the extraction of different properties of the porous materials. Thereby, the quantification of these properties allows for a comparison between different samples. In this section, I will summarize the image analysis methods that are employed throughout this work for characterization of different 3D printed nanoporous microstructures. Similar routines have been used before in comparable contexts [125–127].

Two different quantities are extracted by image analysis. These are

1. the porosity Φ , which is defined as the volume filling fraction of the pores in a porous structure.
2. the distribution of pore sizes in the porous microstructure.

The image analysis routine is depicted in Figure 5.9. Panel (A) shows an exemplary raw SEM image recorded from an ultramicrotome section.⁵ Herein, regions in light grey correspond to the osmium-stained polymer of the nanoporous polymer structures. On the contrary, regions in dark gray correspond to the Epon-filled pores. Ideally, this image would contain only two different gray values, that can simply be matched to the two different phases visible in the image (i.e., polymer and pore/Epon). However, resulting from the finite (non-zero) penetration depth of the electron beam, regions with intermediate gray values correspond to polymer particles in the Epon matrix that lie close to the surface. Hence, these regions should be interpreted as pores in later steps.

Porosity

As a first step in image analysis, the SEM image is normalized, cropped, and global intensity gradients within the image are removed. Then, a median filter is applied to reduce pixel noise.⁶

⁵ In this context, it should be noted that throughout this work, for clarity, usually only sections of the entire SEM images are depicted. Image analysis is carried out for larger areas than shown.

⁶ All SEM images obtained on ultramicrotome sections and on which image analysis is carried out have a pixel size of 3 nm. Median filtering is performed using the `medfilt2()` MATLAB function within a 5×5 neighborhood.

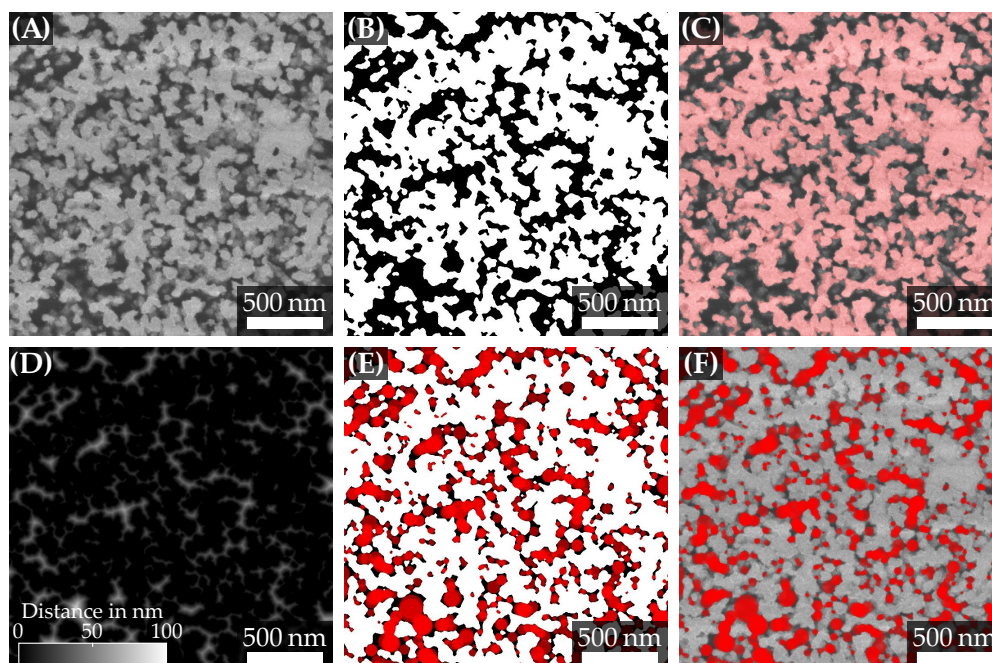


Figure 5.9: Image analysis routine for extraction of porosity and pore size distribution from electron micrographs recorded from ultramicrotome sections. (A) Raw image. Light gray corresponds to polymer, whereas dark gray corresponds to pores. Due to finite penetration depth of SEM imaging, gray values in between correspond to polymer below the surface of the EPON matrix of the ultramicrotome section. (B) Binarized image, calculated by setting a threshold via Otsu's method. The porosity is the fraction of black pixels. (C) Raw image, with an overlay of the binarized image from (B). (D) Euclidean distance map calculated from (B). (E) By searching positions and values of local maxima in (D), spheres can be fitted into the pores of the binarized image. (F) Same as (E), but with (A) as background. Adapted from [118] (CC BY 4.0).

Subsequently, image segmentation is carried out. For that purpose, an intensity threshold value I_{th} is calculated by applying Otsu's method [128] to the image shown in (A), and thresholding of the image using this threshold value is performed. The result of this procedure, a binarized image, is depicted in panel (B). In particular, we assume that the intensity values in the SEM image range between 0 and 1. The binary image is then generated by setting pixels with intensity $I < I_{th}$ to 0, and those with $I \geq I_{th}$ to 1. This means that in the binary image, pores are represented as black, and polymer as white regions.

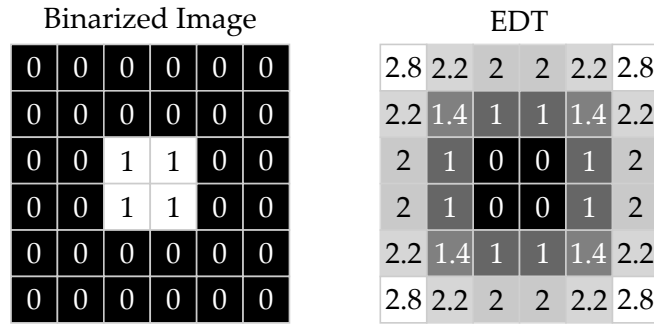


Figure 5.10: Euclidean distance transform (EDT). The EDT is calculated by, for each pixel, computing the euclidean distance to the next white pixel in the binarized image.

From the binarized image in (B), the porosity Φ can then be obtained via

$$\Phi = 1 - \frac{\sum_{i=1}^N I_i}{N} \quad (5.1)$$

where $I_i \in \{0, 1\}$ is the intensity value of pixel i in the binarized image. N is the total number of pixels in the binarized image.

As an intuitive representation, panel (C) shows the binarized image in light red, overlaid onto the raw SEM image from (A). Note that regions with an intermediate gray value in the raw SEM image are *not* overlaid with the reddish color, and are hence interpreted as pores. This behavior is consistent with the interpretation that those regions correspond to particles that are below the surface of the Epon matrix. However, it should be noted that shifts in the threshold value I_{th} directly affect the extracted porosity (and later also the pore size distribution), and hence, a good image segmentation is of importance for later processing steps. A detailed examination on the systematic error of different thresholding approaches (for the very 3D printed nanoporous polymer samples presented in this work) can be found in [129].

Pore Size Distribution

The further processing steps aim towards the extraction of a pore size distribution: subsequently, the euclidean distance transform (EDT) of the binarized image in panel (B) is calculated. The result is depicted in (D). In particular, the value of each pixel in the EDT is determined by the euclidean distance to the next white pixel in the binarized image. An illustrated

explanation of the EDT is also depicted in Figure 5.10. By computing the positions and values of local maxima of the EDT in Figure 5.9(D), circles can be fitted into the pores: in particular, the binarized image with an overlay of such circles is shown in panel (E), and the original SEM image with an overlay of the same circles in panel (F).

Finally, by binning the diameters of the circles from above, the pore size distribution is extracted. In particular, the pore size distribution extracted from the example in Figure 5.9 is shown in Figure 5.11(A). In more detail, it should be noted that the pore size distribution obtained by this procedure is to be taken with caution for a number of reasons:

1. First, this method would only yield ideal results for a porous structure inside which the pores have a spherical shape as well.
2. Second, the analysis is carried out on two-dimensional images only throughout this work. Due to stereological reasons, this results into a systematic error of the extracted pore size distributions. This issue does not affect the extracted porosity. Ideally, one could perform this analysis on three-dimensional image stacks with an isotropic pixel resolution. SEM imaging combined with ultramicrotomy can provide for three-dimensional image stacks; however, not with an axial resolution as good as the lateral resolution (the axial resolution is determined by the thickness of the ultramicrotome sections, i.e., 80 nm in our case).
3. Lastly, longer ridges in the EDT can result in local maxima occur at a high density along the ridge, such that circles fitted into the porous structure overlap. In some works, this issue was treated by setting a minimum distance between adjacent circles, and filtering the result accordingly [127]. This procedure had a negligible effect onto the extracted pore size distribution for the samples examined in this work (not shown). Hence, such filtering is not carried out.

Despite these points, the method presented above is a viable tool for the extraction of pore size distributions, and can be used to compare pore sizes in different polymer samples.

5.3.2 *Optical Characterization via Ballistic Transmission*

As already discussed in section 5.2.3, the 3D printed nanoporous material exhibits strong light-scattering due to the index mismatch between the

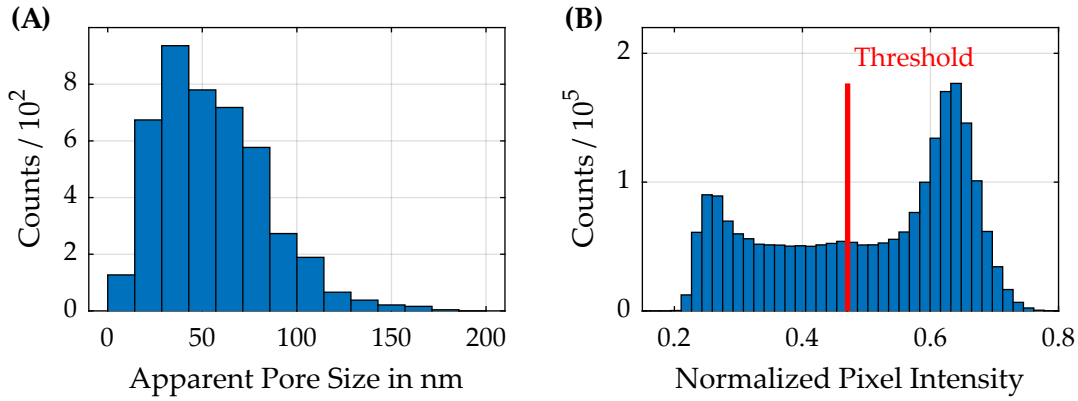


Figure 5.11: **(A)** Number distribution of apparent pore sizes extracted from the 2D image shown in Figure 5.9, but for a larger field of view. **(B)** Pixel intensity histogram extracted from Figure 5.9(A). The two peaks correspond to the two phases, i.e., osmium-stained polymer and pores/Epon. The threshold for binarization of the image obtained by Otsu’s method is indicated. Adapted from [118] (CC BY 4.0).

polymer material (refractive index $n \approx 1.5$) and the pores, which are filled with air (i.e., $n = 1$). This property has already been demonstrated in Figure 5.4(A), and leads to a white appearance and hence a high diffuse reflectivity due to pronounced back-scattering of light from the volume of the material. Besides the electron microscopy methods described in detail in the previous sections, the experimental determination of the light-scattering properties hereby offers an alternative venue for the characterization of volume properties. This section will hence introduce the reader into the experimental details. All of such measurements shown were performed by me.

In the following, we will assume a beam of light with an initial intensity I_0 that travels through a turbid (i.e., light-scattering) medium in z -direction. Along its path, light can be scattered away from the beam, such that the beam’s intensity decreases. Furthermore, absorption of light may occur. The decay in intensity after a certain distance z can be described by Beer-Lambert’s law

$$I(z) = I_0 \exp \left(- \int_0^z \mu_{\text{ex}}(z') dz' \right). \quad (5.2)$$

Here, $\mu_{\text{ex}}(z)$ denotes the so-called extinction coefficient that includes the

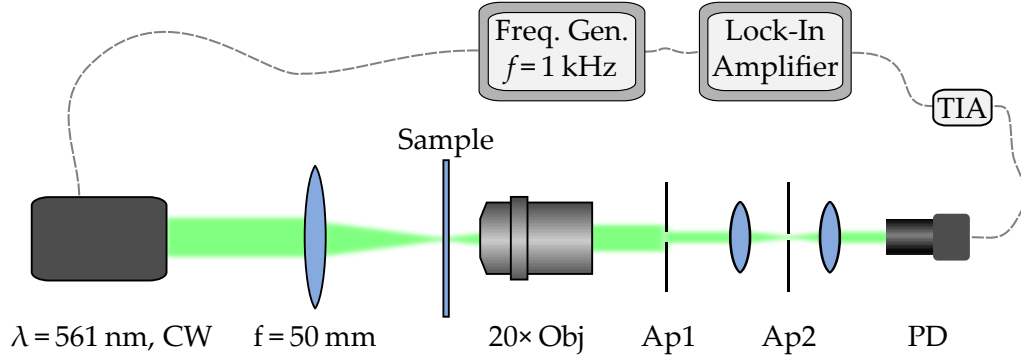


Figure 5.12: Setup for measuring the ballistic transmission through the nanoporous structures. A laser beam is focused onto the sample, and the transmitted light is measured using a silicon photodiode PD. In particular, the signal is restricted to small lateral values of the wave vector \vec{k} using an aperture Ap1, such that only *ballistically* transmitted light is measured. Another aperture in a conjugated image plane Ap2 is for further spatial filtering in the sample plane. The laser is modulated electronically at a frequency of $f = 1 \text{ kHz}$, and the signal from the photodiode is measured using a lock-in amplifier (via a transimpedance amplifier).

contributions from light-scattering and from absorption via

$$\mu_{\text{ex}} = \mu_{\text{s}} + \mu_{\text{a}}, \quad [\mu_{\text{ex}}] = \mu\text{m}^{-1}. \quad (5.3)$$

The quantities μ_{s} and μ_{a} denote the light-scattering and the absorption coefficient, respectively. In the following, the portion of light $I(z)$ that has not been scattered away from the initial propagation direction and that has not been absorbed will also be referred to as ballistically transmitted light.

In the following, we will neglect the absorption coefficient, $\mu_{\text{a}} = 0 \mu\text{m}^{-1}$, since both monomer (PETA) as well as photoinitiator (Irgacure 819) contained in the nanoporous polymer structures do not exhibit significant absorption in the visible range. Absorption of the photoinitiator only becomes significant below a wavelength of $\approx 450 \text{ nm}$. If we furthermore assume the light-scattering coefficient to be spatially homogeneous, Beer-Lambert's law simplifies to

$$I(z) = I_0 \exp(-\mu_{\text{s}} \cdot z). \quad (5.4)$$

Hence, in this case, the light-scattering coefficient can be determined by measuring the relative intensity $I(z)/I_0$ of the ballistically transmitted light

through a medium with thickness z :

$$\mu_s = -\frac{1}{z} \ln \left(\frac{I(z)}{I_0} \right). \quad (5.5)$$

The experimental setup for measuring the ballistically transmitted intensity of light through the 3D printed nanoporous polymer samples is illustrated schematically in Figure 5.12. Transmission measurements are carried out on sweeps of nanoporous cylinders (diameter 350 μm) with different heights, 3D printed onto a glass substrate. As light source, a continuous-wave laser light source emitting at a wavelength of 561 nm is used. Light is focused onto the individual nanoporous cylinders on the glass substrate, and the transmitted light is eventually detected using a silicon photodiode. In the detection beampath, an aperture Ap1 restricts detected light to small lateral values of the wave vector \vec{k} . Furthermore, spatial filtering is carried out by another aperture Ap2 in a conjugated image plane. This spatial filtering serves for suppression of stray light, such that only light transmitted through the 3D printed nanoporous polymer samples is detected. Furthermore, for reduced noise and for suppressing external light, the laser is electronically modulated at $f = 1$ kHz and a lock-in amplifier is used for measurement.

5.4 MATERIAL CHARACTERIZATION

In the previous sections, I have introduced the photoresist, as well as the underlying mechanism that leads to a porosity within the material 3D printed from this resist. In more detail, I have elaborated on the writing strategy that is employed in combination with this photoresist. Furthermore, I have introduced the methods that are used to characterize the 3D printed nanoporous material. In this section, I will subsequently present a more detailed characterization of the material, which is based on scanning electron microscopy images recorded on ultramicrotome sections, as well as on optical measurements of the ballistic transmission. Within this characterization, I will demonstrate that porous as well as non-porous material can be 3D printed from the same photoresist. This is achieved by carefully controlling the printing parameters—enabling multi-material printing from one single photoresist.

5.4.1 Characterization of Single-Exposed Structures

For examination of the porous material's properties in dependence of the exposure dose, test structures are printed using different exposure power levels P , of the writing laser. The scanning speed $v = 5 \text{ cm s}^{-1}$ is kept constant for all structures. The other printing parameters are the same as before (see A.2.3). Subsequently, SEM imaging on ultramicrotome sections prepared from these test structures is carried out according to the routine described in section 5.3.1.1.

Figure 5.13 displays SEM images taken on such ultramicrotome sections. The power of the writing laser P and the porosity Φ (extracted according to the routine from section 5.3.1.2) are indicated in the images. Notably, with increasing P , a decrease in porosity is observed. As a consequence thereof, also the pore size distribution extracted from those images (bottom row) shifts to smaller values. This is a promising result, since it potentially could enable in-situ tuning of the porosity during printing—effectively enabling the printing of *multiple* different materials with different volume porosity from *one single* photoresist.

In particular, the observed decrease in porosity from 43 % (vol) to 22 % (vol) is not to be expected for PIPS in the bulk, where large volumes are polymerized at once. Naively, as explained in section 5.2.2, in this case, one expects the porosity to be defined by the volume fraction of porogen in the photoresist. Hence, since this quantity is $\Phi_{\text{Porogen}} = 54 \text{ \% (vol)}$ for the photoresist presented in this work, also a similar porosity was to be expected. In case of phase-separating photoresists for stereolithography, this has consistently been observed: here, changing the exposure intensity leads to varying pore sizes at constant porosity, which is consistent with PIPS in the bulk [121].

With respect to 3D laser microprinting, a probable cause for the observation of porosities $\Phi < \Phi_{\text{Porogen}}$ is that in this case, polymerization is only triggered in small, spatially confined volumes simultaneously (i.e., voxels). Subsequently, one has to assume that $\Phi < \Phi_{\text{Porogen}}$ is enabled by monomer diffusion into the volume of the printed voxel and subsequent polymerization. In more detail, each layer of the structure shown above is printed by a set of parallel lines spaced by a lateral hatching distance of $0.5 \mu\text{m}$ (unidirectional scanning). These layers are furthermore spaced in z -direction by a slicing distance of $1 \mu\text{m}$. In particular, when doing so, there is an overlap between the individual exposures of the lines written. Hence, when printing a line, a post-polymerization may occur in neighboring lines. Consequently,

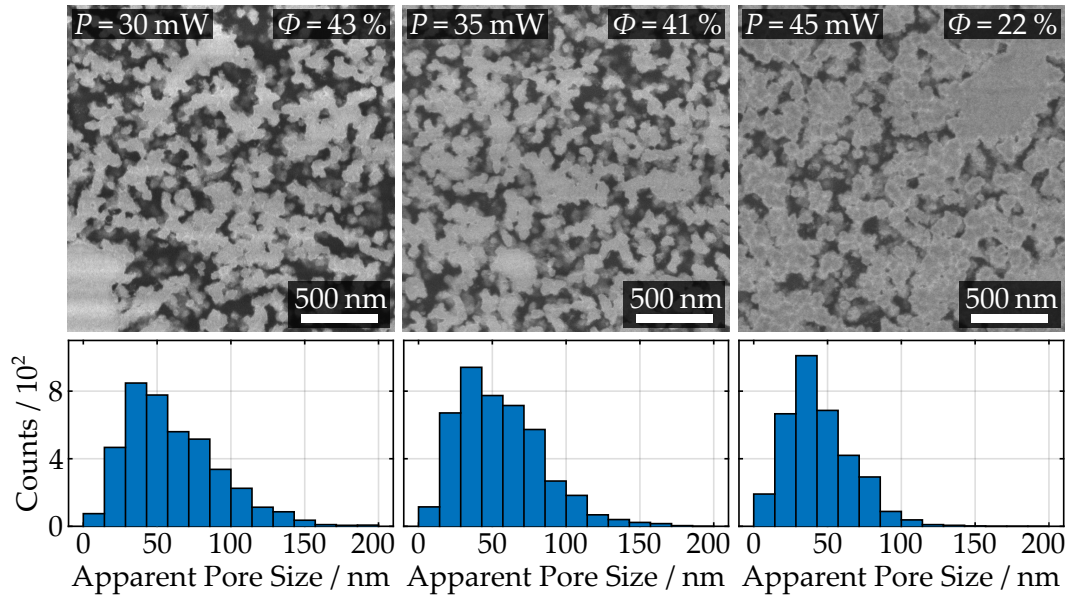


Figure 5.13: Nanoporous polymer 3D printed with varying exposure power P . Top row: Scanning electron micrographs recorded from ultramicrotome sections. Regions in light gray correspond to polymer, and dark regions to pores. With increasing exposure power, the porosity decreases. Bottom row: distributions of apparent pore sizes, corresponding to the SEM images above. With increasing exposure power, the center of the pore size distribution shifts to smaller values. Adapted from [118] (CC BY 4.0).

this means that the relevant timescale for diffusion to occur is defined by the time required for scanning one line, $\Delta t_{\text{line}} \approx 10$ ms, or alternatively by the time required for printing one z-layer of the structure, $\Delta t_{\text{layer}} = 3.5$ s. Within this explanation, the diffusion length $l_D = \sqrt{D \cdot \Delta t}$ would then have to lie on the same order as the hatching or the slicing distance, respectively. Here, D defines the diffusion coefficient for monomer in the porous material.

In summary, the printed material's porosity can be tuned by a factor of approximately 2 by adjusting the exposure power accordingly. However, having control over a wider range of porosity values would be desirable, which can be achieved by a clever printing strategy, as we will see in the following section.

5.4.2 Characterization of Double-Exposed Structures

Within the explanation for the tuning of the porosity Φ discussed in the last section, it should be possible to decrease the porosity even further. One approach for doing so would be to increase the exposure dose deposited per volume in the photoresist further, while letting the monomer sufficient time for diffusion. However, the experimentally available laser power is limited and increasing it further therefore not possible.

Along these lines, instead, a double-exposure strategy is employed for printing further test structures. Experimental results obtained on such structures are depicted in Figure 5.14. As an example, a block (with dimensions $250 \times 250 \times 50 \mu\text{m}^3$) is shown in panel (A), where only one half is written by the double-exposure strategy: in particular, each layer of the structure is first exposed with an exposure power P_1 , followed by an exposure with laser power P_2 . For the second exposure, the hatching direction is rotated by 90° . The other half is written by conventional single-exposure, as employed in the last section. On the right-hand side of panel (A), an oblique-view optical reflection-mode microscope image of a block manufactured in this fashion is depicted.⁷ Strikingly, in this optical image, one can immediately see that the double-exposed half of the block has a darker, transparent appearance. Intuitively, this appearance would be expected for the case of small porosity in the volume. In contrast, due to pronounced light-scattering, the left half still appears white (i.e., is porous in the volume). However, notably, the structure still features a thin white (i.e., porous) layer on top, even on the double-exposed part.

It is worth noting that it was also possible to obtain optically transparent structures by decreasing the scanning speed considerably while keeping the exposure power on a similar level (not shown). For the case of two-photon absorption, decreasing the scanning speed by a factor of 4 (i.e., to 1.25 cm s^{-1}) at constant laser power leads to a two-fold deposited exposure dose per volume. However, this is not an attractive option, as a double exposure printing strategy equally doubles the exposure dose per volume, but only increases the required printing time by a factor of 2.

As the optical inspection of the double-exposed structures shown in panel (A) looks promising, further characterization of such structures is

⁷ Image obtained using a digital microscope (Zeiss Smartzoom 5), with reflection-mode ring-illumination and the extended-depth-of-view functionality.

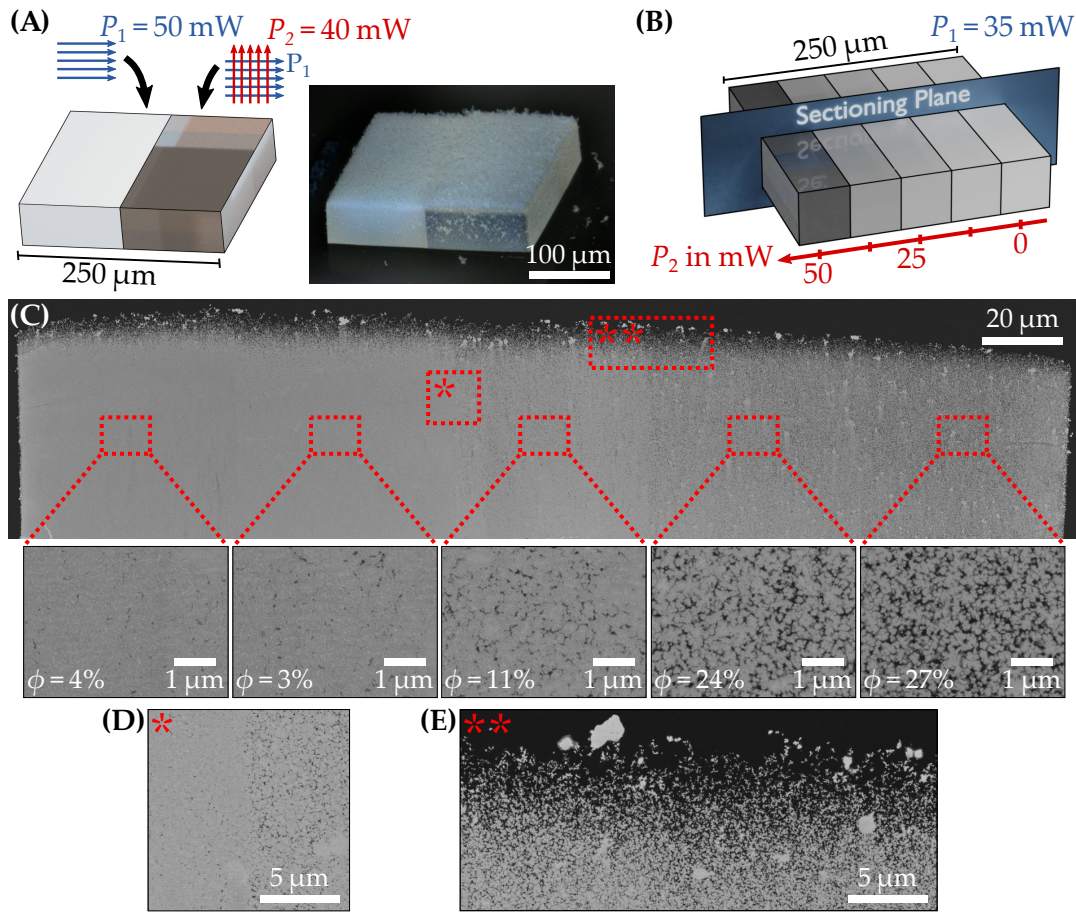


Figure 5.14: A double-exposure printing scheme allows for in-situ tuning of the porosity during printing. Hereby, materials with different porosities can be printed into structures within one single fabrication step. Here, each layer of the structure to be printed is exposed *twice* (with exposure powers P_1 and P_2 , respectively.) (A) Solid block where the left half is exposed once, whereas the other half is exposed twice. For the second exposure, the hatching direction is rotated by 90° as indicated. Due to reduced porosity in the right half, the material appears transparent. (B) For more detailed investigation, the second exposure power is tuned throughout a test structure as indicated. The sectioning plane for ultramicrotomy is indicated. (C) Scanning electron micrographs obtained on a ultramicrotome section from the structure shown in (B). From right to left, the exposure power P_2 is increased. Hereby, the porosity decreases, which enables *in-situ control* of the porosity of the printed material. (D) Transition between two regions with different P_2 . A sudden change in porosity is observed. The transition is remarkably sharp. (E) All printed structures feature a region with increased porosity on top. Adapted from [118] (CC BY 4.0).

carried out. A schematic of a more complex testing structure that was prepared for subsequent ultramicrotomy and SEM imaging is depicted in panel (B). In particular, it consists of a block of the same size as before, but is split into different regions. These regions are printed with the very same exposure power of the first exposure $P_1 = 35$ mW, but with different second exposure powers P_2 . The sectioning plane in parallel to which cutting was carried out by ultramicrotomy is indicated. In doing so, the different material properties resulting from different writing parameters can be characterized within one single structure.

In panel (C), SEM images recorded from a ultramicrotome section of the test structure from panel (B) are presented. In particular, an overview image is shown, with insets magnifying different details of the structure. As can be easily seen from those images, the porosity Φ decreases when increasing P_2 , with the leftmost region of the structure approaching almost solid polymer material, with a porosity below 5%. Hence, this finding is qualitatively consistent with the observation presented in (A), since light-scattering is expected to vanish for the limit of $\Phi = 0\%$. The observation of decreased porosity for the double exposure writing strategy is also in agreement with the interpretation of monomer diffusion into the pores and subsequent polymerization in the second exposure step.

As a side note, it should be mentioned that for the extraction of the porosity as described in section 5.3.1.2, all images were normalized and then binarized using the very same threshold value. This single threshold value was calculated from the image in the middle using Otsu's method. This procedure was chosen since Otsu's method does not yield reasonable threshold values for the two images showing regions with low porosity. In more detail, Otsu's method fails because it is a histogram-based method, and there is no significant contribution of the pores to the intensity histogram of the image for small porosities. For the higher-porosity regions this procedure does not alter the extracted threshold value significantly, as compared to the porosities extracted when using individual threshold values per image.

An inset highlighting the transition region within regions printed with different porosities is depicted in panel (D). The transition region is remarkably sharp, and the change in porosity takes place on a length scale below $1\ \mu\text{m}$.

Finally, panel (E) displays a zoom-in into the top region of the polymer structure. In panel (A), we have already seen that this region has a white appearance (even for regions with low porosity). In accordance with this observation, in the SEM image, a high porosity is observed in this region.

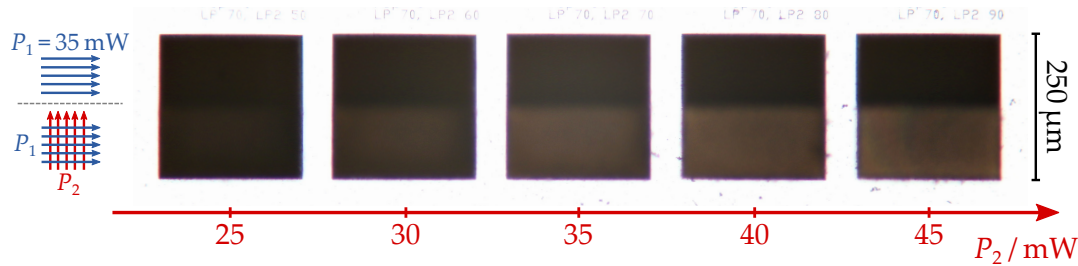


Figure 5.15: Transmitted-light optical microscopy image of solid blocks similar to the ones shown in Figure 5.14(A). The upper halves are printed by a single exposure with exposure power P_1 and can be seen as a reference. The lower halves of the blocks are printed using the double-exposure strategy, and P_2 is varied, while keeping $P_1 = 35$ mW constant. For higher exposure powers P_2 , a brighter appearance of the double-exposed parts is observed, which results from an increased optical transmission due to reduced porosity. This result is in consistency with the observations from electron microscopy, and is another demonstration of the tunability of the porosity during 3D printing.

5.4.3 Optical Characterization

In the last sections, we have seen that the porosity of the 3D printed nanoporous material is significantly influenced by the writing parameters. This allows to realize also materials exhibiting very low porosities. The changes in porosity should be accompanied by changes in the light-scattering coefficient μ_s . In consistency with the expectation that also small light-scattering coefficients can be realized, reflected-light optical microscope images (see Figure 5.14)(A) show that the *volume* of the material appears transparent, although still exhibiting a thin white (i.e., light-scattering and hence porous) region on top of the structures. Likewise, in transmitted-light optical microscopy images as depicted in Figure 5.15, double-exposed structures exhibit a higher optical transmission for increased exposure doses. The observation of a thin porous region on top of the structures can also be made in SEM images taken on ultramicrotomy sections (see Figure 5.14(E)).

Measurements of the light-scattering coefficient for the nanoporous polymer printed by single- and double-exposure writing will be presented in the following. These measurements are carried out as already described in section 5.3.2. In detail, the ballistic transmission is measured through cylinders with a diameter of $350 \mu\text{m}$ and heights ranging from $2 \mu\text{m}$ to $30 \mu\text{m}$.

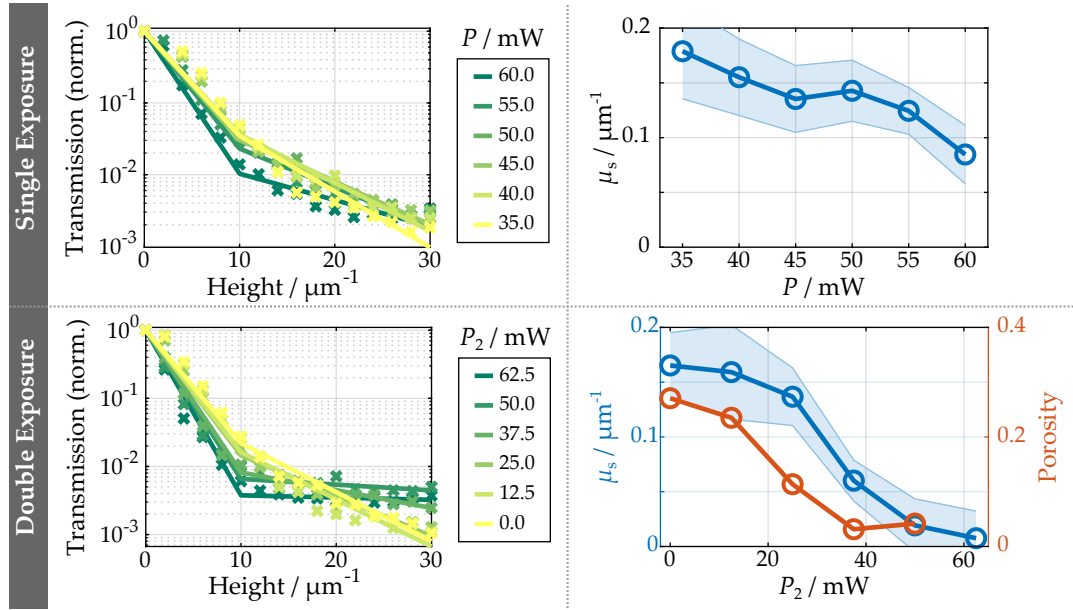


Figure 5.16: Measurements of the ballistic transmission, and extracted light-scattering coefficients μ_s for porous material written by single (top) and double (bottom) exposure, respectively. The measured transmission is plotted on the left side, and light-scattering coefficients are extracted by fitting a model as described in the main text. The slope of the fitted curves on the right corresponds to the volume light-scattering coefficient $\mu_{s,2}$. On the right-hand side, $\mu_{s,2}$ is plotted, respectively. The shaded regions correspond to 95% confidence intervals. Adapted from [118] (CC BY 4.0).

Furthermore, to account for the thin light-scattering layer on top of the structures, the model presented in section 5.3.2 is extended as follows: assuming that the cylinders consist of a bimaterial stack of two slabs made from different materials with light-scattering coefficients $\mu_{s,1}$ and $\mu_{s,2}$, the ballistic transmission $I(z)/I_0$ can be formulated as

$$\ln\left(\frac{I(z = z_1 + z_2)}{I_0}\right) = -\mu_{s,1}z_1 - \mu_{s,2}z_2. \quad (5.6)$$

Here, z_1 and z_2 denote the thicknesses of the individual slabs, and these two quantities add up to the total height z of the 3D printed cylinders that are examined.

Measurements of the ballistic transmission are depicted in Figure 5.16. In particular, measurements taken on structures 3D printed by a conventional single- and the double-exposure writing strategy are displayed. For

extraction of the light-scattering coefficient in the volume $\mu_{s,2}$, the model from above is fitted to the data (left-hand side). In these curves, the slope on the right-hand side corresponds to $\mu_{s,2}$. This quantity is also plotted in dependence of the exposure power on the right-hand side. The shaded regions correspond to 95% confidence intervals.

For a better intuition, it can also be instructive to think in terms of the scattering mean free path $l_s = 1/\mu_s$. A typically occurring scattering coefficient of $0.15 \mu\text{m}^{-1}$ corresponds to a scattering mean free path of $l_s \approx 7 \mu\text{m}$.

For the structures printed by conventional single exposure, a moderate decrease of the volume light-scattering coefficient $\mu_{s,2}$ is observed with increasing exposure power P . For the structures printed by the double-exposure printing strategy, the decrease of the light-scattering coefficient with increasing second exposure power P_2 is significantly more pronounced. For high P_2 the $\mu_{s,2}$ even approaches zero within the uncertainty of the measurement. Hence, it can be concluded that the light-scattering coefficient within the volume of the material can be tuned across a wide range, and both the regime of ballistic light propagation and the regime of multiple scattering are attainable within this tuning range.

These observations are furthermore in qualitative agreement with the observed decrease in porosity that could be also seen in the SEM images obtained on ultramicrotome sections for single exposure (Figure 5.13) and for double exposure (Figure 5.14).

5.5 A MINIATURIZED ULBRICHT SPHERE

In the previous sections, I have discussed details on the photoresist, focused on the strategies employed for printing the resist and have characterized the nanoporous 3D printed polymer in terms of porosity and light-scattering. However, I have not yet explored possible applications of the nanoporous material. In this section, I present a concept of a possible application: An Ulbricht sphere that is 3D printed from the phase-separating resist. 3D printing of Ulbricht spheres has been demonstrated before [130], however, the charm in the approach presented in this section is that the nanoporous printed material exhibits a high reflectivity by itself, such that additional coating steps are not required. Furthermore, realizations on small size scales are possible.

Generally, Ulbricht spheres are widely used in radiometry for measuring

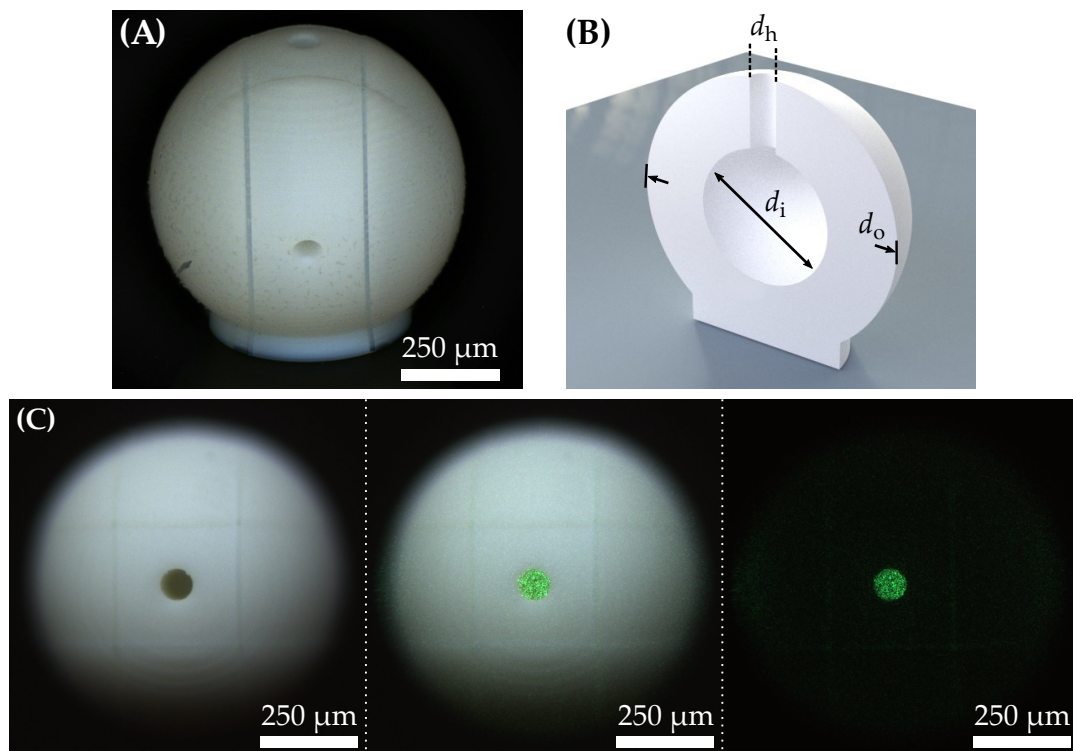


Figure 5.17: Demonstration of a 3D printed Ulbricht sphere. **(A)** Oblique-view optical microscope image of the hollow Ulbricht sphere printed from the phase-separating photoresist. The sphere features a hole at the top and a hole at the side for light in- and outcoupling. **(B)** Design of the Ulbricht sphere, cross-sectional view. The outer diameter $d_o = 800 \mu\text{m}$, the inner diameter $d_i = 400 \mu\text{m}$ and the hole diameter $d_h = 80 \mu\text{m}$ are indicated. **(C)** For testing the functionality, a laser (wavelength $\lambda = 532 \text{ nm}$) is focused through the opening at the side, and the sphere is observed from the top. Switching off white-light illumination, light predominantly emerges from the hole at the top at the sphere. Due to their high reflectivity, the walls transmit few light and hence appear dark. Consequently, the realization and calibration of fully functional Ulbricht spheres printed from the phase-separating photoresist is a plausible application. Adapted from [118] (CC BY 4.0).

the total power of light emerging from a light source, or for measuring the total optical transmission or reflectance of an object. For this purpose, they consist of a hollow sphere that has a coating on the inside with a very high ($\geq 90\%$) diffuse reflectivity across a wide wavelength regime. Commonly, materials such as porous polytetrafluoroethylene (PTFE) are used for this

purpose. For practical reasons, additionally, Ulbricht spheres also feature openings for the insertion of measurement samples and detectors.

Suppose the case where a light source with an arbitrary angular emission pattern is placed into the Ulbricht sphere. Herein, light rays emerging from the source are therefore reflected from the walls and are “trapped” in the sphere, until they are absorbed or transmitted through the walls. Hence, due to multiple reflections, the irradiance (the light power per surface area) is distributed isotropically across the inside of the sphere. Consequently, one single measurement of the irradiance at one spot on the inside is sufficient to retrieve the total power that is emitted from the light source in all directions in space. The same result could be obtained by scanning a detector around the light source across the whole solid angle and performing an integration (i.e., using a goniophotometer). However, employing an Ulbricht sphere is by far more simple and hence widely done. As Ulbricht spheres perform the integration step automatically, they are also often called “integrating spheres”.

An Ulbricht integrating sphere printed from the phase-separating resist is depicted in Figure 5.17. Panel (A) shows an oblique-view reflection-mode microscope image of the printed sphere. It features a hole at the top, and a hole at one side for light in- and outcoupling.

A cross-sectional computer rendering of the sphere is shown in panel (B). The outer diameter of the hollow sphere is $d_o = 800 \mu\text{m}$, the inner diameter is $d_i = 400 \mu\text{m}$, and the holes have a diameter of $d_h = 80 \mu\text{m}$. Consequently, the walls of the sphere have a thickness of $100 \mu\text{m}$. The sphere was printed with a single-exposure writing strategy at a relatively low exposure power of 35 mW , and the standard printing parameters described in the appendix (section A.2.3).

In particular, the thickness of the walls ($100 \mu\text{m}$) should be much larger than the scattering mean free path $l_s \approx 7 \mu\text{m}$, which is fulfilled for the given values. In this case, back-scattering of light impinging onto them becomes prominent, and hence, they exhibit sufficient reflectivity. Based on this reasoning, it also becomes clear that scaling down the Ulbricht sphere and hereby also reducing the thickness of the walls is not a promising avenue, because this would also reduce the reflectivity of the walls.

For testing the printed sphere, a green ($\lambda = 532 \text{ nm}$) laser is focused into the hole at the side, while observing the hole at the top. Optical microscope images taken in these experiments are depicted in panel (C). For clarity, an image is shown on the left side, where the laser is switched off, but white-light illumination is switched on. When switching on the laser (shown

in the middle image) light emerging from the hole at the top can be observed. When switching off the white light (right image), it can be seen that the walls of the Ulbricht sphere appear dark, as they exhibit a high diffuse reflectivity and few light is transmitted through them.

In summary, this first test is a plausible indication that the phase-separating photoresist can in fact be used to 3D print functional miniaturized Ulbricht-style integrating spheres. However, towards this goal, more detailed characterizations and calibrations would be essential.

5.6 CONCLUSION

In this chapter I have presented a photoresist that combines the concepts of 3D printing and self-assembly. Hereby, advantages from both fields are combined into one fabrication method, which enables the printing of 3D microstructures from a material that exhibits a nanoporosity on the scale of tens of nanometers throughout the volume. Specifically, the size scale of this nanoporosity is not accessible by 3D printing methods, and hence, the realization of the same nanoporous structures would not have been possible before.

In particular, I have explained the photoresist's underlying mechanism, which is polymerization-induced phase separation. Herein, the photoresist contains polymerizable as well as non-polymerizable components. Upon polymerization of the photoresist (i.e., 3D printing it), a phase separating into a polymer-rich and a polymer-lean phase occurs. After washing out the polymer-lean phase using organic solvents, a nanoporous polymer remains. With respect to optical 3D printing methods, this concept is charming because the unpolymerized photoresist inherently does not show light-scattering, as it exhibits a spatially homogeneous refractive index.

Moreover, I have presented an optimization of the printing conditions that was required to achieve the 3D printing of spatially homogeneous material properties. In this context, I have furthermore demonstrated that the material's porosity can be tuned during 3D printing by precisely adjusting the printing parameters and employing adequate printing strategies. Hence, materials with different porosity can be printed from one single photoresist. In addition, the phase-separating photoresist could also be printed into multi-material structures using the microfluidic injection system described in chapter 4.

For characterization of the 3D printed material, SEM images were recorded

from ultrathin sections, and image analysis was carried out. Hereby, porosity and pore size distribution could be examined in the volume of the printed material. In addition, the optical light-scattering properties were examined.

Finally, I have presented a possible application of the nanoporous material that makes use of its high reflectivity resulting from strong light-scattering that occurs in the volume: a 3D printed miniaturized Ulbricht integrating sphere. First experimental tests indicate that fully functional miniaturized measurement devices could be manufactured and calibrated. Further applications of the 3D printed nanoporous polymer could lie in, for example, the realization of ultrahydrophobic structures, the printing of cages for biological single-cell experiments or in the realization tailored light-scattering 3D structures such as diffuse-light invisibility cloaks [63].

Chapter 6

6 CONCLUSIONS AND OUTLOOK

In the present thesis, I have explored various aspects of multi-material 3D laser microprinting. The first part of this thesis covered the printing of multi-material 3D microstructures by multi-step lithography. On the contrary, the second part treated a photoresist system that combines 3D printing with self-assembly and hereby enables the fabrication of nanoporous 3D microstructures. In this chapter, I will briefly summarize the contents of this thesis, and will give an outlook.

In **chapter 2**, I have described the underlying principles that are important for a detailed understanding of the present thesis. In section 2.1, I have started by explaining the fundamental concepts of 3D laser microprinting. In this context, I have elaborated on the threshold model, which is commonly used to describe the photoresist's response to exposure to light. Subsequently, I have investigated the 3D printing resolution in 3D laser microprinting. Then, in section 2.3, I have given a short introduction into selected aspects of fluid mechanics that are of major interest for the design of microfluidic systems. In particular, I have introduced the definition of the viscosity and have discussed fluid dynamics in the regime of laminar flow.

PART I OF THIS THESIS dealt with the fabrication of multi-material microstructures by 3D printing different photoresists sequentially. I have started discussing multi-step 3D laser microprinting by an application example: in **chapter 3**, I have presented a novel type of security feature that consists of a three-dimensional microstructure printed from various photoresists with different fluorescence properties. In the photoresists, colloidal CdSeS/ZnS quantum dots are used as a fluorescent additive. These 3D fluorescent security features consist of a non-fluorescent 3D cross-grid as a support structure, with fluorescent markers (with different emission colors) distributed into it. I have described the fabrication of those structures by multiple 3D print-

ing steps: the different photoresists are printed sequentially, with manual processing steps in between. For 3D imaging and hence for readout of the structures, I have employed confocal laser scanning microscopy. The structures have shown good stability towards photobleaching.

With increasing number of materials (i.e., photoresists) to be printed into a single microstructure, its fabrication becomes increasingly time-consuming, effortful, and prone to errors. In this context, the experimental challenges faced in chapter 3 have served as a motivation for developing an integrated multi-material printing system which I have presented in chapter 4. To the best of my knowledge this work represents the first implementation of a fully integrated multi-material 3D laser microprinting system that is capable to fabricate complex multi-material 3D microstructures. After briefly reviewing other research work, I have started by explaining the boundary conditions for the implementation of such a system into a commercial 3D laser microprinting setup, and by giving an overview of the experimental implementation that was eventually realized within this thesis. I have then commenced by discussing different fluidic components in detail. The central part of the integrated microfluidic injection system is a home-built sample holder. It hosts a chamber into which 3D microstructures can be directly printed through a thin glass window which enables the use in combination with high-NA oil-immersion objective lenses. Furthermore, up to ten different liquids (photoresists and solvents) can be injected into the chamber, such that photoresists can be exchanged automatically in the printing procedure. As a demonstration example, I have fabricated multi-material 3D fluorescent security features that are similar to the ones shown in chapter 3, but are printed from four fluorescent materials (instead of two) at a four-fold density of the fluorescent parts. By performing confocal laser scanning microscopy on those structures, I have shown that the integrated microfluidic printing system enables the 3D printing of a large number of different materials into single structures at micrometer precision.

PART II OF THIS THESIS dealt with the development of new printable materials for 3D laser microprinting. In particular, in chapter 5, I have combined the two distinct approaches of 3D printing and self-assembly to create a novel photoresist system from which, for the first time, inherently nanoporous 3D hierarchical microstructures can be directly fabricated by 3D laser microprinting. In doing so, materials with physical properties that are very different from “conventional” non-porous photoresists can be realized. Herein, 3D structuring on the microscale is achieved by 3D printing, whereas

the porous substructure on the scale of tens of nanometers is introduced by the mechanism of polymerization-induced phase separation. This mechanism leads to a phase separation between solvents and the newly formed polymer in the photoresist upon 3D printing it. Due to the nanoporosity, the structures exhibit strong light scattering and hence appear white. This is in contrast to photoresists available so far, which commonly yield polymeric solid materials which exhibit a glass-like appearance. Notably, the unpolymerized photoresist exhibits a homogeneous refractive index distribution and hence does not show light scattering prior to polymerization. This property only enables 3D printing of a strongly light scattering material by the optical method of 3D laser microprinting, which would otherwise be perturbed by light scattering. For characterization of the 3D printed nanoporous materials, I have analyzed SEM images that were taken on thin ultramicrotome sections prepared from 3D printed samples. Furthermore, I have characterized the light scattering properties of the material. In this context, I have shown that the porosity can be tuned during 3D printing, such that porous as well as non-porous material can be 3D printed. Hence, this constitutes a form of multi-material printing from a single photoresist. Finally, as an application example, I have 3D printed and tested an Ulbricht integrating sphere, which makes use of the high reflectivity resulting from the strong light scattering properties of the nanoporous polymer material.

OUTLOOK

It appears safe to assume that functional 3D microstructures printed from several different materials by 3D laser microprinting will be seen more frequently in the future. This trend can be expected to be amplified by the increasingly large number of different photoresist materials available for 3D laser microprinting.

In the course of the considerable progress in the field of 3D fabrication technologies, it also appears probable that more forgery-proof security features based on this progress will come into use in the future. In this context, the use of the 3D fluorescent multi-material microstructures I have presented within this thesis as security features is well conceivable. In particular, since these structures are printed from multiple different photoresists, it would be possible to extend on the different material properties printed within the microstructures, hereby increasing the level of counterfeiting security even further. Besides different colors of fluorescence, it would be conceivable to,

for example, realize different refractive indices, employ fluorophores with characteristic spectral fingerprints, or employ light scattering materials.

With respect to the microfluidic injection system presented in chapter 4, a number of research groups have already started adapting the same or a similar system for their own research goals. While the injection system presented in this thesis has a number of limitations—most importantly, the limited maximum print height—it can already be employed for the efficient manufacturing of many different types of multi-material structures, beyond those presented within this thesis. Future applications could for example include achromatic micro optical systems and cage-like environments for biological single-cell studies. Furthermore, in order to circumvent the limitation of maximum print height, improved versions as well as alternative concepts of systems for the integrated 3D laser microprinting of multiple photoresists might pop up in the future. Ideally, such systems would be integrated into readily available commercial 3D laser microprinters, such that the 3D printing of multi-material microstructures eventually becomes accessible for a large number of users.

In the context of multi-material printing, the phase-separating photoresist presented in chapter 5 in a broader sense expands on the number of photoresist materials that can be printed by 3D laser microprinting, and could be also printed using the microfluidic injection system. Applications of this photoresist material might include realizations of diffuse-light invisibility cloaks, environments for experiments on biological cells, microfluidic filter elements, and superhydrophobic surfaces. Future work on similar photoresists could, for example, involve a wider variety of different porogens that allow for custom-tailored pore size distributions in the 3D printed polymer. Furthermore, it would be desirable to reduce the vulnerability of the printing process to atmospheric oxygen, hereby lifting the necessity of 3D printing under a nitrogen atmosphere if spatially homogeneous porosities are to be printed. Along this line, the development of phase-separating photoresists based on chemistries other than the oxygen-prone radical polymerization of (meth)acrylates (such as thiol-ene photo-polymerizations) appears promising.

In the introduction of this thesis, I have argued that in addition to the 3D structuring abilities of 3D printing, it would be at the same time of utter interest to exert free control over the 3D printed material. Within the present thesis, I have contributed towards reaching this vision within the scope of 3D laser microprinting. In particular, I have presented new fabrication

strategies and an integrated system for printing multi-material structures from multiple different photoresists, as well as a novel photoresist material. I am convinced that further progress into these directions will eventually enable the realization of more and more complex three-dimensional functional microstructures, and I am full of curiosity to see the further development.

A

Appendix A

APPENDIX

A.1 PHOTORESIST FORMULATIONS

In what follows, the preparation of the photoresists employed throughout this thesis is described.

A.1.1 Photoresists for 3D Fluorescent Security Features (chapters 3 and 4)

A.1.1.1 Non-Fluorescent Photoresist

For preparation of the non-fluorescent photoresist, 1 %(wt) (chapter 3) or 2 %(wt) (chapter 4) of Irgacure 819 were dissolved in pentaerythritol triacrylate (PETA; technical grade; Sigma-Aldrich) and ultrasonicated for 30 min until a clear mixture was obtained.

A.1.1.2 Fluorescent Photoresists Containing Quantum Dots

The photoresists containing quantum dots (Trilite Fluorescent Nanocrystals in toluene solution 1 mg mL^{-1} , Cytodiagnosics) with emission wavelengths 450 nm, 525 nm, 575 nm, or 665 nm were prepared by the following routine:

1. **Mix A:** 2 %(wt) (chapter 3) or 4 %(wt) (chapter 4) of Irgacure 819 (Ciba Inc.) were added to PETA and ultrasonicated for 30 min until a clear solution was obtained.
2. **Mix B:** Mix A was blended with Tricyclo[5.2.1.0^{2,6}]decanedimethanol diacrylate (TDDDA; technical grade; Sigma-Aldrich) and toluene (99.8%; Sigma-Aldrich) in a volume ratio of 1:1:2.
3. **Adding of quantum dots:** While stirring on a magnetic stirrer, 10 %(wt) of quantum dot solution was slowly added to Mix B (one of the different

emission wavelengths).

4. **Evaporation:** Finally, while continuously stirring, toluene was evaporated from the photoresist at an elevated temperature of 35 °C for 20 h.

The prepared photoresists still contained about 10 %(vol) of toluene.

A.1.1.3 Fluorescent Photoresists Containing Organic Dyes

The photoresists containing organic dyes (i.e., Atto 647N or Atto 565) were prepared by the following routine:

1. **Mix A:** 4 %(wt) of Irgacure 819 (Ciba Inc.) were added to PETA and ultrasonicated for 30 min until a clear solution was obtained.
2. **Mix B:** TDDDA was added in a volume ratio of 50 % to Mix A.
3. **Mix C1:** Atto 647N (AttoTEC GmbH, alkyne functionalized) was dissolved in dimethyl sulfoxide (DMSO; 99 %; Merck) in a concentration of 0.1 mg mL⁻¹.
4. **Mix C2:** Alternatively, Atto 565 (AttoTEC GmbH, alkyne functionalized) was dissolved in dimethyl sulfoxide (DMSO; 99 %; Merck) in a concentration of 0.1 mg mL⁻¹.
5. **Photoresist 1:** 391 µL of Mix C1 were added to 5 mL of Mix B and stirred for 5 min. The final photoresist contains about 7 %(vol) DMSO and dye molecules in a concentration of 9.3 µM.
6. **Photoresist 2:** Alternatively, 324 µL of Mix C2 were added to 5 mL of Mix B and stirred for 5 min. The final photoresist contains about 6 %(vol) DMSO and dye molecules in a concentration of 9.4 µM.

A.1.2 Phase-Separating Photoresist (chapter 5)

The photoresist was obtained by adding the following components into a glass bottle.

- 52.94 %(wt) PETA
- 22.43 %(wt) dodecyl acetate (Sigma-Aldrich)
- 22.43 %(wt) octadecyl acetate (TCI Chemicals)
- 2.12 %(wt) Irgacure 819 (Ciba)

- 0.07 % 2,2,6,6-tetramethylpiperidinyloxy (TEMPO; Sigma-Aldrich)

A clear mixture was obtained by treatment in an ultrasonic bath for 30 min. Prior to printing, the oxygen concentration was depleted in the photoresist by bubbling it with nitrogen gas for 5 min. Furthermore, printing was carried out under a nitrogen atmosphere. More details on the printing process are found in section A.2.3 of this chapter.

A.2 FURTHER EXPERIMENTAL DETAILS

A.2.1 Security Feature Samples

Further experimental details for the printing and the fluorescence microscopy on the security feature structures discussed in chapter 3 and 4 are listed in this section.

A.2.1.1 3D Laser Microprinting

For printing the non-fluorescent backbone of the security feature structures using the Nanoscribe Photonic Professional GT 3D printer, the following printing parameters were employed that are not mentioned specifically in the main text:

- Objective lens: Plan-Apochromat 63 \times /1.40, Carl Zeiss (chapter 3) or LD LCI Plan-Apochromat 63 \times /1.2 Imm Korr DIC, Carl Zeiss (chapter 4).
- Slicing distance: 0.4 μm
- Hatching distance: 0.3 μm
- Each rod of the 3D cross-grid consists of 3 to 4 lines being printed (both axially and laterally). For rods that are oriented perpendicular to the optical axis, individual lines are always printed *along* the rod direction.
- Focus velocity: 1.5 cm s^{-1}
- Typical writing powers: 100 % (chapter 3), 66 % (chapter 4)

Further parameters of cylindrical fluorescent markers shown in chapter 3:

- Objective lens: Plan-Apochromat 63 \times /1.40, Carl Zeiss
- Slicing distance: 0.4 μm

- Hatching distance: $0.3\ \mu\text{m}$
- Focus velocity: $1\ \text{cm s}^{-1}$
- The fluorescent markers consisted of 5 slices along the axial direction
- They have a nominal outer diameter of $5\ \mu\text{m}$
- The laser power was increased linearly from the uppermost to the lowermost layer of fluorescent markers printed, typically from $\approx 90\%$ to $\approx 100\%$

Printing parameters for rectangular markers shown in chapter 4 (section 4.3.3):

- Objective lens: LD LCI Plan-Apochromat $63\times/1.2$ Imm Korr DIC, Carl Zeiss
- Slicing distance: $0.2\ \mu\text{m}$
- Hatching distance: $0.2\ \mu\text{m}$
- Focus velocity: $1\ \text{cm s}^{-1}$
- The fluorescent markers consisted of 6 slices in axial direction
- The rectangular fluorescent markers have a nominal lateral extent of $3\ \mu\text{m} \times 3\ \mu\text{m}$
- The laser power is increased linearly from the uppermost to the lowermost layer of fluorescent markers printed, typically from $\approx 70\%$ to $\approx 85\%$

Alignment in between the consecutive printing steps was carried out by aligning to markers that were printed in the first step from the non-fluorescent photoresists.

A.2.2 Laser Scanning Fluorescence Microscopy

All fluorescence images shown throughout this thesis have been recorded using a commercial confocal laser scanning fluorescence microscope (LSM 510 Meta, Carl Zeiss). This microscope is equipped with a number of laser lines for excitation, a set of filters for discrimination of fluorescence signals, a set of different objective lenses, and different detectors. In particular, it features two photomultiplier tubes, such that two different fluorescence signals can be recorded simultaneously. Furthermore, all images have been taken using the objective lens Plan-Apochromat $63\times/1.40$, Carl Zeiss. For imaging, a droplet of immersion oil (Immersol 518F) was applied directly on top of the samples (i.e., the samples were not imaged through the glass

substrate). The objective lens was immersed into this oil droplet (i.e., imaging was not carried out through the glass substrate). All images were recorded at a image resolution of 1024×1024 pixels. Typically, image stacks of ≈ 150 images with a spacing along the z -axis of $0.37 \mu\text{m}$ were taken. Other parameters were as follows:

- *One emission color (section 3.4.1)*: Excitation at $\lambda = 405 \text{ nm}$ with a power of $P_{405} = 155 \mu\text{W}$. For discrimination of the fluorescence signal which is centered around $\lambda_{\text{fl}} = 525 \text{ nm}$, a bandpass filter transmitting light between 505 to 550 nm was employed. The pinhole diameter was set to 1 Airy unit. The pixel dwell time was $1.6 \mu\text{s}$.
- *Two emission colors (section 3.4.2)*: Same as for one emission color, but simultaneous detection of two fluorescence channels (for the quantum dots emitting at $\lambda_{\text{fl},1} = 450 \text{ nm}$ and $\lambda_{\text{fl},2} = 525 \text{ nm}$). For this purpose, a chromatic beam splitter at 490 nm was employed, combined with an additional band pass filter transparent between 420 to 480 nm . The pixel dwell time was $3.2 \mu\text{s}$.
- *Four emission colors (section 4.3.3)*: For recording all four fluorescence channels, it was necessary to image each image section *twice* with different filter settings. In doing so, the red and the green fluorescence channels were obtained simultaneously, using a chromatic beam splitter at $\lambda_{\text{c},1} = 565 \text{ nm}$ and band-pass filters transparent between $505 \text{ nm} < \lambda_{\text{BP},1} < 550 \text{ nm}$ and a long-pass filter with $\lambda_{\text{LP}} > 650 \text{ nm}$ in the beam paths of the photomultiplier tubes, respectively. Likewise, the blue and the orange channel are captured simultaneously using a chromatic beam splitter at $\lambda_{\text{c},2} = 490 \text{ nm}$, and two band-pass filters with $420 \text{ nm} < \lambda_{\text{BP},2} < 480 \text{ nm}$ and $575 \text{ nm} < \lambda_{\text{BP},3} < 615 \text{ nm}$. For excitation, two lasers with wavelengths $\lambda_1 = 405 \text{ nm}$ and $\lambda_2 = 488 \text{ nm}$ were used. The excitation powers were $P_1 = 236 \mu\text{W}$ and $P_2 = 109 \mu\text{W}$, respectively, measured in the back focal plane of the objective lens. The pixel dwell time was $1.28 \mu\text{s}$. Hence, a single image section of the microstructure containing $1024 \text{ px} \times 1024 \text{ px}$ was obtained in 6.3 s .

A.2.3 3D Printing of Porous Samples

The phase-separating photoresist was printed using a $25\times$ objective lens (LCI Plan-Neofluar $25\times/0.8 \text{ Imm Korr DIC}$, Carl Zeiss) in the dip-in configuration (refractive index correction ring in standard setting for IP-S resist).

Furthermore, printing was carried out under nitrogen atmosphere (unless indicated otherwise in the main text). This was realized by a nitrogen-flooded chamber, which is depicted in the photograph in Figure A.1. A continuous flow of nitrogen was flushed into this chamber during printing using the same electronic gas pressure controller that was also used in the microfluidic setup (Elveflow OB1 MK3).

Furthermore, prior to printing, the phase-separating photoresist was bubbled with nitrogen gas for 5 min to deplete the oxygen concentration in the photoresist. Printing was typically started by printing dummy structures to further deplete residual oxygen. Parameters for those cylinders were: Diameter 350 μm , height 100 μm . In total, an array of 2×5 of such cylinders was printed, with a distance of 500 μm between individual structures. Only then, printing of the actual structures was carried out.

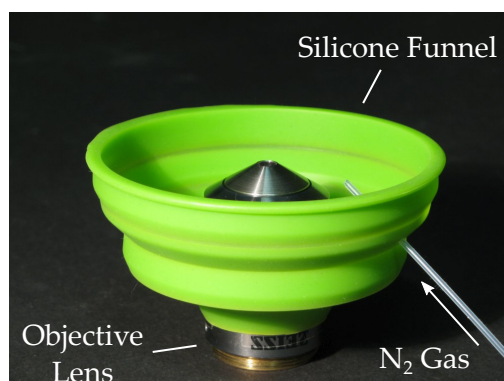


Figure A.1: The sample is kept under nitrogen atmosphere in a chamber that is made up of a silicone funnel, which is pulled over the objective lens. The 3D printer's sample holder seals the chamber towards the top. Adapted from [118] (published under [CC BY 4.0](#) license).

Furthermore, unless otherwise noted, the standard printing parameters for all structures shown in this chapter are: slicing distance 1 μm , hatching distance 0.5 μm , unidirectional hatching, laser power 50 mW. All structures were printed with the objective lens LCI Plan-Neofluar 25 \times /0.8 Imm Korr DIC, Carl Zeiss.

A.2.4 Supercritical Drying

Supercritical drying was employed only for the nanoporous polymer structures presented in chapter 5. For this purpose, a commercial device (Leica EM CPD300) was used. In particular, after printing, the samples were immersed in acetone for 30 min for development. The sample was then placed in the acetone-filled drying chamber. In the drying process, the chamber was cooled down to 14 °C, and the acetone in the chamber was replaced by liquid CO₂. The chamber was subsequently heated above the critical point of CO₂ to 40 °C while slowly releasing CO₂ to keep the pressure below 100 bar. After slowly releasing all carbon dioxide from the chamber, drying was finished. The entire process took about 60 min.

A.2.5 Adhesion Improvement by Silanization

In 3D laser microprinting, commonly, a silanization treatment is applied on the glass substrate to improve attachment of 3D-printed structures, such that the structures do not fall off during or after development. In particular, in this work, silanization was carried out by

1. Cleaning of the glass substrates using an plasma oven for 15 min, such that hydroxy groups stick out of the surface.
2. Immersion of the substrates in a solution of 3-(trimethoxysilyl)propyl methacrylate in toluene at a concentration of 1 mM for 30 min. During this step, the silane molecules attach to the hydroxy groups at the surface of the glass substrates. Acrylate- or methacrylate-based photoresists can react to the these silane molecule, which is the reason for the improved adhesion in later 3D printing steps.
3. Washing of the substrates in toluene and isopropyl alcohol.
4. Blow-drying of the substrates with a nitrogen gun.

Except for the nanoporous polymer samples on which ultramicrotomy was carried out, this silanization procedure was carried out for all samples presented throughout this work.

A.3 RESOLUTION LOSS UNDER OXYGEN-DEPLETED CONDITIONS

In section 5.2.4, I have discussed homogeneity and reproducibility issues that occurred when printing the phase-separating photoresist under atmospheric conditions. These issues were traced back to gradients in the oxygen concentration in the phase-separating photoresist. For treating these issues, printing was carried out under nitrogen atmosphere and, furthermore, the polymerization quencher TEMPO was added to the photoresist. In addition to this discussion, results for the printing under oxygen-depleted conditions without any additional polymerization quencher added (i.e., no TEMPO) will be presented in the following.

Conceptually, in this case, the number of possible termination reactions in the radical polymerization is reduced (see also section 2.2). Scanning electron micrographs taken on different samples that have been printed under nitrogen atmosphere are depicted in Figure A.2. In particular, the photoresist was *not* bubbled with nitrogen prior to printing, such that the oxygen concentration in the photoresist starts from the equilibrium value under normal conditions, and is then depleted successively as printing time progresses. Panel (A) shows nominally identical cylinders (diameter $d = 350\ \mu\text{m}$, nominal height $h = 100\ \mu\text{m}$, exposure power 50 mW). The printing order of the cylinders is from the top right to the bottom left. Panel (B) shows similar cylinders ($h = 16\ \mu\text{m}$) printed at later times on the same sample. Notably, in both cases, spatially uncontrolled polymerization is observed in regions that have only seen low exposure doses. Specifically, the “threads” connecting the cylinders in panel (B) stem from the movement of the objective lens through the photoresist during printing.

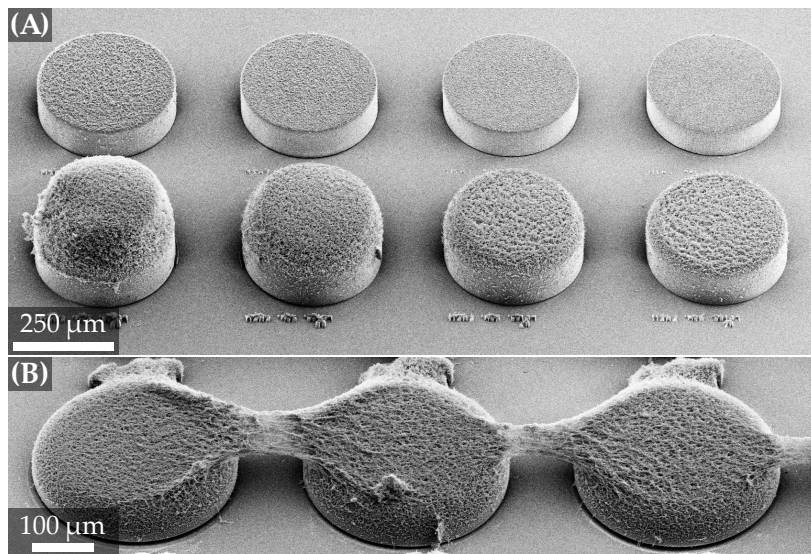


Figure A.2: Oblique-view SEM images of cylinders (diameter $d = 350 \mu\text{m}$, nominal height $100 \mu\text{m}$) printed into the phase-separating photoresist under nitrogen atmosphere. The photoresist did *not* contain the polymerization quencher TEMPO (see also section 5.2.4). (A) Sequence (printing order from top right to bottom left) of nominally identical cylinders. Prior to printing, the photoresist was *not* bubbled with N_2 gas, such that during 3D printing, the concentration of oxygen is successively depleted in the photoresist. As a result, spatially undefined polymerization is observed. (B) Another example of spatially undefined polymerization in the case of oxygen depletion: polymer filaments connecting different cylinders (nominal height $16 \mu\text{m}$).

BIBLIOGRAPHY

- [1] M. A. Skylar-Scott, J. Mueller, C. W. Visser, and J. A. Lewis, "Voxelated soft matter via multimaterial multinozzle 3D printing", *Nature* **575**, 330–335 (2019) (cited on pages 4, 51).
- [2] F. Klein, B. Richter, T. Striebel, C. M. Franz, G. v. Freymann, M. Wegener, and M. Bastmeyer, "Two-Component Polymer Scaffolds for Controlled Three-Dimensional Cell Culture", *Adv. Mater.* **23**, 1341–1345 (2011) (cited on pages 4, 8, 32, 50).
- [3] M. Schmid, S. Thiele, A. Herkommer, and H. Giessen, "Three-dimensional direct laser written achromatic axicons and multi-component microlenses", *Opt. Lett.* **43**, 5837–5840 (2018) (cited on pages 4, 8, 32).
- [4] K. Weber, D. Werdehausen, P. König, S. Thiele, M. Schmid, M. Decker, P. W. De Oliveira, A. Herkommer, and H. Giessen, "Tailored nanocomposites for 3D printed micro-optics", *Opt. Mater. Express* **10**, 2345 (2020) (cited on page 4).
- [5] C. Barner-Kowollik, M. Bastmeyer, E. Blasco, G. Delaittre, P. Müller, B. Richter, and M. Wegener, "3D Laser Micro- and Nanoprinting: Challenges for Chemistry", *Angew. Chem. Int. Ed.* **56**, 15828–15845 (2017) (cited on page 4).
- [6] C. A. Spiegel, M. Hippler, A. Münchinger, M. Bastmeyer, C. Barner-Kowollik, M. Wegener, and E. Blasco, "4D Printing at the Microscale", *Adv. Funct. Mater.* **30**, 1907615 (2020) (cited on page 4).
- [7] H. Zeng, D. Martella, P. Wasylczyk, G. Cerretti, J.-C. G. Lavocat, C.-H. Ho, C. Parmeggiani, and D. S. Wiersma, "High-Resolution 3D Direct Laser Writing for Liquid-Crystalline Elastomer Microstructures", *Adv. Mater.* **26**, 2319–2322 (2014) (cited on page 4).
- [8] Z. Xiong, M.-L. Zheng, X.-Z. Dong, W.-Q. Chen, F. Jin, Z.-S. Zhao, and X.-M. Duan, "Asymmetric microstructure of hydrogel: two-photon microfabrication and stimuli-responsive behavior", *Soft Matter* **7**, 10353–10359 (2011) (cited on page 4).

- [9] M. Hippler, E. Blasco, J. Qu, M. Tanaka, C. Barner-Kowollik, M. Wegener, and M. Bastmeyer, "Controlling the shape of 3D microstructures by temperature and light", *Nat. Commun.* **10**, 232 (2019) (cited on pages 4, 32, 50).
- [10] M. Hippler, K. Weißenbruch, K. Richler, E. D. Lemma, M. Nakahata, B. Richter, C. Barner-Kowollik, Y. Takashima, A. Harada, E. Blasco, M. Wegener, M. Tanaka, and M. Bastmeyer, "Mechanical stimulation of single cells by reversible host-guest interactions in 3D microscaffolds", *Sci. Adv.* **6**, eabc2648 (2020) (cited on pages 4, 8).
- [11] T. Tanaka, A. Ishikawa, and S. Kawata, "Two-photon-induced reduction of metal ions for fabricating three-dimensional electrically conductive metallic microstructure", *Appl. Phys. Lett.* **88**, 081107 (2006) (cited on page 4).
- [12] E. Blasco, J. Müller, P. Müller, V. Trouillet, M. Schön, T. Scherer, C. Barner-Kowollik, and M. Wegener, "Fabrication of Conductive 3D Gold-Containing Microstructures via Direct Laser Writing", *Adv. Mater.* **28**, 3592–3595 (2016) (cited on page 4).
- [13] M. M. Zieger, P. Mueller, A. S. Quick, M. Wegener, and C. Barner-Kowollik, "Cleaving Direct-Laser-Written Microstructures on Demand", *Angew. Chem. Int. Ed.* **56**, 5625–5629 (2017) (cited on pages 4, 32, 50).
- [14] R. Batchelor, T. Messer, M. Hippler, M. Wegener, C. Barner-Kowollik, and E. Blasco, "Two in One: Light as a Tool for 3D Printing and Erasing at the Microscale", *Adv. Mater.* **31**, 1904085 (2019) (cited on page 4).
- [15] S. Maruo, O. Nakamura, and S. Kawata, "Three-dimensional microfabrication with two-photon-absorbed photopolymerization", *Opt. Lett.* **22**, 132–134 (1997) (cited on page 7).
- [16] B. H. Cumpston, S. P. Ananthavel, S. Barlow, D. L. Dyer, J. E. Ehrlich, L. L. Erskine, A. A. Heikal, S. M. Kuebler, I.-Y. S. Lee, D. McCord-Maughon, J. Qin, H. Röckel, M. Rumi, X.-L. Wu, S. R. Marder, and J. W. Perry, "Two-photon polymerization initiators for three-dimensional optical data storage and microfabrication", *Nature* **398**, 51–54 (1999) (cited on page 7).

-
- [17] J. H. Strickler and W. W. Webb, "Two-photon excitation in laser scanning fluorescence microscopy", in [CAN-AM Eastern '90 Proceedings Volume 1398](#), edited by R. L. Antos and A. J. Krisiloff (Apr. 1991), pp. 107–118 (cited on page 7).
- [18] J. Serbin, A. Egbert, A. Ostendorf, B. N. Chichkov, R. Houbertz, G. Dommann, J. Schulz, C. Cronauer, L. Fröhlich, and M. Popall, "Femtosecond laser-induced two-photon polymerization of inorganic–organic hybrid materials for applications in photonics", [Opt. Lett.](#) **28**, 301–303 (2003) (cited on page 7).
- [19] J. Serbin, A. Ovsianikov, and B. Chichkov, "Fabrication of wood-pile structures by two-photon polymerization and investigation of their optical properties", [Opt. Express](#) **12**, 5221–5228 (2004) (cited on page 7).
- [20] M. Deubel, G. von Freymann, M. Wegener, S. Pereira, K. Busch, and C. M. Soukoulis, "Direct laser writing of three-dimensional photonic-crystal templates for telecommunications", [Nat. Mater.](#) **3**, 444–447 (2004) (cited on page 7).
- [21] T. Gissibl, S. Thiele, A. Herkommer, and H. Giessen, "Sub-micrometre accurate free-form optics by three-dimensional printing on single-mode fibres", [Nat. Commun.](#) **7**, 11763 (2016) (cited on pages 8, 32, 50).
- [22] T. Gissibl, S. Thiele, A. Herkommer, and H. Giessen, "Two-photon direct laser writing of ultracompact multi-lens objectives", [Nat. Photon.](#) **10**, 554–560 (2016) (cited on page 8).
- [23] P.-I. Dietrich, M. Blaicher, I. Reuter, M. Billah, T. Hoose, A. Hofmann, C. Caer, R. Dangel, B. Offrein, U. Troppenz, M. Moehrle, W. Freude, and C. Koos, "In situ 3D nanoprinting of free-form coupling elements for hybrid photonic integration", [Nat. Photon.](#) **12**, 241–247 (2018) (cited on page 8).
- [24] V. Hahn, P. Kiefer, T. Frenzel, J. Qu, E. Blasco, C. Barner-Kowollik, and M. Wegener, "Rapid Assembly of Small Materials Building Blocks (Voxels) into Large Functional 3D Metamaterials", [Adv. Funct. Mater.](#), 1907795 (2020) (cited on pages 8, 18, 79).

- [25] B. Richter, V. Hahn, S. Bertels, T. K. Claus, M. Wegener, G. Delaittre, C. Barner-Kowollik, and M. Bastmeyer, "Guiding Cell Attachment in 3D Microscaffolds Selectively Functionalized with Two Distinct Adhesion Proteins", *Adv. Mater.* **29**, 1604342 (2017) (cited on pages 8, 32, 50).
- [26] N. Lindenmann, G. Balthasar, D. Hillerkuss, R. Schmogrow, M. Jordan, J. Leuthold, W. Freude, and C. Koos, "Photonic wire bonding: a novel concept for chip-scale interconnects", *Opt. Express* **20**, 17667–17677 (2012) (cited on page 8).
- [27] H. Zeng, P. Wasylczyk, C. Parmeggiani, D. Martella, M. Burrelli, and D. S. Wiersma, "Light-Fueled Microscopic Walkers", *Adv. Mater.* **27**, 3883–3887 (2015) (cited on page 8).
- [28] T. Frenzel, M. Kadic, and M. Wegener, "Three-dimensional mechanical metamaterials with a twist", *Science* **358**, 1072–1074 (2017) (cited on page 8).
- [29] M. Göppert-Mayer, "Über Elementarakte mit zwei Quantensprüngen", *Ann. Phys.* **401**, 273–294 (1931) (cited on page 8).
- [30] E. Abbe, "Beiträge zur Theorie des Mikroskops und der mikroskopischen Wahrnehmung", *Archiv f. mikrosk. Anatomie* **9**, 413–468 (1873) (cited on page 13).
- [31] J. Fischer and M. Wegener, "Three-dimensional optical laser lithography beyond the diffraction limit: 3D optical lithography off limits", *Laser Photonics Rev.* **7**, 22–44 (2013) (cited on pages 13, 15, 33, 35, 79).
- [32] C. M. Sparrow, "On Spectroscopic Resolving Power", *ApJ* **44**, 76–87 (1916) (cited on page 13).
- [33] Nanoscribe GmbH, (2015) www.nanoscribe.de (cited on page 15).
- [34] S. C. Ligon, B. Husár, H. Wutzel, R. Holman, and R. Liska, "Strategies to Reduce Oxygen Inhibition in Photoinduced Polymerization", *Chem. Rev.* **114**, 557–589 (2014) (cited on page 18).
- [35] J. B. Mueller, J. Fischer, F. Mayer, M. Kadic, and M. Wegener, "Polymerization Kinetics in Three-Dimensional Direct Laser Writing", *Adv. Mater.* **26**, 6566–6571 (2014) (cited on pages 18, 90).

-
- [36] L. Yang, A. Münchinger, M. Kadic, V. Hahn, F. Mayer, E. Blasco, C. Barner-Kowollik, and M. Wegener, “On the Schwarzschild Effect in 3D Two-Photon Laser Lithography”, *Adv. Opt. Mater.* **7**, 1901040 (2019) (cited on pages 18, 90).
- [37] J. B. Müller, “Exploring the Mechanisms of Three-Dimensional Direct Laser Writing by Multi-Photon Polymerization”, PhD thesis (Karlsruhe Institute of Technology, 2015) (cited on pages 18, 90, 93).
- [38] P. Kiefer, V. Hahn, M. Nardi, L. Yang, E. Blasco, C. Barner-Kowollik, and M. Wegener, “Sensitive Photoresists for Rapid Multiphoton 3D Laser Micro- and Nanoprinting”, *Adv. Opt. Mater.*, 2000895 (2020) (cited on page 18).
- [39] E. Waller and G. von Freymann, “Spatio-Temporal Proximity Characteristics in 3D μ -Printing via Multi-Photon Absorption”, *Polymers* **8**, 297 (2016) (cited on pages 18, 90).
- [40] O. Reynolds, “XXIX. An experimental investigation of the circumstances which determine whether the motion of water shall be direct or sinuous, and of the law of resistance in parallel channels”, *Philos. Trans. Royal Soc.* **174**, 935–982 (1883) (cited on page 20).
- [41] J. Rotta, “Experimenteller Beitrag zur Entstehung turbulenter Strömung im Rohr”, *Ing. arch* **24**, 258–281 (1956) (cited on pages 21, 63).
- [42] R. W. Fox, P. J. Pritchard, and A. T. McDonald, *Introduction to fluid mechanics / Robert W. Fox ; Philip J. Pritchard ; Alan T. McDonald* (2010) (cited on page 21).
- [43] G. S. Ash, “United States Patent: 4434010 - Article and method for forming thin film flakes and coatings”, 4434010 (Feb. 1984) (cited on page 29).
- [44] J. A. Dobrowolski, F. C. Ho, and A. Waldorf, “Research on thin film anticounterfeiting coatings at the National Research Council of Canada”, *Appl. Opt.* **28**, 2702–2717 (1989) (cited on page 29).
- [45] R. W. Phillips, T. Mayer, and G. S. Ash, “United States Patent: 5171363 - Optically variable printing ink”, 5171363 (Dec. 1992) (cited on page 29).
- [46] M. T. Gale, K. Knop, and R. H. Morf, “Zero-order diffractive microstructures for security applications”, in *Proc. SPIE 1210, Optical Security and Anticounterfeiting Systems*, edited by W. F. Fagan (Apr. 1990), pp. 83–89 (cited on page 29).

- [47] N. Yoshikawa, M. Itoh, and T. Yatagai, "Binary computer-generated holograms for security applications from a synthetic double-exposure method by electron-beam lithography", *Opt. Lett.* **23**, 1483–1485 (1998) (cited on page 29).
- [48] J. M. Meruga, W. M. Cross, P. S. May, Q. Luu, G. A. Crawford, and J. J. Kellar, "Security printing of covert quick response codes using upconverting nanoparticle inks", *Nanotechnology* **23**, 395201 (2012) (cited on page 29).
- [49] J. Andres, R. D. Hersch, J.-E. Moser, and A.-S. Chauvin, "A New Anti-Counterfeiting Feature Relying on Invisible Luminescent Full Color Images Printed with Lanthanide-Based Inks", *Adv. Funct. Mater.* **24**, 5029–5036 (2014) (cited on page 29).
- [50] P. Kumar, J. Dwivedi, and B. K. Gupta, "Highly luminescent dual mode rare-earth nanorod assisted multi-stage excitable security ink for anti-counterfeiting applications", *J. Mater. Chem. C* **2**, 10468–10475 (2014) (cited on page 29).
- [51] M. You, J. Zhong, Y. Hong, Z. Duan, M. Lin, and F. Xu, "Inkjet printing of upconversion nanoparticles for anti-counterfeit applications", *Nanoscale* **7**, 4423–4431 (2015) (cited on page 29).
- [52] M. You, M. Lin, S. Wang, X. Wang, G. Zhang, Y. Hong, Y. Dong, G. Jin, and F. Xu, "Three-dimensional quick response code based on inkjet printing of upconversion fluorescent nanoparticles for drug anti-counterfeiting", *Nanoscale* **8**, 10096–10104 (2016) (cited on page 29).
- [53] C. Campos-Cuerva, M. Zieba, V. Sebastian, G. Martínez, J. Sese, S. Irusta, Vicente Contamina, M. Arruebo, and J. Santamaria, "Screen-printed nanoparticles as anti-counterfeiting tags", *Nanotechnology* **27**, 095702 (2016) (cited on page 29).
- [54] Y. Cui, R. S. Hegde, I. Y. Phang, H. K. Lee, and X. Y. Ling, "Encoding molecular information in plasmonic nanostructures for anti-counterfeiting applications", *Nanoscale* **6**, 282–288 (2013) (cited on page 29).
- [55] Y. Cui, I. Y. Phang, Y. H. Lee, M. R. Lee, Q. Zhang, and X. Y. Ling, "Multiplex plasmonic anti-counterfeiting security labels based on surface-enhanced Raman scattering", *Chem. Commun.* **51**, 5363–5366 (2015) (cited on page 29).

-
- [56] F. Chen, J. H. Yu, and N. Gupta, "Obfuscation of Embedded Codes in Additive Manufactured Components for Product Authentication", *Adv. Eng. Mater.* **21**, 1900146 (2019) (cited on page 29).
- [57] E. N. Glezer, M. Milosavljevic, L. Huang, R. J. Finlay, T.-H. Her, J. P. Callan, and E. Mazur, "Three-dimensional optical storage inside transparent materials", *Opt. Lett.* **21**, 2023–2025 (1996) (cited on pages 29, 31).
- [58] F.-K. Bruder, R. Hagen, T. Rölle, M.-S. Weiser, and T. Fäcke, "From the Surface to Volume: Concepts for the Next Generation of Optical–Holographic Data-Storage Materials", *Angew. Chem. Int. Ed.* **50**, 4552–4573 (2011) (cited on pages 29, 31).
- [59] C. Ryan, C. W. Christenson, B. Valle, A. Saini, J. Lott, J. Johnson, D. Schiraldi, C. Weder, E. Baer, K. D. Singer, and J. Shan, "Roll-to-Roll Fabrication of Multilayer Films for High Capacity Optical Data Storage", *Adv. Mater.* **24**, 5222–5226 (2012) (cited on pages 29, 31).
- [60] D. L. N. Kallepalli, A. M. Alshehri, D. T. Marquez, L. Andrzejewski, J. C. Scaiano, and R. Bhardwaj, "Ultra-high density optical data storage in common transparent plastics", *Sci. Rep.* **6**, 26163 (2016) (cited on pages 29, 31, 32).
- [61] R. Pappu, B. Recht, J. Taylor, and N. Gershenfeld, "Physical One-Way Functions", *Science* **297**, 2026–2030 (2002) (cited on page 29).
- [62] O. Ivanova, A. Elliott, T. Campbell, and C. B. Williams, "Unclonable security features for additive manufacturing", *Addit. Manuf., Inaugural Issue 1–4*, 24–31 (2014) (cited on page 29).
- [63] R. Schittny, M. Kadic, T. Buckmann, and M. Wegener, "Invisibility cloaking in a diffusive light scattering medium", *Science* **345**, 427–429 (2014) (cited on pages 29, 115).
- [64] R. Schittny, A. Niemeyer, M. Kadic, T. Bückmann, A. Naber, and M. Wegener, "Transient behavior of invisibility cloaks for diffusive light propagation", *Optica* **2**, 84–87 (2015) (cited on page 30).
- [65] A. Niemeyer, F. Mayer, A. Naber, M. Koirala, A. Yamilov, and M. Wegener, "Uncloaking diffusive-light invisibility cloaks by speckle analysis", *Opt. Lett.* **42**, 1998–2001 (2017) (cited on page 30).
- [66] F. Mayer, S. Richter, P. Hübner, T. Jabbour, and M. Wegener, "3D Fluorescence-Based Security Features by 3D Laser Lithography", *Adv. Mater. Technol.* **2**, 1700212 (2017) (cited on pages 31, 36, 40, 42, 44).

- [67] D. Gräfe, A. Wickberg, M. M. Zieger, M. Wegener, E. Blasco, and C. Barner-Kowollik, “Adding chemically selective subtraction to multi-material 3D additive manufacturing”, *Nat. Commun.* **9**, 2788 (2018) (cited on pages 32, 50).
- [68] M. Soreni-Harari, R. St. Pierre, C. McCue, K. Moreno, and S. Bergbreiter, “Multimaterial 3D Printing for Microrobotic Mechanisms”, *Soft Robot.* **7**, 59–67 (2020) (cited on pages 32, 51).
- [69] J. Fischer, G. von Freymann, and M. Wegener, “The Materials Challenge in Diffraction-Unlimited Direct-Laser-Writing Optical Lithography”, *Adv. Mater.* **22**, 3578–3582 (2010) (cited on page 33).
- [70] U. Resch-Genger, M. Grabolle, S. Cavaliere-Jaricot, R. Nitschke, and T. Nann, “Quantum dots versus organic dyes as fluorescent labels”, *Nat. Methods* **5**, 763–775 (2008) (cited on pages 34, 43).
- [71] T. Gissibl, S. Wagner, J. Sykora, M. Schmid, and H. Giessen, “Refractive index measurements of photo-resists for three-dimensional direct laser writing”, *Opt. Mater. Express* **7**, 2293–2298 (2017) (cited on page 37).
- [72] Y. Liu, P. Chen, Z.-H. Wang, F. Bian, L. Lin, S.-J. Chang, and G.-G. Mu, “Efficient two-photon absorption of CdSe-CdS/ZnS core-multi-shell quantum dots under the excitation of near-infrared femtosecond pulsed laser”, *Laser Phys.* **19**, 1886–1890 (2009) (cited on page 45).
- [73] F. Mayer, S. Richter, J. Westhauser, E. Blasco, C. Barner-Kowollik, and M. Wegener, “Multimaterial 3D laser microprinting using an integrated microfluidic system”, *Sci. Adv.* **5**, eaau9160 (2019) (cited on pages 50, 51, 53, 57–61, 67, 69, 73).
- [74] R. Wicker, F. Medina, and C. Elkins, “Multiple Material Micro-Fabrication: Extending Stereolithography to Tissue Engineering and Other Novel Applications”, in *2004 International Solid Freeform Fabrication Symposium* (2004) (cited on page 50).
- [75] R. Wicker, F. Medina, and C. Elkins, “Multi-material stereolithography”, US7556490B2 (July 2009) (cited on page 50).
- [76] C. Zhou, Y. Chen, Z. Yang, and B. Khoshnevis, “Development of multi-material mask-image-projection-based stereolithography for the fabrication of digital materials”, in *Annual solid freeform fabrication symposium*, Austin, TX (2011), pp. 65–80 (cited on page 50).
- [77] J.-W. Choi, H.-C. Kim, and R. Wicker, “Multi-material stereolithography”, *J. Mater. Process. Technol.* **211**, 318–328 (2011) (cited on page 50).

-
- [78] S. Maruo, K. Ikuta, and T. Ninagawa, "Multi-polymer microstereolithography for hybrid opto-MEMS", in *Technical Digest. MEMS 2001. 14th IEEE International Conference on Micro Electro Mechanical Systems* (Jan. 2001), pp. 151–154 (cited on page 50).
- [79] D. Chen and X. Zheng, "Multi-material Additive Manufacturing of Metamaterials with Giant, Tailorable Negative Poisson's Ratios", *Sci. Rep.* **8**, 9139 (2018) (cited on page 50).
- [80] K. Kowsari, S. Akbari, D. Wang, N. X. Fang, and Q. Ge, "High-Efficiency High-Resolution Multimaterial Fabrication for Digital Light Processing-Based Three-Dimensional Printing", *3D Print. Addit. Manuf.* **5**, 185–193 (2018) (cited on page 50).
- [81] A. K. Miri, D. Nieto, L. Iglesias, H. Goodarzi Hosseinabadi, S. Maharjan, G. U. Ruiz-Esparza, P. Khoshakhlagh, A. Manbachi, M. R. Dokmeci, S. Chen, S. R. Shin, Y. S. Zhang, and A. Khademhosseini, "Microfluidics-Enabled Multimaterial Maskless Stereolithographic Bioprinting", *Adv. Mater.* **30**, 1800242 (2018) (cited on page 50).
- [82] D. Dendukuri, D. C. Pregibon, J. Collins, T. A. Hatton, and P. S. Doyle, "Continuous-flow lithography for high-throughput microparticle synthesis", *Nat. Mater.* **5**, 365–369 (2006) (cited on page 51).
- [83] D. C. Pregibon, M. Toner, and P. S. Doyle, "Multifunctional Encoded Particles for High-Throughput Biomolecule Analysis", *Science* **315**, 1393–1396 (2007) (cited on page 51).
- [84] D. Dendukuri, S. S. Gu, D. C. Pregibon, T. A. Hatton, and P. S. Doyle, "Stop-flow lithography in a microfluidic device", *Lab Chip* **7**, 818 (2007) (cited on page 51).
- [85] J.-H. Jang, D. Dendukuri, T. A. Hatton, E. L. Thomas, and P. S. Doyle, "A Route to Three-Dimensional Structures in a Microfluidic Device: Stop-Flow Interference Lithography", *Angew. Chem. Int. Ed.* **46**, 9027–9031 (2007) (cited on page 51).
- [86] S. C. Laza, M. Polo, A. A. R. Neves, R. Cingolani, A. Camposeo, and D. Pisignano, "Two-Photon Continuous Flow Lithography", *Adv. Mater.* **24**, 1304–1308 (2012) (cited on page 51).
- [87] D. Han, C. Yang, N. X. Fang, and H. Lee, "Rapid Multi-Material 3D Printing with Projection Micro-Stereolithography Using Dynamic Fluidic Control", *Addit. Manuf.* **27**, 606–615 (2019) (cited on page 51).

- [88] A. C. Lamont, M. A. Restaino, M. J. Kim, and R. D. Sochol, "A facile multi-material direct laser writing strategy", *Lab Chip* **19**, 2340–2345 (2019) (cited on page 51).
- [89] Z.-C. Ma, Y.-L. Zhang, B. Han, X.-Y. Hu, C.-H. Li, Q.-D. Chen, and H.-B. Sun, "Femtosecond laser programmed artificial musculoskeletal systems", *Nat. Commun.* **11**, 4536 (2020) (cited on page 51).
- [90] D. Han and H. Lee, "Recent advances in multi-material additive manufacturing: methods and applications", *Curr. Opin. Chem. Eng.* **28**, 158–166 (2020) (cited on page 51).
- [91] R. L. Truby and J. A. Lewis, "Printing soft matter in three dimensions", *Nature* **540**, 371–378 (2016) (cited on page 51).
- [92] L. J. Jiang, Y. S. Zhou, W. Xiong, Y. Gao, X. Huang, L. Jiang, T. Baldacchini, J.-F. Silvain, and Y. F. Lu, "Two-photon polymerization: investigation of chemical and mechanical properties of resins using Raman microspectroscopy", *Opt. Lett.* **39**, 3034–3037 (2014) (cited on page 51).
- [93] J. Qu, M. Kadic, A. Naber, and M. Wegener, "Micro-Structured Two-Component 3D Metamaterials with Negative Thermal-Expansion Coefficient from Positive Constituents", *Sci. Rep.* **7**, 40643 (2017) (cited on page 51).
- [94] J. Rys, S. Steenhusen, C. Schumacher, C. Cronauer, and C. Daraio, "Locally addressable material properties in 3D micro-architectures", *Extreme Mech. Lett.* **28**, 31–36 (2019) (cited on page 51).
- [95] I. Gibson, D. Rosen, and B. Stucker, *Additive manufacturing technologies: 3D printing, rapid prototyping and direct digital manufacturing*, Second Edition (Springer, New York Heidelberg Dodrecht London, 2015) (cited on page 79).
- [96] T. Baldacchini, ed., *Three-dimensional microfabrication using two-photon polymerization: fundamentals, technology, and applications*, Micro & nano technologies series (Elsevier/William Andrew, Amsterdam Boston Heidelberg, 2016) (cited on page 79).
- [97] G. M. Whitesides, "Self-Assembly at All Scales", *Science* **295**, 2418–2421 (2002) (cited on page 79).
- [98] A. Ulman, "Formation and Structure of Self-Assembled Monolayers", *Chem. Rev.* **96**, 1533–1554 (1996) (cited on page 79).

-
- [99] C. J. Brinker, Y. Lu, A. Sellinger, and H. Fan, "Evaporation-Induced Self-Assembly: Nanostructures Made Easy", *Adv. Mater.* **11**, 579–585 (1999) (cited on page 79).
- [100] J. D. Hartgerink, E. Beniash, and S. I. Stupp, "Self-Assembly and Mineralization of Peptide-Amphiphile Nanofibers", *Science* **294**, 1684–1688 (2001) (cited on page 79).
- [101] H. Yan, "DNA-Templated Self-Assembly of Protein Arrays and Highly Conductive Nanowires", *Science* **301**, 1882–1884 (2003) (cited on page 79).
- [102] R. C. Bansal and M. Goyal, *Activated Carbon Adsorption* (CRC Press, May 2005) (cited on page 81).
- [103] J. Syurik, R. H. Siddique, A. Dollmann, G. Gomard, M. Schneider, M. Worgull, G. Wiegand, and H. Hölscher, "Bio-inspired, large scale, highly-scattering films for nanoparticle-alternative white surfaces", *Sci. Rep.* **7**, 46637 (2017) (cited on page 81).
- [104] J. Bauer, A. Schroer, R. Schwaiger, and O. Kraft, "Approaching theoretical strength in glassy carbon nanolattices", *Nat. Mater.* **15**, 438–443 (2016) (cited on page 81).
- [105] T. Tancogne-Dejean, M. Diamantopoulou, M. B. Gorji, C. Bonatti, and D. Mohr, "3D Plate-Lattices: An Emerging Class of Low-Density Metamaterial Exhibiting Optimal Isotropic Stiffness", *Adv. Mater.* **30**, 1803334 (2018) (cited on page 81).
- [106] H. P. Dang, T. Shabab, A. Shafiee, Q. C. Peiffer, K. Fox, N. Tran, T. R. Dargaville, D. W. Hutmacher, and P. A. Tran, "3D printed dual macro-, microscale porous network as a tissue engineering scaffold with drug delivering function", *Biofabrication* **11**, 035014 (2019) (cited on page 82).
- [107] X. Mu, T. Bertron, C. Dunn, H. Qiao, J. Wu, Z. Zhao, C. Saldana, and H. J. Qi, "Porous polymeric materials by 3D printing of photocurable resin", *Mater. Horiz.* **4**, 442–449 (2017) (cited on page 82).
- [108] D. W. Johnson, C. Sherborne, M. P. Didsbury, C. Pateman, N. R. Cameron, and F. Claeysens, "Macrostructuring of Emulsion-templated Porous Polymers by 3D Laser Patterning", *Adv. Mater.* **25**, 3178–3181 (2013) (cited on page 82).

- [109] C. Minas, D. Carnelli, E. Tervoort, and A. R. Studart, "3D Printing of Emulsions and Foams into Hierarchical Porous Ceramics", *Adv. Mater.* **28**, 9993–9999 (2016) (cited on page 82).
- [110] L. Alison, S. Menasce, F. Bouville, E. Tervoort, I. Mattich, A. Ofner, and A. R. Studart, "3D printing of sacrificial templates into hierarchical porous materials", *Sci. Rep.* **9**, 409 (2019) (cited on page 82).
- [111] D. M. Wirth, A. Jaquez, S. Gandarilla, J. D. Hochberg, D. C. Church, and J. K. Pokorski, "Highly Expandable Foam for Lithographic 3D Printing", *ACS Appl. Mater. Interfaces* **12**, 19033–19043 (2020) (cited on page 82).
- [112] F. Kotz, K. Arnold, W. Bauer, D. Schild, N. Keller, K. Sachsenheimer, T. M. Nargang, C. Richter, D. Helmer, and B. E. Rapp, "Three-dimensional printing of transparent fused silica glass", *Nature* **544**, 337–339 (2017) (cited on page 83).
- [113] F. Svec, "Porous polymer monoliths: Amazingly wide variety of techniques enabling their preparation", *J. Chromatogr. A* **1217**, 902–924 (2010) (cited on pages 83–85).
- [114] F. Svec and J. M. J. Frechet, "Kinetic Control of Pore Formation in Macroporous Polymers. Formation of "Molded" Porous Materials with High Flow Characteristics for Separations or Catalysis", *Chem. Mater.* **7**, 707–715 (1995) (cited on page 83).
- [115] M. Ulbricht, "Advanced functional polymer membranes", *Polymer* **47**, 2217–2262 (2006) (cited on page 83).
- [116] M. W. Schulze, L. D. McIntosh, M. A. Hillmyer, and T. P. Lodge, "High-Modulus, High-Conductivity Nanostructured Polymer Electrolyte Membranes via Polymerization-Induced Phase Separation", *Nano Lett.* **14**, 122–126 (2014) (cited on page 83).
- [117] P. A. Levkin, F. Svec, and J. M. J. Fréchet, "Porous Polymer Coatings: a Versatile Approach to Superhydrophobic Surfaces", *Adv. Funct. Mater.* **19**, 1993–1998 (2009) (cited on page 83).
- [118] F. Mayer, D. Ryklin, I. Wacker, R. Curticean, M. Čalkovský, A. Niemeyer, Z. Dong, P. A. Levkin, D. Gerthsen, R. R. Schröder, and M. Wegener, "3D Two-Photon Microprinting of Nanoporous Architectures", *Adv. Mater.* **32**, 2002044 (2020) (cited on pages 84, 86, 87, 98, 101, 105, 107, 110, 112, 128).

-
- [119] C. Viklund, F. Svec, J. M. J. Fréchet, and K. Irgum, "Monolithic, "Molded", Porous Materials with High Flow Characteristics for Separations, Catalysis, or Solid-Phase Chemistry: Control of Porous Properties during Polymerization", *Chem. Mater.* **8**, 744–750 (1996) (cited on page 85).
- [120] S. Yu, F. L. Ng, K. C. C. Ma, A. A. Mon, F. L. Ng, and Y. Y. Ng, "Effect of porogenic solvent on the porous properties of polymer monoliths", *J. Appl. Polym. Sci.* **127**, 2641–2647 (2013) (cited on page 85).
- [121] D. G. Moore, L. Barbera, K. Masania, and A. R. Studart, "Three-dimensional printing of multicomponent glasses using phase-separating resins", *Nat. Mater.* **19**, 212–217 (2020) (cited on pages 85, 104).
- [122] J. Fouassier, D. Ruhlmann, B. Graff, F. Morlet-Savary, and F. Wieder, "Excited state processes in polymerization photoinitiators", *Prog. Org. Coat.* **25**, 235–271 (1995) (cited on page 90).
- [123] G. Michler, *Electron Microscopy of Polymers* (Springer Berlin Heidelberg, Berlin, Heidelberg, 2008) (cited on pages 95, 96).
- [124] I. U. Wacker, L. Veith, W. Spomer, A. Hofmann, M. Thaler, S. Hillmer, U. Gengenbach, and R. R. Schröder, "Multimodal Hierarchical Imaging of Serial Sections for Finding Specific Cellular Targets within Large Volumes", *JoVE*, 57059 (2018) (cited on page 95).
- [125] F. She, K. Tung, and L. Kong, "Calculation of effective pore diameters in porous filtration membranes with image analysis", *Robot Comput. Integr. Manuf.* **24**, 427–434 (2008) (cited on page 97).
- [126] M. Ender, J. Joos, T. Carraro, and E. Ivers-Tiffée, "Quantitative Characterization of LiFePO₄ Cathodes Reconstructed by FIB/SEM Tomography", *J. Electrochem. Soc.* **159**, A972–A980 (2012) (cited on page 97).
- [127] M. Ender, "Mikrostrukturelle Charakterisierung, Modellentwicklung und Simulation poröser Elektroden für Lithiumionenzellen", *KIT Scientific Publishing*, 10.5445/ksp/1000040284 (2014) (cited on pages 97, 100).
- [128] N. Otsu, "A Threshold Selection Method from Gray-Level Histograms", *IEEE T. Syst. Man Cy. B* **9**, 62–66 (1979) (cited on page 98).

- [129] M. Čalkovský, E. Müller, M. Meffert, N. Firman, F. Mayer, M. Wegener, and D. Gerthsen, “Comparison of segmentation algorithms for FIB-SEM tomography of porous polymers: Importance of image contrast for machine learning segmentation”, submitted (cited on page 99).
- [130] J. J. Tomes and C. E. Finlayson, “Low cost 3D-printing used in an undergraduate project: an integrating sphere for measurement of photoluminescence quantum yield”, *Eur. J. Phys.* **37**, 055501 (2016) (cited on page 111).

ACKNOWLEDGMENTS

The realization of this thesis would not have been possible in this way without the support of many different people. Hence, it is my pleasure to sincerely thank them at this point.

Foremost, I would like to thank Prof. Dr. Martin Wegener for giving me the possibility to carry out my Ph.D. thesis in his research group at KIT, and for his outstanding support while doing so. He was always up for supportive discussions on problems, and supported my work wherever he could with his great expertise. Likewise, I would also like to express my gratitude to Prof. Dr. Rasmus R. Schröder, who was not only a great collaboration partner, but who also kindly agreed to co-referee this Ph.D. thesis.

All projects in this thesis were carried out as collaborations—and within these collaborations, various people have supported me in different ways. Specifically, I would like to thank Stefan Richter from ZEISS for the fruitful discussions and the successful collaboration on the three-dimensional fluorescent security features. I have always enjoyed the positive and supportive atmosphere within this joint work. Moreover, I want to thank Jun.-Prof. Dr. Eva Blasco for the support in countless chemistry-related questions. The work on the 3D fluorescent security features would furthermore not have been possible without access to a confocal laser scanning microscope. I hence want to sincerely thank Prof. Dr. Martin Bastmeyer for the unrestricted access to the devices in his group.

The in-depth characterization of the 3D nanoporous polymers was enabled by a number of people who are experts in the field of electron microscopy. In this regard, I have collaborated with Prof. Dr. Rasmus R. Schröder (Heidelberg University) and Prof. Dr. Dagmar Gerthsen (KIT) and their respective research groups. In the group of Prof. Dr. Rasmus R. Schröder, Dr. Irene Wacker, Daniel Ryklin, and Ronald Curticean have worked on my samples. Likewise, Prof. Dr. Dagmar Gerthsen and her group, in particular Martin Čalkovský, have characterized my samples by FIB-SEM tomography. Within this collaboration, I also want to thank Prof. Dr. Pavel Levkin and Dr. Zheqin Dong for their valuable input. I felt that the working atmosphere in this collaboration was always very supportive, for which I am very grateful.

During my time as a Ph.D. student, I have been part of two graduate schools: the Karlsruhe School of Optics and Photonics and the cluster of excellence 3D Matter Made to Order. The various events I have attended—be it the summer schools, the Ph.D. seminars or the Ph.D. retreats—have promoted exchange with other students, and have regularly broadened my view on other subjects, for which I am very thankful.

I would also like to sincerely thank the people who have proofread this thesis, and have thereby helped in hunting down many mistakes: Marc Hippler, Vincent Hahn, Julian Köpfler, Andreas Niemeyer, Tobias Messer, and Hans-Peter Mayer.

The Institute of Applied Physics at KIT has a great backbone of people working in the different workshops and in the secretary's office. By keeping track of many everyday and extraordinary tasks, by supporting the students in the manufacturing of required parts, and by helping in building up experimental setups, they often enable research work to be carried out. In particular, I want to sincerely thank our technician Johann Westhauser, who not only supports the group in many everyday problems, but who also helped me in the design of the microfluidic sampleholder. Likewise, I would like to express my gratitude to the mechanics workshop, in particular to Frank Landhäußer, for the manufacturing of many different parts I have used in my experiments. Special thanks also go to Werner Gilde, Michael Hippe, and Helmuth Lay from the electronics workshop. They not only keep our IT systems running, but they also built electronic components for my experiments. My thanks also go to Ursula Möhle, Claudia Alaya and Monika Brenkmann from the secretary's office, who handle so many administrative matters for us.

I would also like to thank my great colleagues at the Institute of Applied Physics, who accompanied me during my time as a PhD student, and many of whom have become close friends. The atmosphere in the research group during or after work was always exceptionally pleasant, and when problems arose, there was always somebody to talk to.

Finally, I would like to thank my family and my partner for their continuous support, and for always helping and motivating me in going my way.

